NUMERICAL SIMULATION OF NON-ENERGETIC REACTIVE ARMORS

A THESIS SUBMITTED TO
THE GRADUATE SCHOOL OF NATURAL AND APPLIED SCIENCES
OF
MIDDLE EAST TECHNICAL UNIVERSITY

BY

MERT CAN KURT

IN PARTIAL FULFILLMENT OF THE REQUIREMENTS
FOR
THE DEGREE OF MASTER OF SCIENCE
IN
AEROSPACE ENGINEERING

JANUARY 2017

Approval of the thesis:

NUMERICAL SIMULATION OF NON-ENERGETIC REACTIVE ARMORS

submitted by **MERT CAN KURT** in partial fulfillment of the requirements for the degree of **Master of Science in Aerospace Engineering Department, Middle East Technical University** by,

Prof. Dr. Gülbin Dural Ünver
Dean, Graduate School of **Natural and Applied Sciences**

Prof. Dr. Ozan Tekinalp
Head of Department, **Aerospace Engineering**

Assist. Prof. Dr. Ercan Gürses
Supervisor, **Aerospace Engineering Department, METU**

Examining Committee Members:

Prof. Dr. Altan Kayran
Aerospace Engineering Department, METU

Assist. Prof. Dr. Ercan Gürses
Aerospace Engineering Department, METU

Prof. Dr. Mehmet Ali Güler
Mechanical Engineering Department, TOBB ETU

Prof. Dr. Bora Yıldırım
Mechanical Engineering Department, Hacettepe University

Assoc. Prof. Dr. Demirkan Çöker
Aerospace Engineering Department, METU

Date:

I hereby declare that all information in this document has been obtained and presented in accordance with academic rules and ethical conduct. I also declare that, as required by these rules and conduct, I have fully cited and referenced all material and results that are not original to this work.

Name, Last Name: MERT CAN KURT

Signature :

ABSTRACT

NUMERICAL SIMULATION OF NON-ENERGETIC REACTIVE ARMORS

Kurt, Mert Can
M.S., Department of Aerospace Engineering
Supervisor : Assist. Prof. Dr. Ercan Gürses

January 2017, 109 pages

Non-energetic reactive armors (NERAs) are one type of reactive armors which are developed to reinforce main armors of heavily armoured vehicles. Non-energetic reactive armors also called as bulging armors are known to be effective against lethal effects of shaped charges. Their structures are like sandwich structures and consist of one intermediate layer between two outer metal plates. The intermediate layer is made of inert materials such as rubber or polymers. The intermediate layer and the outer metal plates are fundemental components of defensive mechanism of these armors. The principle of the mechanism depends on shock waves which are generated by the interaction of a shaped charge jet and the intermediate layer. When the shaped charge jet hits the intermediate layer, high pressure waves are generated which cause a localized bulging of the metallic layers. These metallic layers are accelerated by the shock waves and they distort the movement of the shaped charge jet.

This thesis involves numerical simulations of the bulging armors and focuses on the investigation of high performance bulging armors (NERA-Non-energetic reactive armor). In this study, penetration of shaped charges into NERAs is simulated by using AUTODYN software. The simulations are performed in two consecutive steps which are respectively the formation of the jet and the penetration of the jet into the bulging armor. Two-dimensional multi material Euler solver of AUTODYN is chosen for the jet formation analysis. Then this jet is remapped to two and three-dimensional Lagrange solver for the jet penetration analysis. Critical material parameters of the intermediate layer that influence the performance of the armor are studied.

Keywords: Shaped Charge, Bulging Armor, Penetration, Numerical Simulation.

ÖZ

ENERJİYE SAHİP OLMAYAN REAKTİF ZIRHLARIN SAYISAL BENZETİMİ

Kurt, Mert Can
Yüksek Lisans, Havacılık ve Uzay Mühendisliği Bölümü
Tez Yöneticisi : Yrd. Doç. Dr. Ercan Gürses

Ocak 2017 , 109 sayfa

Enerjiye sahip olmayan reaktif zırhlar, ağır zırhlı araçlarda ana zırh güçlendirici olarak geliştirilen reaktif zırhların bir tipidir. Şişen zırh olarak da adlandırılan enerjiye sahip olmayan reaktif zırhların çukur imlaların öldürücü etkilerine karşı etkili olduğu bilinmektedir. Yapıları sandviç yapılar gibidir ve iki dış metal plaka arasında bulunan ara katmandan oluşmaktadır. Ara katman kauçuk veya polimerler gibi inert malzemelerden oluşmaktadır. Ara katman ve dış metal plakalar, bu zırhların savunma mekanizmasının ana bileşenlerini oluşturmaktadır. Mekanizmanın prensibi, çukur imla jeti ile ara katmanın etkileşimiyle oluşan şok dalgalarına bağlıdır. Çukur imla jeti ara katmana çarptığı zaman yüksek basınç oluşmakta ve metalik katmanların bölgesel şişmesine neden olmaktadır. Bu metalik katmanlar, şok dalgalarıyla hızlandırılmakta ve çukur imla jetininin hareketini bozmaktadır.

Bu tez, şişen zırhların sayısal benzetimlerini içermektedir ve yüksek performanslı şişen zırhların (NERA-Non-energetic reactive armor) araştırılmasına odaklanmaktadır. Bu çalışmada, çukur imlaların şişen zırhlara penetrasyonunun AUTODYN yazılımı ile sayısal benzetimi yapılmıştır. Bu benzetimler sırasıyla jet oluşum ve jetin şişen zırha penetrasyon analizleri olmak üzere iki sıralı adımda gerçekleştirilmiştir. Jet oluşum analizi için iki boyutlu çok malzemeli Euler çözücüsü seçilmiştir. Daha sonra jet, jet penetrasyon analizi için iki boyutlu ve üç boyutlu Lagrange çözücüsüne aktarılmıştır. Zırh performansını etkileyen ara katmanın kritik malzeme parametreleri üzerinde çalışılmıştır.

Anahtar Kelimeler: Çukur İmla, Şişen Zırh, Penetrasyon, Sayısal Benzetimi

To my family

ACKNOWLEDGMENTS

I would like to thank to my supervisor Assistant Professor Ercan Gürses for his ceaseless support, motivation and guidance to complete this work successfully. It was also a great honor for me to be a project assistant and work with him in METU Aerospace Engineering Department.

I would also like to state thankfulness to ROKETSAN A.Ş. for helping and giving me opportunity to take theoretical education and supports.

In addition, I want to thank my colleague, Farid Saeidi, for friendship and teamwork. We were project assistants and worked together determinedly in METU Aerospace Engineering Department.

I am very lucky to have a family, İsmet Kurt, Filiz Kurt and Onur Emre Kurt, for supporting me throughout my all educations and showing me their trusts.

This work is supported by TÜBİTAK-BİDEB National Graduate Scholarship Programme for MSc students (2210-C).

TABLE OF CONTENTS

CHAPTERS

LIST OF TABLES

TABLES

LIST OF FIGURES

FIGURES

LIST OF ABBREVIATIONS

NERA	Non-energetic reactive armor
NxRA	Non-explosive reactive armor
ERA	Explosive reactive armor
SLERA	Self-limiting explosive reactive armor
F-plate (FMP)	Forward moving plate
B-plate (BMP)	Backward moving plate
RHA	Rolled homogeneous armor
UHMWPE	Ultra high molecular weight polyethylene
WFRCA	Woven fabric rubber composite armors
EOS	Equation of state
LD	Liner diameter
CD	Charge diameter
WD	Warhead diameter
FRP	Fiber reinforced plastics
JWL EOS	Jones-Wilkins-Lee equation of state
CFL	Courant-Friedrichs-Levy

LIST OF SYMBOLS

t	Time
U_s	Shock velocity
C_1	Bulk sound speed
S_1	Slope of the Hugoniot curve
U_p	Particle velocity
Γ	Gruneisen coefficient
K	Bulk modulus
V	Specific volume
C_v	Specific heat
I	Internal energy
σ	Yield strength of a material
ϵ	Equivalent plastic strain
T_H	Homologous temperature
T_{Melt}	Melting temperature
T_{Room}	Room temperature
A	Yield stress
B	Hardening constant
n	Hardening exponent
C	Strain rate constant
m	Thermal softening exponent
G	Shear modulus
Y	Yield stress
Y_0	Yield stress value at the reference state
G_0	Shear modulus value at the reference state
ρ	Density
Z	Impedance
V_j	Jet velocity
V_{tip}	Jet tip velocity

CHAPTER 1

INTRODUCTION

Heavily armoured vehicles (tanks etc.) contain a thick armor, yet it is insufficient for protection against shaped charges which are high-explosive anti-tank warheads. For this reason, reactive armors also called add-on armors have been developed to increase the protection level of armored vehicles. The add-on armors are used in front of the main armor and they can prevent lethal effects of shaped charge jets. A reactive armor is a sandwich structure and generally consists of three plates. The outer layers are typically made of steel plates and the mid layer could be explosive, energetic, rubbery or polymeric materials depending on the particular type of the reactive armor.

1.1 Shaped charges

Shaped charges encapsulate explosive materials that provide high penetration capabilities. There are many distinctive utilizations of shaped charges in both non-military and military applications. Non-military applications involve construction works, petroleum exploration works and mining jobs. In military applications, shaped charges are used as deadly threats against heavily armored vehicles. Shaped charges are located in the warhead of anti-tank weapons. The purpose of shaped charges is to puncture through the main armors of heavily armoured vehicles.

According to [29], a shaped charge consists of a hollow cavity which is filled with explosive and an initiation part. If this cavity does not compose of a liner, this model is called as an unlined-cavity charge or hollow charge. Moreover, if the cavity composes of a liner, the model is called cumulative or shaped charge. The shape of the liner can be parabolic, conic or hemispheric. If the liner's geometry is like bowl shaped, the device is called explosively formed penetrator (EFP) [29].

Shaped charge jet formation is shown in Figure 1.1. Firstly, when a missile hits a target, a piezo-electric trigger activates a detonator and explosive is detonated. After explosion, high pressure developes and a conical liner is compressed and pushed forward with very high velocity. This conical liner forms a longitudinal jet.

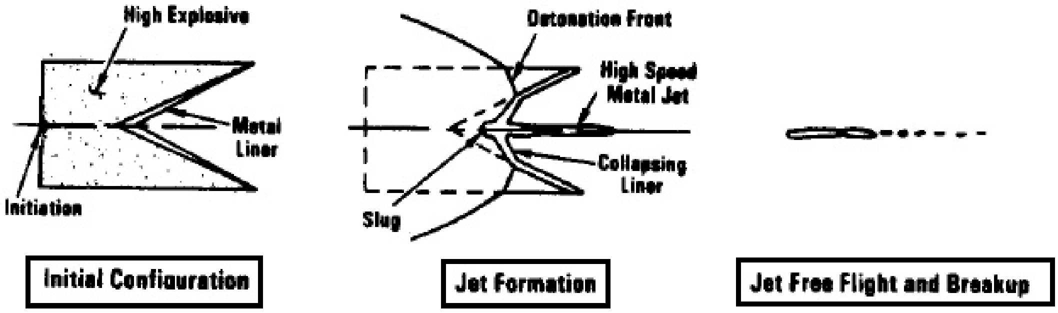

Figure 1.1: Stages of shaped charge jet formation [4]

A schematic view of a shaped charge is shown in Figure 1.2. In this figure, LD implies the liner diameter; CD is the charge diameter and WD is the warhead diameter. The stand-off is the distance between the front of the shaped charge and the target.

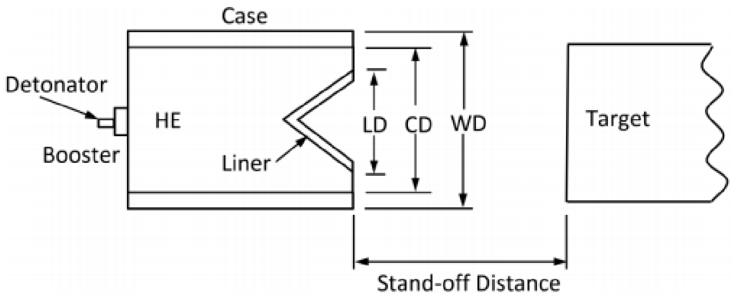

Figure 1.2: A schematic view of a shaped charge [30]

While a shaped charge jet is penetrating through a target, high stresses arise in the target. These stresses are much higher than yield strengths of materials so this interaction is called as hydrodynamic penetration. In the hydrodynamic state of a material, the material loses its strength due to higher strain rate affected by pressure and behaves like a fluid. In this case, material strength does not have to be taken into account for the penetration. On the other hand, pressure and volume changes in the material are considered within the interaction. The jet performance is related to depth of penetration. Jet density, jet length and the ratio of deflected material to total material of the jet are major factors effecting the penetration depth.

A generic shaped charge modelled in Ansys DesignModeler software is shown in Figure 1.3. Typical components of a shaped charge are given in this figure.

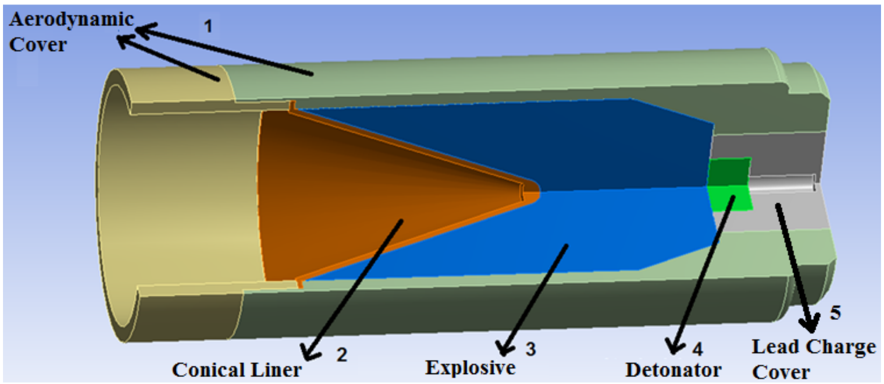

Figure 1.3: Shaped charge model [16]

1.2 Reactive armors

Reactive armors have been developed to reduce penetration capability of shaped charges. These armors are used as add-on armors in front of main armors. Reactive armors could be divided into four main subgroups based on different intermediate layer materials. These are explosive reactive armor (ERA), self-limiting explosive reactive armor (SLERA), non-explosive reactive armor (NxRA) and non-energetic reactive armor (NERA) [5]. In Figure 1.4, types of reactive armor are shown with a diagram.

In this thesis, non-energetic reactive armor (NERA) will be modelled and used for all analyses. NERA and ERA are composed of two metallic plates and an interlayer material placed between the metallic plates. Different interlayer materials are used in these armors. Details and the defeat mechanisms of ERA and NERA will be comprehensively described in Section 1.2.1 - Section 1.2.2. In literature, there is limited or no information about the mechanisms of SLERA and NxRA. Therefore, only general information including materials of these armors, advantages and disadvantages will be mentioned.

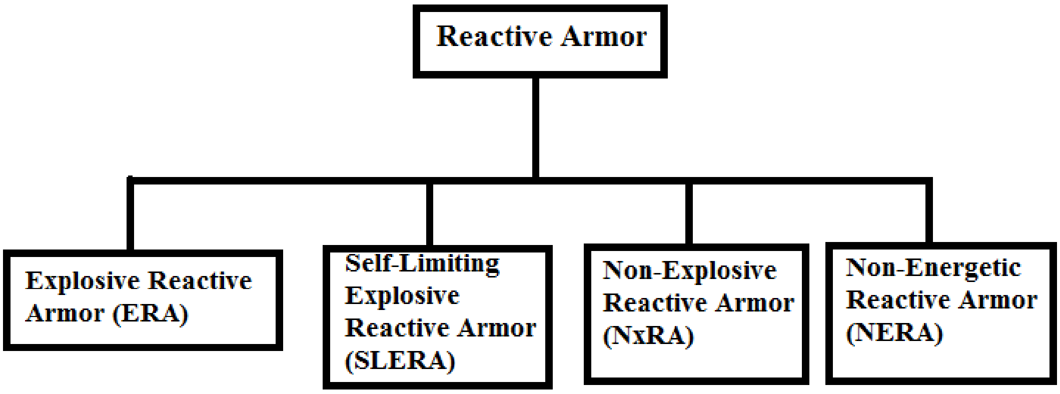

Figure 1.4: Reactive Armors [5]

The self-limiting explosive reactive armor (SLERA) is a passive form of ERA. It contains a low quantity of explosives and therefore it shows lower performance against missiles than ERA. On the other hand, this provides reduced negative effects caused by explosives on armored vehicles [15].

The non-explosive reactive armor (NxRA) does not include explosive. Instead, it contains gas generating and non-explosive materials to spread the energy due to a hit by an anti-tank missile. NxRA is a totally passive armor. It is less effective than ERA [15].

To indicate the performance of the armors, in Figure 1.5, a schematic view of efficiency versus survivability/safety of the armors is given. The survivability or safety of the armors means that the protected enclosure is not being severely affected by shaped charge jet attack or projectile threat. In other words, the armors can sustain multiple hits. This figure indicates that the efficiency or performance of ERA is the highest. However, the survivability of ERA is the lowest. NxRA and NERA have the opposite of the characteristics of ERA. Also, SLERA shows moderate characteristics.

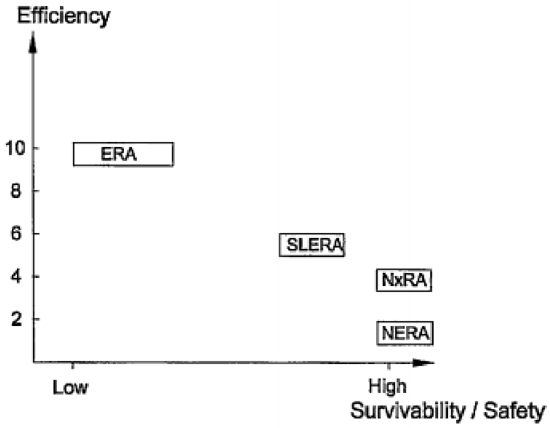

Figure 1.5: A schematic view of efficiency vs survivability/safety of reactive armors [5]

1.2.1 Explosive reactive armor (ERA)

In explosive reactive armors (ERAs), an explosive material is used as intermediate layer [9]. Efficiency of this reactive armor is known to be more effective than non-energetic reactive armors. Upon the penetration of the jet the intermediate layer explodes accelerating metal plates in opposite directions. These accelerated plates interact with the shaped charge jet and distort it. Due to the explosive involved and accelerated plates, this armor causes a threat to infantry units. The composition and mechanism of an explosive reactive armor are shown with a diagram in Figure 1.6.

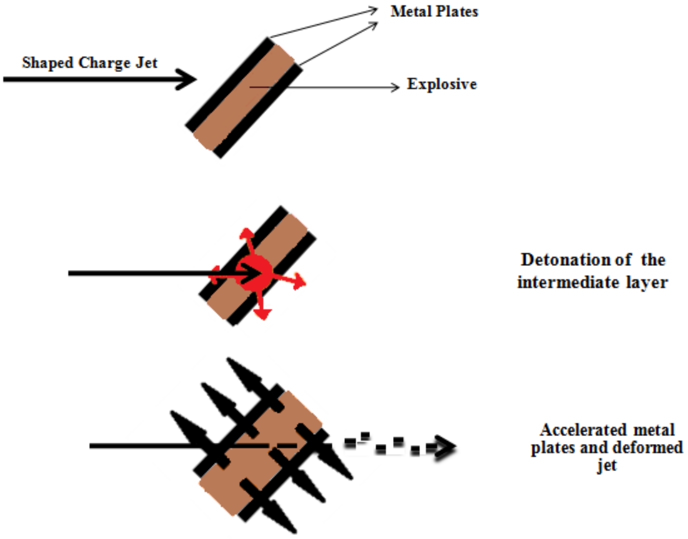

Figure 1.6: The composition and mechanism of an explosive reactive armor

1.2.2 Non-energetic reactive armor (NERA)

Non-energetic reactive armors (bulging armors) were firstly proposed by Held [10]. Their intermediate layers include inert materials like rubbery or polymeric materials rather than explosives. Bulging armors have a distinctive mechanism when they are compared with explosive reactive armors. The mechanism of NERAs is especially based on shock waves formed in the intermediate layer. While a shaped charge jet penetrates into NERA, the metallic layers start to bulge on the impact region due to high pressures in the intermediate layer. Then, the metallic layers swiftly move outwards by shock waves. The shaped charge jet is disturbed by the moving metallic layers [32, 6, 22]. Due to higher acceleration of the plates caused by explosives, ERAs are more effective against shaped charges than NERAs. The composition and mechanism of a non-energetic reactive armor are shown in Figure 1.7.

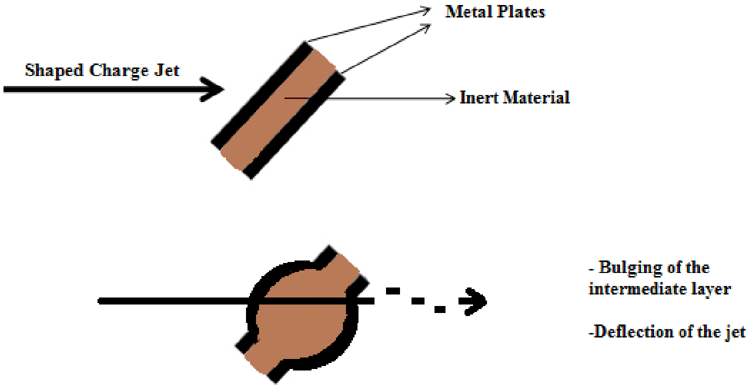

Figure 1.7: The composition and mechanism of a non-energetic reactive armor

1.3 Literature Survey

In literature, there are several studies on ERA, yet works on NERA are limited. Therefore, the main features of the defeat mechanisms of ERA are well known.

The first theoretical study concerning the interaction of ERA with a shaped charge jet was made by Mayseless et al. about three decades ago [21]. Meyseless et al. developed a mass flux model by using the conversation laws. In this model, variation of the velocity along the jet was omitted and therefore the velocity of the jet was taken uniform. According to this work, while the jet penetrates through the first metal plate, the explosive located in the intermediate layer is detonated and consequently both outer metal plates are accelerated in opposite directions. One of the accelerated metal plates, moving to the same direction of the jet, is called forward moving plate (F-Plate) and the other accelerated plate moving to the opposite direction of the jet is called backward moving plate (B-Plate). If ERA is not aligned perpendicular to the direction of the jet's motion, velocity vectors of F-Plate and B-Plate are not parallel to the velocity vector of the jet. After the interaction between plates and the jet, straight and intact structure of the jet is disturbed. This case is shown in Figure 1.8. In the study of [21], the interaction of accelerated F-Plate and B-Plate with shaped charge jets were investigated experimentally and numerically. The F-Plate which is accelerated in the same direction as the movement of the jet has more apparent effects on the jet than the B-Plate because of longer interaction time.

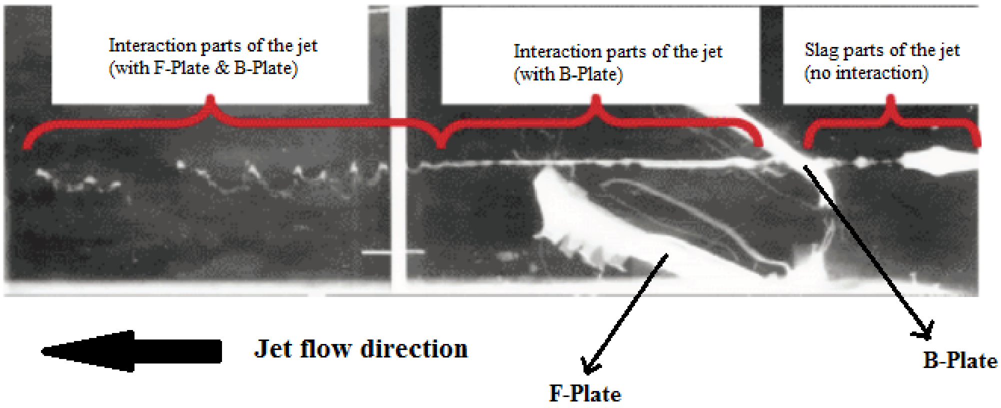

Figure 1.8: The interaction of a shaped charge jet with ERA [20].

The mass flux model was later improved and the velocity of F-Plate in ERA was investigated by Mayseless [20]. Moreover, the effects of some parameters like the angle of an incoming jet and the thickness of metal plates on the performance of ERA were studied.

One of the first studies on the interaction of bulging armors with shaped charge jets was conducted by Gov, Kivity and Yaziv [6]. This work includes not only two-dimensional numerical studies but also a limited experimental study. In both these numerical and experimental studies, a shaped charge jet hits an armor that is aligned perpendicular to the axis of the jet. The stand-off distance was taken 2.5 times the diameter of the shaped charge. The jet's tip velocity was measured 7 km/s in the experiments. The jet's yield strength was ignored and Von Mises criterion was used only for the metal plates. According to this study, the main difference between bulging armors and explosive reactive armors was stated as the energy source, causing acceleration of metal plates. Like in ERA, the accelerated plates interact with the jet in transverse direction and disturb intact and straight jet. Furthermore, the interaction mechanism of a bulging armor with a shaped charge jet was explained in this work. Firstly, the shaped charge jet penetrates through the B-Plate and reaches the intermediate layer. In this case, significant amount of pressure builds up in the intermediate layer and some of the jet's kinetic energy is transferred into the intermediate layer. Then, shock waves develop and spread from the compression point of the intermediate layer radially. Because of the shock waves, the metal plates deform, bulge and accelerate. Neoprene rubber was chosen as the intermediate layer.

Following the study above, a similar work which includes experiments and two-dimensional numerical simulations was carried out three years later by Yaziv, Frilling and Kivity [32]. In their study, the stand-off distance was taken 2.5 times the diameter of the shaped charge. As a result of the experiments, the jet's tip velocity was measured 7 km/s. One substantial difference from the study mentioned before is that the armor is placed in an inclined configuration. In the experiments performed by Yaziv, Frilling and Kivity, eight distinctive nonmetallic intermediate layers and five different metal plates were tested. The material properties of these samples are not given in their article. Moreover, in their article it is mentioned that the depth of penetration into a witness plate depends on the bulge height of an armor. When the armor bulges more, the penetration depth of the jet decreases. It is also stated that for better performance, high strength metal plates should be used and the shock impedance difference between metal plates and the intermediate layer should be high. Another important result of their study is that the performance of ERA is more sensitive to the inclination angle of the armor than bulging armors. The interactions of ERA and bulging armor with shaped charge jets are shown in Figure 1.9.

The interaction mechanisms between shaped charge jets and reactive armors have been studied by Mayseless et al. [22]. In explosive reactive armors, it is assumed that the velocity vectors of metal plates are perpendicular to the surfaces of the armor. In bulging armors, however, the velocity vectors of metal plates are not constant on the

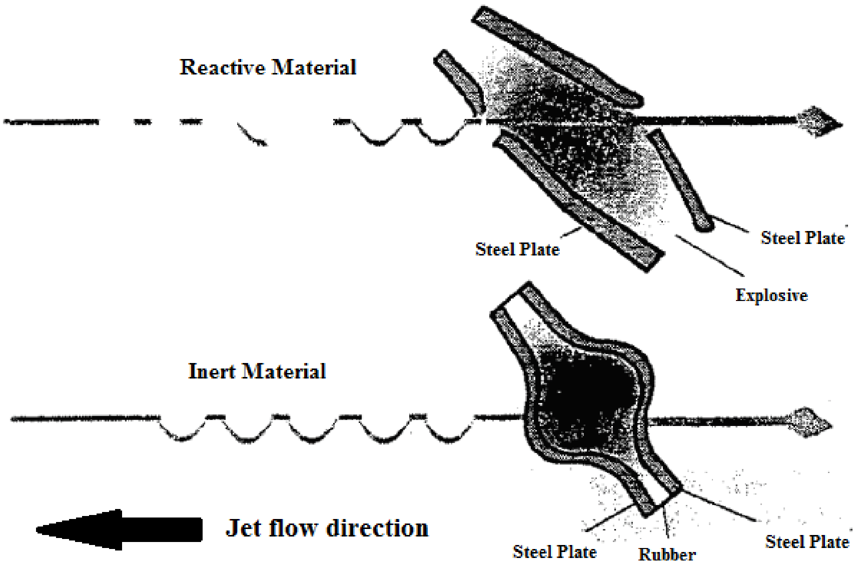

Figure 1.9: a) Interaction between ERA and a shaped charge jet, b) interaction between a bulging armor and a shaped charge jet [32].

surface of metal plates. The non-uniformity of velocity vectors results in bulging. The authors developed an analytical model that estimates the diameter reduction of a jet, grazed by the metal plates, during the penetration of the plates by the jet. They named this model *grazing model*. The jet becomes thinner while penetrating into the plates. With the use of the grazing model, it was concluded that F-Plate is more effective at reducing the penetration depth of jets than B-Plate. This model was only applied to ERAs inasmuch as it is applicable to metal plates accelerated in the perpendicular direction to the surface of the armor. Therefore, this formulation cannot be used for bulging armors. Although necessary adjustments of the model for bulging armors were indicated in their article, no concrete model was developed.

Yadav [31] studied different bulging armor systems by changing the material used in the intermediate layer. Three different materials were used as intermediate layer, namely neoprene, plexiglass and bakalite. In his work, an analytical model was developed and it was applied to these different armors. Yadav [31] tested the analytical model for a jet with a tip velocity of 9 km/s and three different thicknesses of the intermediate layer, i.e., 10 mm, 20 mm and 30 mm. The fundamental assumption of this model is that metal plates bulge because of shock wave propagation from the intermediate layer. There are also other assumptions which are: (i) the intermediate layer is taken as a fluid (strenghtless), (ii) the diameter of the hole formed in the intermediate layer is taken as same as a the diameter of the jet, (iii) it is assumed that high pressures are generated by the jet causing shock waves in the intermediate layer. It was stated that the performance of an intermediate layer is directly proportional to the shock energy in that layer. The shock energy increases with an increase in the density and a decrease in the strength of the material used in the intermediate layer. The author mentioned the derivation of an equation about the energy of the shock wave in the interlayer material. According to this equation, the interlayer materials, having high density and low strength value, show better performance against shaped charge jets due to the greater shock energy. Yadav [31] tested three materials and found that neoprene which has the highest density and the lowest strength value is the most appropriate material for the intermediate layer. Moreover, it is stated that Hugoniot parameters of an intermediate layer also affect the shock energy.

Held [11] performed several experiments with bulging armors. In the experiments, the diameter of the copper liner of a shaped charge was taken 115 mm. The standoff distance is 350 mm and the plates are made of mild steel. The thicknesses of B-Plate, F-Plate and the intermediate layer are respectively 2 mm, 4 mm and 20 mm. Held [11] conducted two tests for two different interlayer materials. In his first test, unidirectional Dyneema fibers were used. Dyneema is an ultra high molecular weight polyethylene (UHMWPE) based material. Furthermore, Dyneema panel consists of approximately 80% fiber content. In his second test, a plain woven fabric which consists of 90% fiber content was tested. In both tests, one witness plate was placed at a 1700 mm distance away from the shaped charge. Flash x-ray pictures given in Figure 1.10 were taken in the experiments. It was seen that some parts of a jet did not interact with the metal plates. Thus, these parts of the jet moves in a straight manner without any disturbance. The velocity of these parts is between 9 km/s and 6 km/s. As a result of the experiments, the tip velocity of the jet was measured 9.3 km/s. Also, it was stated that the periodic interactions of the disturbed jet with the bulging armor happens with a the frequency range between 50 kHz and 200 kHz.

Rosenberg and Dekel [25] performed two-dimensional simulations of bulging armors. In their work, the factors effecting the bulging process were investigated and some

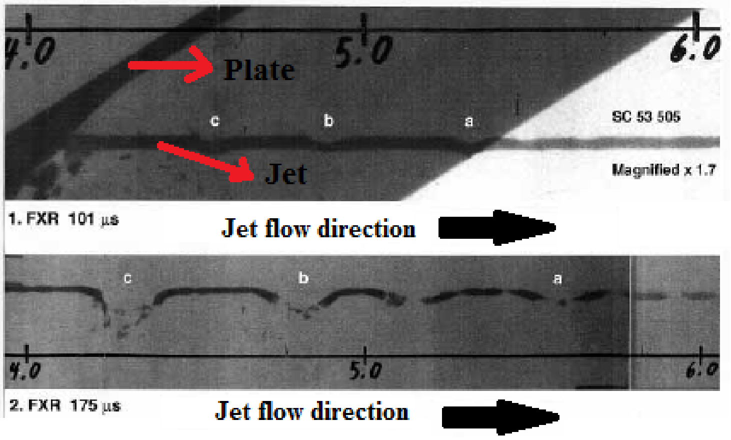

Figure 1.10: Flash x-ray pictures are taken 101 microseconds and 175 microseconds after the initiation of the shaped charge [11]. Dyneema is used as an interlayer material of the bulging armour.

suggestions for better performance were given. Plate thickness, intermediate layer thickness, yield strength and modulus of elasticity were varied to evaluate the performance of the bulging armor. The conclusions of their work are that the material of the intermediate layer should have low strength with a density in the range of $1.5 - 2.5$ g/cm^3. It was stated that the shear modulus of the intermediate layer does not affect the bulging performance. On the other hand, it was mentioned that the bulging velocity of metal plates depends on the thickness of the intermediate layer. Rosenberg and Dekel [25] suggested that the thicknesses of metal plates should be taken asymmetrically for a better performance.

Thoma et al. [28] performed experiments on bulging armors. In their experiments, two bulging armors were placed with some distance as shown in Figure 1.11. The caliber and conical angle of a shaped charge are respectively 136 mm and $60\,^\circ$. This shaped charge can penetrate a distance of 950 mm into a rolled homogeneous armor (RHA) witness plate. This penetration depth is obtained with a 6-caliber stand-off distance. Caliber means the diameter of a shaped charge. Additionally, jet‘s tip velocity can reach up to 8.25 km/s. In their experiments, the angle between the plate normal and the flow direction of a jet is $65\,^\circ$. The thickness and yield strength of metal plates are 10.5 mm and 1200 MPa. The metal plates are made of RHA. The thickness of the intermediate layer was varied between 7 mm and 8 mm. The distance between two armors is 71 mm. In the work of Thoma et al. [28], five different intermediate

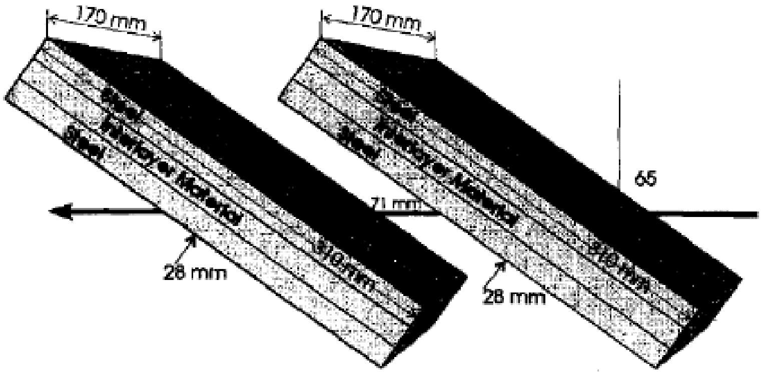

Figure 1.11: The position of two bulging armors[28].

layer materials were examined and all other parameters were taken as constant. Elastomer and fiber reinforced plastics (FRP) were selected as reference materials. It is concluded from the experiments that the reference materials exhibit 2 to 4 times better performance than other materials tested. Furthermore, in order to support the results of the experiments, three-dimensional numerical simulations were performed. In the numerical simulations, the diameter of the jet was taken variable and its velocity gradient was nonlinear. The material of the jet was elastic-plastic and the plates were elastoplastic with strain hardening effects. The results of the numerical simulations were similar to the results of the experiments.

Jia et al. [13] investigated composite bulging armors experimentally. The shaped charge jet used in the experiments has 56 mm diamater, 73 mm length, 60° conical angle and 0.8 mm copper liner thickness. The experiments were conducted with a stand-off distance of 80 mm. The tip velocity of the jet was measured approximately 6 km/s. The bulging armor was made of S235 steel plates, woven fabric layers and one rubber layer, see Figure 1.12. The thickness of the steel plates and the woven fabric layers are 3 mm and 1 mm, respectively.

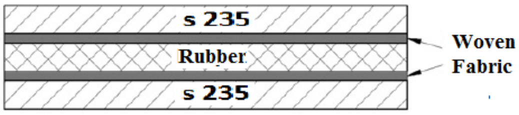

Figure 1.12: The composition of a bulging armor [13].

In the work of Jia et al. [13], only woven fabric was changed and four different materials were tested. The materials of the woven fabric are carbon fiber, glass fiber, kevlar and poly (PBO). The density of the rubbery material is 1.3 g/cm^3 and its tensile strength is 23.8 MPa. The density and the tensile strength of the steel plates are 7.84 g/cm^3 and 235 MPa, respectively. Two different armors were designed as reference armors and were used to evaluate the armor which contains woven fabric. The first reference armor consists of steel plates (3 mm thickness each) and a rubbery layer (5 mm thickness) in between. In the second reference armor, the rubbery layer is replaced with a steel plate. Hence, the second reference armor consists of three steel plates (3/5/3 mm thickness). The experimental setup is shown in Figure 1.13.

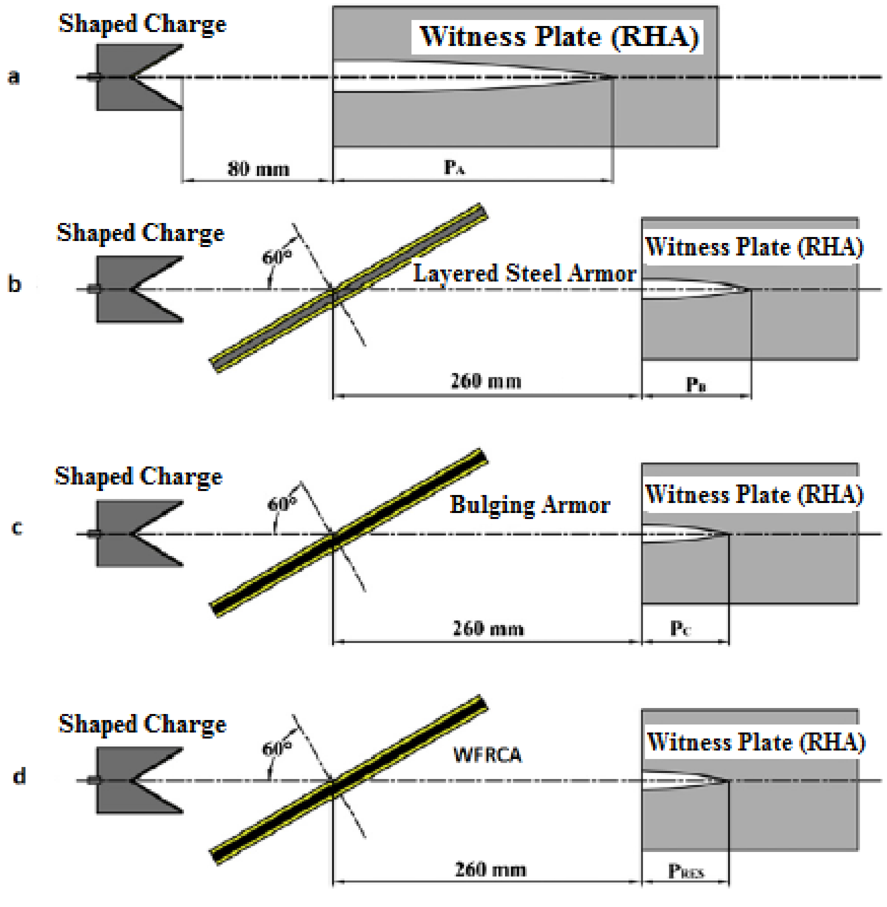

Figure 1.13: Experimental setups. a) only witness plate, b) a three-layered steel armor, c) classical bulging armor, d) woven fabric rubber composite armor (WFRCA) [13].

In the experiments, Jia et al. [13] selected four different types of woven fabrics to place between the metal plate and the rubber layer. These materials and the penetration values of shaped charges into witness plates are given in Table 1.1. At the end of the work, Jia et al. mentioned that the best two performances were obtained from Kevlar fabric and PBO fabric. Additionally, interaction frequencies between jets and armors were investigated. It is stated that the interaction frequency of Kevlar fabric is in the range of 120-160 kHz, while other fabrics are in the range of 60-100 kHz.

Table 1.1: Tip velocity of the jet and the amounts of penetration into the witness plate for different armor configurations [13].

Armor type	Interlayer	Velocity of jet tip [m/s]	Res. penetration [mm]
WFRCA	Carbon	6250	94
WFRCA	Glass	6098	87
WFRCA	Kevlar	6098	76
WFRCA	PBO	6410	83
Bulging armor	Rubber	5814	82
Layered steel armor	Steel	6098	114

Zu, Huang and Jia [33] developed an analytical model and also performed experiments to observe interactions of a shaped charge jet with a bulging armor. They discussed the importance of the thickness of the intermediate layer and the inclination of the armor on protective performance. A rubbery material used in the experiments. The density and the tensile strength are 1.3 g/cm^3 and 20 MPa, respectively. The outer diameter of the shaped charge was 56 mm and the copper liner thickness is 0.8 mm. In the experiments, penetration into a witness plate was measured approximately 180 mm for a stand off distance of 80 mm. Furthermore, jet‘s tip velocity was 6 km/s and its tail velocity was 1.9 km/s. The diameters of jet‘s tip and tail are 1.5 mm and 9 mm, respectively. As a result of this work, when the inclination of the armor is $60\,^\circ$ and the thickness of the intermediate layer is 3.0 to 3.5 mm, the bulging armor provides the best protection. The results of the analytical model are in agreement with the experimental results.

Lidén, Helte and Tjernberg [19] performed ballistic experiments with two parallel NERA-panels like the work of Thoma et al. [28]. However, in the work of Lidén et al., the effects of armor orientations on armor performance were studied. Both bulging armors consist of a rubbery intermediate layer (5 mm thickness) and two steel plates (3 mm thickness each). AUTODYN software was used for three-dimensional numerical analyses. In the analyses, Johnson Cook strength model and Mie-Gruneisen equation of state (EOS) were selected for the steel plates and the jet. For the rubbery material, strength was ignored, yet Mie-Gruneisen EOS was used. When the jet interacted with two parallel NERA armors, a penetration of 60 mm occured into the witness plate. This depth was 40 mm in the experiments for two cross-wise oriented NERA-panels. It was concluded that the use of cross-wise oriented panels increases the protection capability of bulging armors considerably.

Huang et al. [12] investigated the effects of the wave impedance of intermediate layer materials on performance of bulging armors. Their work includes experimental, theoretical and numerical studies. Four different materials were used for the intermediate layer of a bulging armor. These materials were polycarbonate, Kevlar-epoxy, fluorocarbon rubber and polyrubber. When fluoro rubber was selected for the intermediate layer, the depth of penetration into a witness plate was measured 81 mm. For the other three intermediate layers, the depth of the penetration was approximately 130 mm. Numerical analyses were conducted with AUTODYN. According to the results of the analytical model, the mass efficiency or the protection capability of the bulging armor was computed to be approximately 1.8 for fluoro rubber and 1.2 for other materials. Analytical and numerical results show that fluorocarbon is the best intermediate layer material. It was stated that use of higher density materials for the intermediate layer improves the armor performance. Moreover, it was indicated that the best armor performance was observed when the wave impedance of the intermediate layer material was in the range of 0.2-0.6 g/cm$^3\cdot$ mm/μs.

Zu, Huang and Xiao [34] performed experiments and numerical studies to investigate the effect of inclination of bulging armors on protection performance. Polybutylene was used as the intermediate layer material. Angles between the normal of a bulging armor and the direction of a jet was taken as $0\,^\circ$, $30\,^\circ$, $45\,^\circ$, $60\,^\circ$ and $68\,^\circ$. When the angle of the bulging armor is $0\,^\circ$ (parallel to the direction of a jet), the penetration into the witness plate is 83 mm. If this angle is changed to $68\,^\circ$, the penetration distance reduces to 35 mm. This penetration distance decreases with the increase of the angle. Also, the mass efficiency of the bulging armors depends on the inclination of the armor and increases with increase in angle. In this work of Zu et al., the mass efficiencies were calculated as 2.02, 2.10, 3.05, 3.29 and 3.46 for 0°, 30°, 45°, 60° and 68°, respectively. AUTODYN software was used for numerical simulations. Zu et al. stated that the results of the numerical studies were consistent with the experimental results.

Experimental studies found in the literature are summarized in Table 1.2. Additionally, analytical and numerical models in the literature are given in Table 1.3.

Table 1.2: Experimental studies on bulging armors

Reference	Intermediate Layer Material	Year
Gov, Kivity and Yaziv [6]	Neoprene	1992
Thoma et al. [28]	Optimized materials, elastomer and FRP	1993
Yaziv, Frilling and Kivity [32]	Non-metallic materials	1995
Held [11]	Dyneema fiber	2001
Lidén, Helte and Tjernberg [19]	Rubber	2007
Zu, Huang and Xiao [34]	Polybutylene Rubber	2010
Huang et al. [12]	Fluorocarbon Rubber	2011
Jia et al. [13]	Rubber+Woven fabric	2013
Zu, Huang and Jia [33]	Rubber	2013

Table 1.3: Analytical and numerical models in the literature

Reference	Analytical/Numerical	2D /3D	Year
Gov, Kivity and Yaziv [6]	Numerical	2D	1992
Mayseless et al. [22]	Analytical/Numerical	2D	1993
Thoma et al. [28]	Numerical	3D	1993
Yaziv, Frilling and Kivity [32]	Numerical	2D	1995
Rosenberg and Dekel [25]	Numerical	2D	1998
Yadav [31]	Analytical	2D-3D	2004
Lidén, Helte and Tjernberg [19]	Numerical	3D	2007
Zu, Huang and Xiao [34]	Numerical	2D-3D	2010
Huang et al. [12]	Analytical/Numerical	2D-3D	2011
Zu, Huang and Jia [33]	Analytical	2D-3D	2013

In a nutshell, it has been mentioned in many works that the performance of a bulging armor is directly proportional to the density of the intermediate layer and inversely proportional to the strength of this layer. It was stated that the shear strength of the intermediate layer does not affect the performance of the bulging armor significantly. On the other hand, the strength of the metal plates should be high for a better performance of the armor. Furthermore, the thicknesses of the intermediate layer and the metal plates and the inclination of the armor can affect the performance considerably.

CHAPTER 2

MODELING OF MATERIAL RESPONSE

In this thesis, interaction of a shaped charge jet with a non-energetic reactive armor (NERA) called bulging armor is studied. Autodyn software is used for the numerical simulations. Explicit time integration is the solution techniques for these simulations. The equations in explicit integration are decoupled, so there is no need to invert the stiffness matrix. Also, the mass matrix in the equations of motion is diagonal and mathematically trivial to solve. Velocities and displacements are calculated using central difference integration [3]. Stability of the integration is controlled by time step size (Courant-Friedrichs-Levy (CFL) condition). Element size, material sound speed (C_1) and safety factor affect the time step size during numerical simulations. Smaller element size and/or higher C_1 cause small time step. In this case, accuracy for stress wave propagation is ensured [1].

On the other hand, a shaped charge model is built using ANSYS DesignModeler. For the interaction analyses, the stand-off distance of the jet and the angle between the jet flow direction and the surface normal of the armor are taken constant. The layer thickness for the bulging armor and the mechanical properties of the metal plates are also constant. On the other hand, various polymeric materials from the AUTODYN material library are used to fill the intermediate layer. Analyses are conducted to determine the most effective interlayer in terms of the bulging performance of the NERA. Critical parameters of the intermediate layer material with regard to bulging performance are determined by the help of numerical analyses. The purpose of this study is to increase the effect of the NERA against the shaped charge jet.

This chapter discusses the models used for the description of the material response for the jet and the armor. Material properties such as the shock equation of state (EOS), the Jones-Wilkins-Lee (JWL) EOS, the strength model and the failure model are discussed. In AUTODYN, relations involving the EOS models, the strength and the failure models are used to predict dynamic behaviors of materials and enable materials to propagate shock waves. The simulation of materials exposed to shock waves needs these fundamental equations. Therefore, these models are utilized for the materials used in this thesis. The EOS defines the pressure as a function of density, temperature and energy. The strength model is employed to describe the yielding behavior of materials. In addition, the failure model takes into account the effect of many factors such as strain, strain rate, pressure and temperature on the failure criteria of materials. Detailed information on these equations are presented below.

2.1 Equation of State (EOS)

The equation of state (EOS) provides a relationship among the density of a material, the pressure and the temperature. It is associated with the state of the material which is under high-pressure compression and temperatures [26]. Stress is defined in a tensorial form and mostly separated into a volumetric tensor (hydrostatic pressure) and a deviatoric tensor (shear stress). Hydrostatic pressure plays a fundamental role in the equation of state (EOS) of a material. In addition to hydrostatic pressure, there are also two important parameters for the EOS, which are specific energy and specific volume.

In this section, the Mie-Gruneisen EOS [23, 7, 18] and the Jones-Wilkins-Lee (JWL) EOS [17, 2] are explained in detail.

2.1.1 Mie-Gruneisen Equation of State (EOS)

In 1903, Gustav Mie proposed a general equation useful for derivation of solid phase equations. Eduard Gruneisen extended Mie‘s form of the equation. This extended equation serves as a basis for derivation of the Mie-Gruneisen equation of state (EOS) [18]. The Mie-Gruneisen EOS establishes a relation between pressure and internal energy obtained from the Hugoniot curve. This EOS can be applied to materials based on the Hugoniot data. The Hugoniot curve exhibits the relations between the pressure and the particle velocity of a material. The Hugoniot is related to an empirical equation considering shock transitions instead of all the equilibrium states of a material. The Mie-Gruneisen EOS is employed to characterize shocked solids [26]. The shock state can be obtained from a plate impact experiment. During the experiment, the shock front and the particle velocity behind the shock front occur. The relation between them is specified in the linear formulation below.

$$U_s = C_0 + S \cdot U_p \tag{2.1}$$

U_s is the shock velocity, C_0 is the bulk sound speed of a material, U_p is the particle velocity of a material and S is the slope of the shock velocity-particle velocity curve. These parameters can be seen in Figure 2.1 for Aluminium 6061. This figure is obtained from experimental data. C_0 is expressed in velocity units. Moreover, the Gruneisen parameter (Γ) is also used in the theory of shocked solids. The Gruneisen parameter is considered as independent of temperature [26]. The relation between S and Γ [1] can be given in an equation shown below.

$$S = (\Gamma + 1)/2 \tag{2.2}$$

The Gruneisen parameter can be computed by using the relation [35].

$$\Gamma = \frac{3 \cdot K \cdot V \cdot \alpha}{C_v} \tag{2.3}$$

In this equation, K implies the bulk modulus; V is the specific volume, $V = 1/\rho$; α is the thermal expansion coefficient and C_V is the specific heat.

In AUTODYN theory manual, the Mie-Gruneisen EOS is appeared under the title of *The Shock EOS*. The Shock EOS is a particular equation of state commonly used for high velocity impact simulations. In this thesis, the shock EOS is used for the materials of a shaped charge and a bulging armor. The shock EOS can be expressed in linear or bilinear forms. The bilinear shock EOS is especially used in non-metallic materials. Unlike the linear shock EOS, the curve of the shock velocity versus the particle velocity is nonlinear for the bilinear shock EOS [1].

The equations describing conversation of mass, momentum and energy have too many unknowns to compute. In shock problems, the conversation equations are solved by

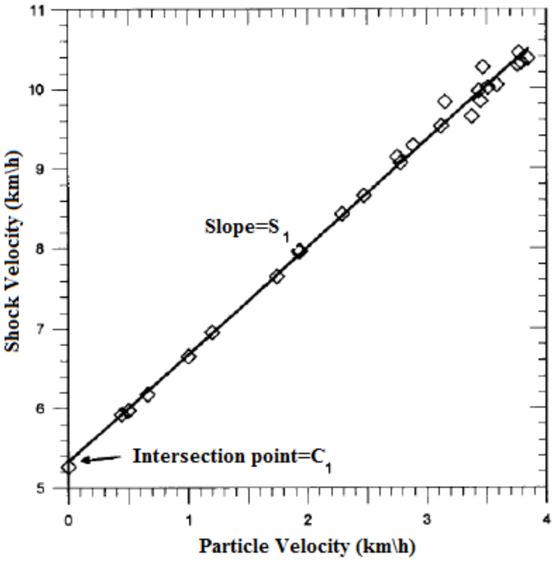

Figure 2.1: Shock Velocity-Particle Velocity plot (Aluminium 6061) [35]

the EOS. Conversation equations for solids, in the shock state, are called the Rankine-Hugoniot jump conditions [35]. The solution of these governing equations requires solutions of partial differential equations. Unlike the one-dimensional problem, it is difficult to obtain an analytical solution of the partial differential equations for the three-dimensional and complex problems. Thus, numerical methods have been developed to solve these challenging problems.

2.1.2 Jones-Wilkins-Lee (JWL) Equation of State (EOS)

This EOS is commonly used to describe the pressure-volume-energy behavior of explosive materials [27]. It is determined from dynamic experiments. Pressure function based on density is given below.

$$P = A\Big(1 - \frac{\omega \cdot \eta}{R_1}\Big)e^{-R/\eta} + B\Big(1 - \frac{\omega \cdot \eta}{R_2}\Big)e^{-R/\eta} + \omega \cdot \eta \cdot I \qquad (2.4)$$

A, B, R_1, R_2 and ω are obtained by experiments. These parameters are related to each other, so each one of them should not be changed separately. Internal energy is represented by *I*. A and B are expressed in stress units. The other parameters have no units. In the equation above, $\eta = \rho/\rho_0$ [35] .

In this thesis, the JWL EOS is used to model both Comp-B and Comp-A3. They compose certain parts of the shaped charge model. The JWL EOS is employed to simulate the detonation propagation of the shaped charge model. This EOS is the preferred choice for the jet formation analyses in the AUTODYN-Euler solver. Details are given in Chapter 3.

2.2 Strength Model

Strength model is related to the deviatoric response of a material. In this case, deformation of a material under constant volume is considered.

Many constitutive equations are proposed in the theory of ballistics. In this thesis, two prevalent equations, the Johnson-Cook and the Steinberg-Guinan strength, are used to model materials. They are described in detail below.

2.2.1 Johnson-Cook Strength

Johnson and Cook [14] developed a constitutive model and presented data for metals subjected to large strains, high strain rates and high temperatures. Johnson-Cook strength is an empirically based model. High velocity impact behavior of materials can be expressed by the Johnson-Cook Strength. The yield strength (σ) of a material is defined as

$$\sigma = [A + B \cdot \epsilon^{n}][1 + C \cdot ln\dot{\epsilon^{*}}][1 - T^{*m}] \tag{2.5}$$

Here ϵ is the equivalent plastic strain, $\dot{\epsilon^{*}}$ is the dimensionless plastic strain rate and T^{*} is the homologous temperature [14]. A, B, n, C and m are the material constants. T^{*} is defined as

$$T_{H}(\text{homologous temperature}) = \frac{T - T_{Room}}{T_{Melt} - T_{Room}} \tag{2.6}$$

Where T_{Melt} is the melting temperature and T_{Room} is the room temperature [14].

The yield strength equation is separated into three bracket groups. From left to right here, the groups are associated respectively with strain hardening, strain rate and temperature effect. Material constants are as follows: A is the yield stress, B is the hardening constant, n is the hardening exponent, C is the strain rate constant and m is the thermal softening exponent. The yield strength based on strain strain hardening can be obtained when ϵ_p^*=1 sec^{-1} and $T = T_{Room}$. When T equals to T_{Melt}, $T_H = 1$ so yield strength becomes zero. All EOS and failure models can be combined with the Johnson-Cook strength model [14].

The Johnson-Cook strength model is applied to the metal plates of the NERA and the body of the shaped charge model in the current work. Both plate and body materials are Steel 1006. The details can be seen from the following chapter.

2.2.2 Steinberg-Guinan Strength

In this strength model, both shear modulus (G) and yield stress (Y) are calculated. They are pressure and temperature dependant. Equations are given below [26].

$$G(p,T) = G_0\left(1 + \frac{G'_p}{G_0} \cdot \frac{p}{\eta^{1/3}} + \frac{G'_T}{G_0} \cdot (T - 300)\right) \tag{2.7}$$

$$Y(p,T) = Y_0 \cdot \frac{G(p,T)}{G_0} \cdot (1 + \beta_p \cdot \epsilon)^n \tag{2.8}$$

The flow stress equation is obtained when $G(p,T)$ is insert into the equation of $Y(p,T)$. This is given by:

$$Y(p,T) = Y_0\left(1 + \frac{G'_p}{G_0} \cdot \frac{p}{\eta^{1/3}} + \frac{G'_T}{G_0} \cdot (T - 300)\right) \cdot (1 + \beta_p \cdot \epsilon)^n \tag{2.9}$$

In equation (2.10), $G'_p = dG/dp$, $G'_T = dG/dT$ and $\eta = \rho/\rho_0$. In equation (2.11), ϵ is the effective plastic strain, β and n are the material parameters. Y_0 is the yield stress value at the reference state, T= 300 K and p=0 GPa. In addition, G_0 is the shear modulus value at the reference state [26].

Strain rate effects are not considered in the Steinberg Guinan Strength model [24]. When the temperature of a material is equal to or higher than the melting temperature, the yield strength and shear modulus of the material become zero [1].

There are several assumptions in the Steinberg Guinan strength. One of them is that the effect of strain rate on the yield stress of a material are insignificant when strain rate is greater than 10^5 sec^{-1}. The other assumption is that shear modulus is directly proportional to pressure. Equations for yield stress and shear modulus, including the effects of pressure, effective plastic strain and internal energy, develop with these assumptions [1].

In this thesis, the constitutive behavior of the metal parts (Cu-OFHC and Al 7075-T6) of the shaped charge is modeled using the Steinberg- Guinan strength model. The details are given in Chapter 3.

2.3 Erosion Criterion

The Johnson-Cook and the Steinberg-Guinan Strength models are flow stress models that calculate deviatoric stresses. The EOS adds volumetric effects in addition to the shape deformation (deviatoric) effects. In addition to the EOS and the strength model, a failure or a damage model can be used to model the failure state of a material. Instead of using the failure model, erosion criterion is used to carry out simulations of hypervelocity impact (over 3000 m/s) in the current thesis.

Erosion is a numerical technique for removal of the element (mesh) from the computational grid. Highly distorted elements are eroded to ensure the stability of timestep. Explicit integration is solved within the timestep. Geometric strain, one of the erosion options in AUTODYN, is chosen as an erosion criterion in the this thesis. When element geometric strain exceeds the specified value, these distorted elements are discarded.

Several tentative simulations are performed to determine the optimum value for erosion criterion. The geometric strain value of Cu-OFHC, Steel 1006 and interlayer materials was found 5 for two-dimensional numerical simulations. In addition, for three-dimensional numerical simulations, the geometric strain values of Cu-OFHC, Steel 1006 and Epoxy-Res2 were found 1.75, 1 and 1, respectively. These values are used for the simulations in the next chapters.

Material properties used in the two-dimensional and three-dimensional simulations are summarized in Table 2.1.

Table 2.1: Material properties used in the simulations

Part	Material	EOS	Strength Model
Structural part of shaped charge	Al 7075-T6	Shock	Steinberg Guinan
Booster	Comp A-3	JWL	None
Casing and metal plates	Steel 1006	Shock	Johnson Cook
Liner	Cu-OFHC	Shock	Steinberg Guinan
Explosive	Comp B	JWL	None
Intermediate Layer	Polymeric materials	Shock	None

CHAPTER 3

TWO-DIMENSIONAL ANALYSES OF SHAPED CHARGE NERA INTERACTION

This chapter focuses on the determination of an effective intermediate layer material for the NERAs. Firstly, the jet formation analysis mentioned in the previous chapter is conducted to create an appropriate jet model. The AUTODYN-Euler solver is used for the jet formation study. Then, the formed jet is transferred to the AUTODYN-Lagrange solver and simulations are conducted for the interaction between the jet and the bulging armor. Mesh size effects are also studied. Twelve inert materials are selected from the AUTODYN material library and assigned to the intermediate layer. An assessment of the bulging performance of the NERA is done using kinetic energy, momentum, velocity and pressure results. The results obtained from the simulations are comprehensively explained in this chapter.

All of the analyses mentioned in this chapter are performed with the two-dimensional solver in AUTODYN-2D. The reason for using AUTODYN-2D is to reduce the computational time. The three-dimensional solver in AUTODYN-3D requires significantly longer computation times than AUTODYN-2D.

The Eulerian and the Lagrangian meshes are used as numerical grids. In the Euler grid, the void should be defined in the geometry for which the material flows into and the grid is fixed. In other words, the mesh does not distort throughout an analysis. Under such a circumstance, the analysis gains an advantage over the long calculation time of the simulations of highly distorted materials. These highly distorted materials particularly occur in blast analyses. Therefore, the Euler grid is preferred for the jet formation analyses. In the Lagrange grid, the mesh is bonded to the material so it moves with the material. Therefore, the mesh can be severely distorted. If distortion is high, then analyses can run with very small time steps. One technique for highly distorted meshes is the erosion criteria. It is particularly utilized in the Lagrange grid. It is not a physical property of a material so the erosion criteria should be described when the strain of the material is much larger than the failure strain. If degenerated elements are not removed from an analysis, the time step can be reduced significantly and the computation time of the analysis can be extremely long. An important advantage of the Lagrange mesh is that one mesh or element includes only one material. In other words, the mesh does not encapsulate mixed materials so material interactions can be analyzed more accurately. Thus, the interactions of the jet and the bulging armor can be investigated precisely by means of the Lagrange mesh. One disadvantage of the erosion criteria is that the internal energy, the mass and the momentum of an eroded elements are always discarded.

3.1 Analyses of Shaped Charge Jet Formation

A generic shaped charge model is used for all analyses in this thesis. Dimensions and details of the shaped charge model are given in Figure 3.1. The shaped charge is modeled based on these dimensions.

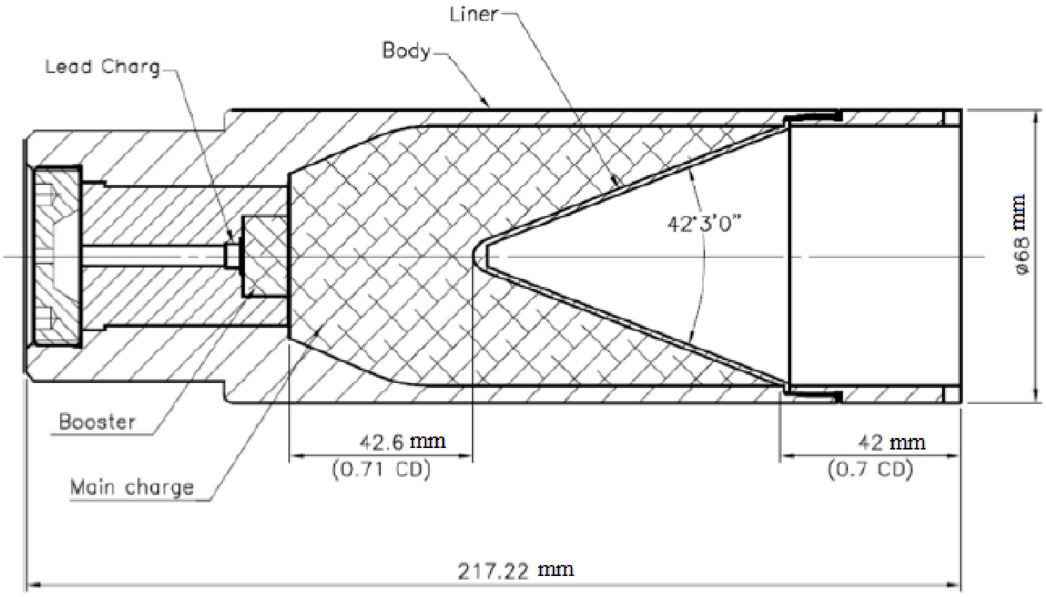

Figure 3.1: Geometry of the shaped charge

Materials of the shaped charge model are Steel 1006 (casing), Comp-B (explosive), Cu-OFHC (liner) and Comp-A3 (booster). In addition, Al 7075-T6 is selected to model one part of the main body. These materials are represented by different colors and they can be seen in Figure 3.2.

The materials used for the intermediate layer are summarized in Table 3.1. These polymeric materials and their material properties can be found in the AUTODYN material library. The density and significant shock parameters of the materials are are given in Table 3.1.

Table 3.1: Materials used for the intermediate layer and their material properties

Material	ρ_0 [g/cm^3]	C_1 [m/s]	S_1 [-]	Γ [-]
Adiprene	0.927	$2.33 \cdot 10^3$	1.536	1.48
Plexiglass	1.186	$2.60 \cdot 10^3$	1.516	0.97
Phenoxy	1.178	$2.27 \cdot 10^3$	1.698	0.55
Polycarbonate	1.200	$1.93 \cdot 10^3$	2.650	0.61
Polyethylene	0.915	$2.90 \cdot 10^3$	1.481	1.64
Poly-rubber	1.010	$0.85 \cdot 10^3$	1.865	1.50
Polyurethane	1.265	$2.49 \cdot 10^3$	1.577	1.55
Lucite	1.181	$2.26 \cdot 10^3$	1.816	0.75
Epoxy-Res	1.186	$2.73 \cdot 10^3$	1.493	1.13
Epoxy-Res2	1.186	$3.23 \cdot 10^3$	1.255	1.13
Neoprene	1.439	$2.79 \cdot 10^3$	1.419	1.39
Nylon	1.140	$2.29 \cdot 10^3$	1.630	0.87

In Figure 3.3, the shaped charge model and the void region are illustrated. The Eulerian mesh stays fixed while detonation waves are initiated and copper liner flows through the void. Except for the axis of axial symmetry, the outer edges of the void are defined with flow-out boundary condition. In this case, exploded materials can flow out the system through these boundaries and they are not calculated again in an analysis.

A mesh study is conducted for the jet formation analyses. Six different mesh sizes are taken: 0.5, 0.4, 0.25, 0.2, 0.1 and 0.08 mm. The model with 0.25 mm mesh size

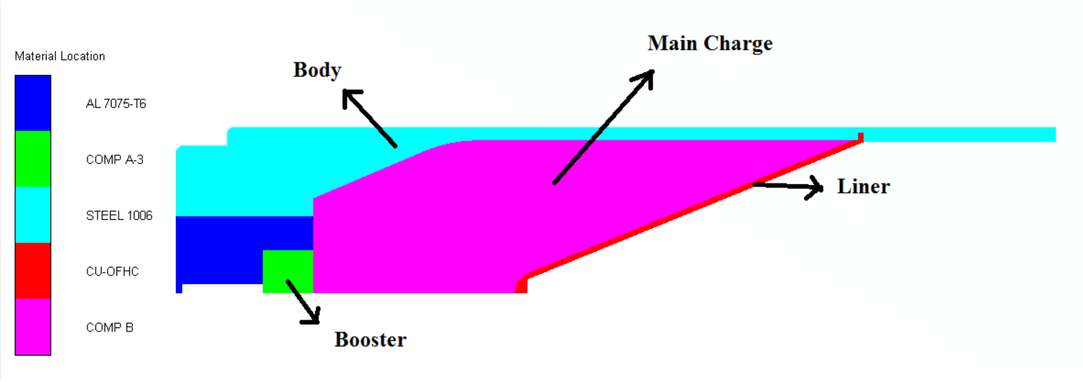

Figure 3.2: The shaped charge model is created by using ANSYS DesignModeler and AUTODYN software. The different materials of the model are represented by various of colors.

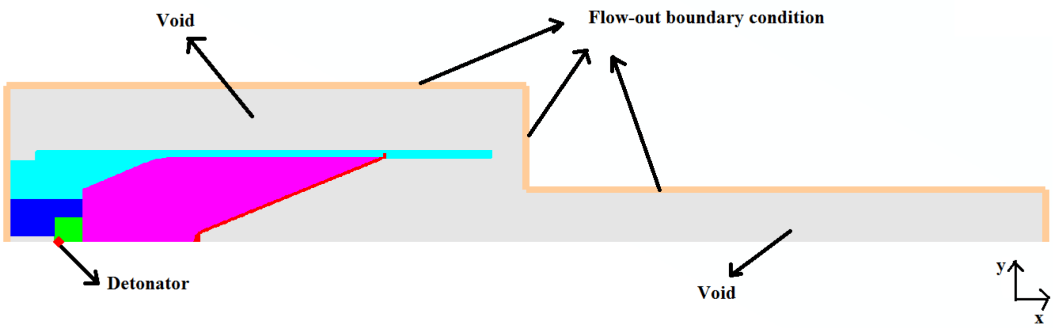

Figure 3.3: The shaped charge model together with the void region

is illustrated in Figure 3.4.

The mesh size is taken constant through the x-direction of the void region, yet in the y-direction, the mesh size of the void region is changed from a fine mesh to a coarse mesh. The fine mesh is created in the region of the jet flow. The mesh becomes coarser away from the region of the jet flow.

Two-dimensional axisymmetric behavior is selected and the jet formation analyses are conducted. Then the formed jet is transferred to the two-dimensional Lagrange solver. In this step of the analyses, planar symmetric behavior, one of the symmetry options within AUTODYN, is chosen for the Lagrangian mesh model. Planar symmetric also called plane strain behavior assumes zero strain in the z-direction. Note that the jet alone can be modeled as axisymmetric. However, in the following the jet obliquely hits the NERA and therefore an axisymmetric model is not appropriate.

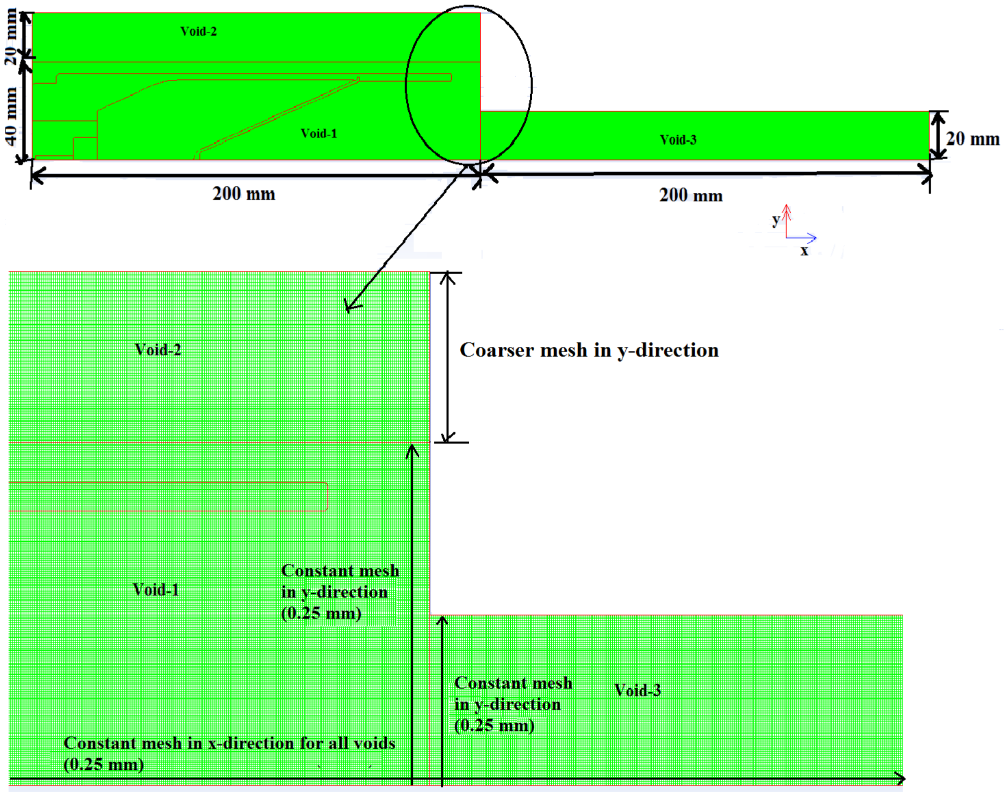

Figure 3.4: The Euler mesh model is shown for the mesh size 0.25 mm. A similar meshing strategy is followed for other mesh sizes (0.5, 0.4, 0.2, 0.1 and 0.08 mm).

3.1.1 Results of Analysis of Jet Formation

A profile line is created to measure x-velocity values along the jet as shown in Figure 3.5. This line is generated from the tail part of the jet to the tip point.

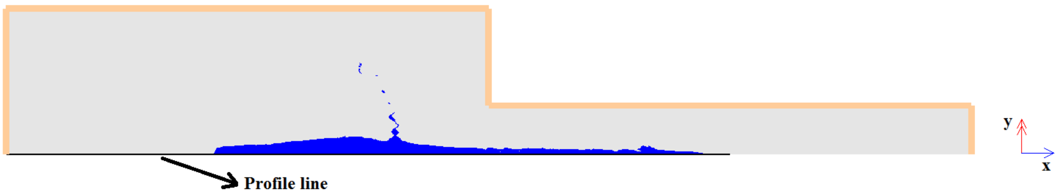

Figure 3.5: Profile line along the jet

In Figure 3.6, x-velocity distributions over the jet are given for various mesh densities. Although there are differences in the peak velocity values, the velocity profiles are very similar.

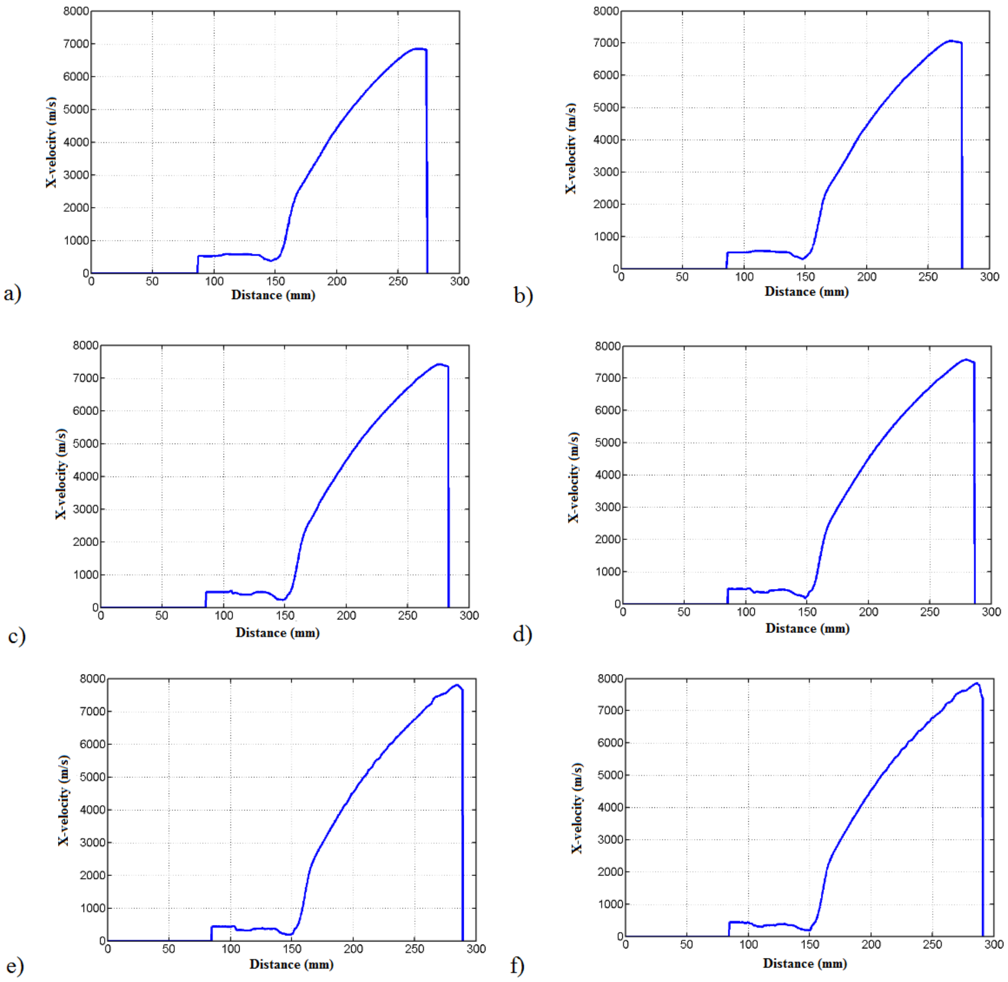

Figure 3.6: Velocity profile of the jet along the centerline for a) 0.5 mm, b) 0.4 mm, c) 0.25 mm, d) 0.2 mm, e) 0.1 mm and f) 0.08 mm.

Table 3.2: Properties of the jets computed by various mesh sizes at 40 μs

Mesh size [mm]	Jet tip distance [mm]	Jet tip velocity [mm/ μ s]	X-momentum [mg·m/s]	Total energy [mg·m^2/s^2]
0.50	273.0	6843	$1.2220 \cdot 10^8$	$2.347 \cdot 10^{11}$
0.40	277.2	7067	$1.2295 \cdot 10^8$	$2.369 \cdot 10^{11}$
0.25	283.0	7417	$1.2226 \cdot 10^8$	$2.377 \cdot 10^{11}$
0.20	286.0	7574	$1.2187 \cdot 10^8$	$2.376 \cdot 10^{11}$
0.10	288.9	7801	$1.2200 \cdot 10^8$	$2.400 \cdot 10^{11}$
0.08	290.7	7848	$1.2182 \cdot 10^8$	$2.403 \cdot 10^{11}$

Penetration of the jet model having a mesh size of 0.08 mm approximately begins at 40 μs. At that time, jet tip distance for mesh size of 0.08 mm is closest to the bulging armor. Therefore, the final state of the formed jet at 40 μs is evaluated for all mesh sizes, see Table 3.2. Also, this time is taken for transferring the jet (Euler to Lagrange). In accordance with Table 3.2, it can be concluded that the jet tip velocity depends on the mesh density. Jet tip velocity increases with decreasing mesh size. The highest velocity is obtained for the finest mesh and the lowest velocity is obtained for the coarsest mesh. A similar conclusion was reached in Gürel [8]. When the mesh size is taken 0.25 mm or smaller, tip velocity, x-momentum and total energy values do not significantly change and very similar results are achieved. Furthermore, the mass of the jet is approximately the same for all mesh sizes which is $9.7 \cdot 10^4$ mg. It is decided that the jet model having a mesh size of 0.25 mm is used for the following analyses.

The axisymmetric jet model computed with the two-dimensional Euler solver is transferred to the three-dimensional Lagrange solver for the interaction analysis of the jet and the armor. It is transferred at 40 μs. The transfer is performed for six different mesh sizes of the Lagrange solver. After the transfer, the geometry, the mass, the momentum and the kinetic energy of the jet can change. This change comes from the differences between the Eulerian mesh and the Lagrangian mesh. Note that one Eulerian element can include multiple materials, while one Lagrangian element can contain only single material. In Table 3.3, the mass, the x-momentum and the total energy of the transferred jet are shown for different mesh sizes. It can be seen from

Table 3.2 and Table 3.3 that the errors due to the transfer is acceptable for the mesh size of 0.25 mm. Smaller meshes have even lower transfer errors but they lead to high computational costs. Therefore, the mesh size of the Lagrange solver is taken 0.25 mm for the following analyses.

Table 3.3: Jet properties after transferring Euler mesh to Lagrange mesh

Mesh size [mm]	Mass [mg]	X-momentum [mg.m/s]	Total energy [mg·m^2/s^2]
0.50	$1.217 \cdot 10^5$	$1.441 \cdot 10^8$	$2.714 \cdot 10^{11}$
0.40	$1.139 \cdot 10^4$	$1.407 \cdot 10^8$	$2.633 \cdot 10^{11}$
0.25	$1.073 \cdot 10^4$	$1.312 \cdot 10^8$	$2.498 \cdot 10^{11}$
0.20	$1.072 \cdot 10^4$	$1.313 \cdot 10^8$	$2.523 \cdot 10^{11}$
0.10	$1.023 \cdot 10^4$	$1.261 \cdot 10^8$	$2.457 \cdot 10^{11}$
0.08	$1.021 \cdot 10^4$	$1.265 \cdot 10^8$	$2.475 \cdot 10^{11}$

The interaction of the jet and the armor is first analyzed using the three-dimensional Lagrange solver. It is seen that the three dimensional Lagrange solver requires a very long computational time. Therefore, the analyses for determination of intermediate layer material are conducted using the two-dimensional Lagrange solver.

3.2 Analyses of Interaction of Jet-Bulging Armor

There are many parameters affecting the interaction mechanisms of a shaped charge jet and a bulging armor. The significant parameters are as follows: The distance between a shaped charge and a bulging armor, the angle between the jet‘s flow direction and the normal of the armor, the thicknesses of each layer of the armor and various material combinations of the armor. In this thesis, the material of the intermediate layer of a bulging armor is the only varied parameter. The other parameters are taken constant.

A general schematic view of the problem considered is illustrated in Figure 3.7. The distance between the shaped charge and the bulging armor is 150 mm and the angle between the jet‘s flow direction and the normal of the armor is 60°. The bulging armor consists of three layers and the thickness of each layer is 3 mm. In Figure

3.8, the AUTODYN model for simulating the interaction of the jet with the bulging armor is shown. The bulging armor consists of three layers named as the forward moving plate (FMP), the intermediate layer and the backward moving plate (BMP). The FMP and the BMP are metallic layers and the intermediate layer is made of an inert material. While the FMP moves in the same direction with the shaped charge jet, the BMP moves in the opposite direction during the interaction.

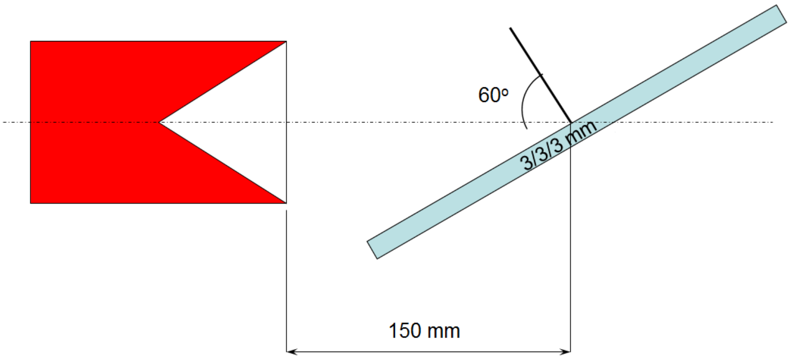

Figure 3.7: A schematic view of jet-bulging armor

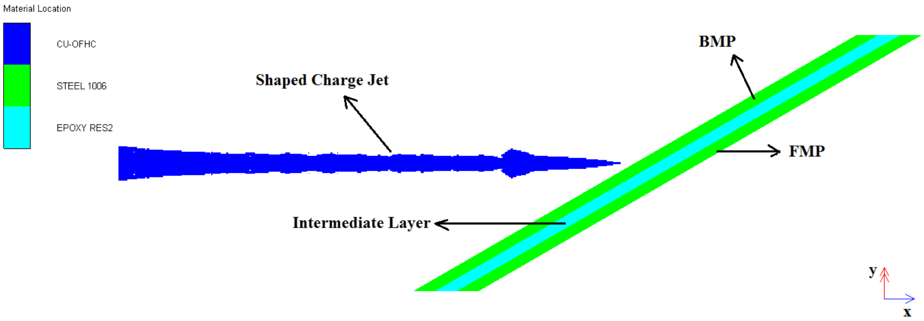

Figure 3.8: AUTODYN model for the interaction analysis of jet-bulging armor

3.2.1 Momentum, Kinetic Energy and Mass Results of the Jet

The performance of the bulging armor is based on the change of the momentums, kinetic energy and mass of the jet and the armor. Therefore, in order to understand the performance of the armor, the results for the x- and y-momentum, kinetic energy and mass of the jet and the armor are investigated. A performance comparison of the 12 interlayer materials focuses on these results.

The rates of change in the x- and y-momentum, the kinetic energy and the mass of the jet are shown in Figure 3.9 - 3.11 for 12 intermediate layer materials considered in this section. The results of the interaction analyses for adiprene, nylon, phenoxy and polycarbonate are presented in Figure 3.9.

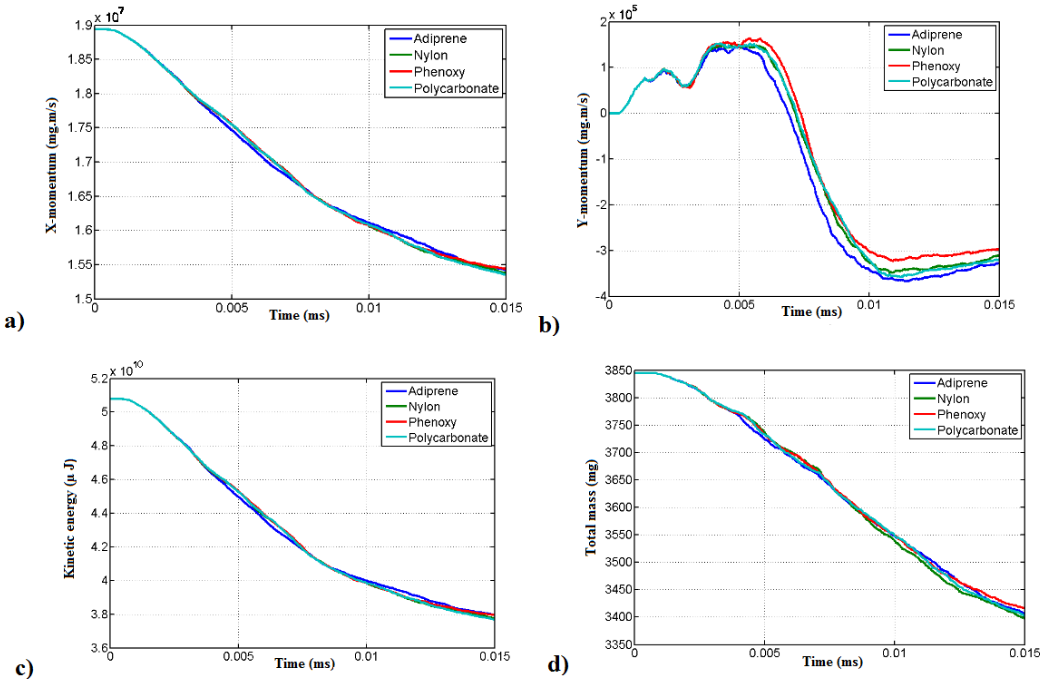

Figure 3.9: Momentum, kinetic energy and mass plots are given for the jet. Intermediate layers are adiprene, nylon, phenoxy and polycarbonate. a) x-momentum - time, b) y-momentum - time, c) kinetic energy - time and d) total mass - time

Basically, the lowering of the kinetic energy and the x-momentum of the jet means that the jet looses its penetration capacity. Evaluation of the armor performance based on only these plots might be misleading. The Lagrangian solver is used and it includes element erosion. Therefore, some part of the kinetic energy and momentum losses is due to element erosion. In Figure 3.9d, the results for the change of jet mass are shown. Note that the mass loss occurs due to the erosion of highly distorted elements and it has no physical meaning.

The momentum results for the y-direction are given in Figure 3.9b, Figure 3.10b and Figure 3.11b. It can be seen in these figures that the jet has initially zero y-momentum. Later the y-momentum of the jet changes from zero to first positive and then negative

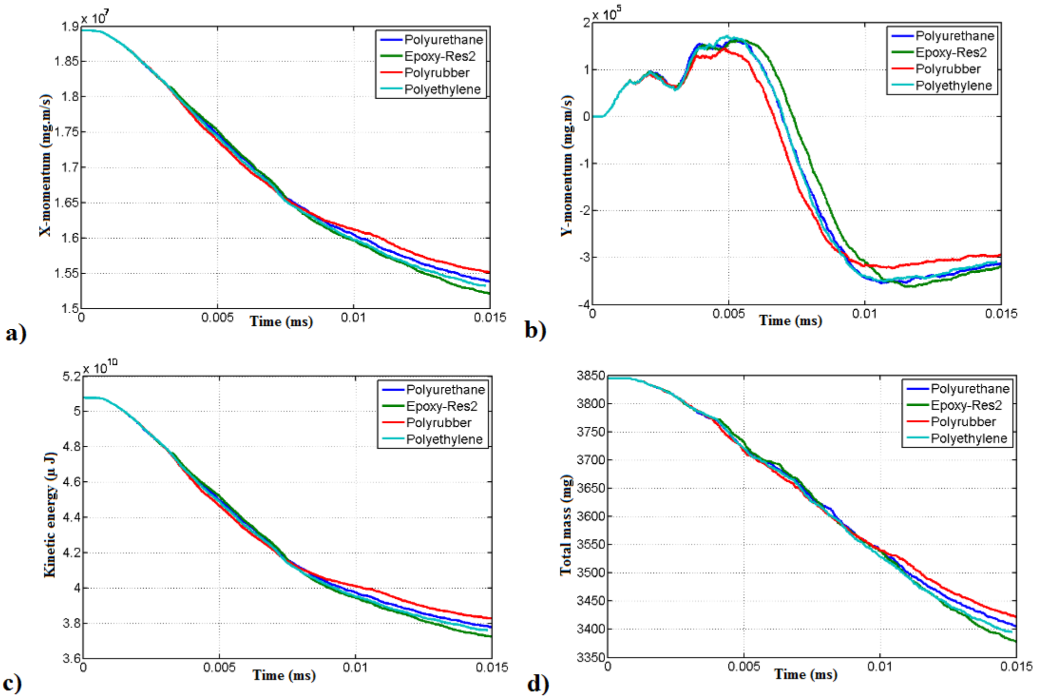

Figure 3.10: Momentum, kinetic energy and mass plots are given for the jet. Intermediate layers are polyurethane, epoxy-res2, poly-rubber and polyethylene. a) x-momentum - time, b) y-momentum - time, c) kinetic energy - time and d) total mass - time

values. This change arises from the interaction between the jet and the bulging armor. A big change of the y-momentum of the jet means that there is a strong interaction between the jet and the armor. The protection capability of the armor relates to the amount of y-momentum transfer from the plates to the jet. There is no significant difference in the x-momentum, kinetic energy and mass of the jet for all interlayer materials till 0.007 ms. On the other hand, significant differences occur after 0.0035 ms for the y-momentum of the jet.

In compliance with Figure 3.9b, Figure 3.10b and Figure 3.11b, it can be concluded that:

- In Figure 3.9b, for phenoxy, the y-momentum of the jet reaches nearly $1.6 \cdot 10^5$ mg·m/s approximately at 0.006 ms. Momentum values for other materials are lower than this. Phenoxy is the most effective material and Adiprene is the lowest effective material for jet deflection.

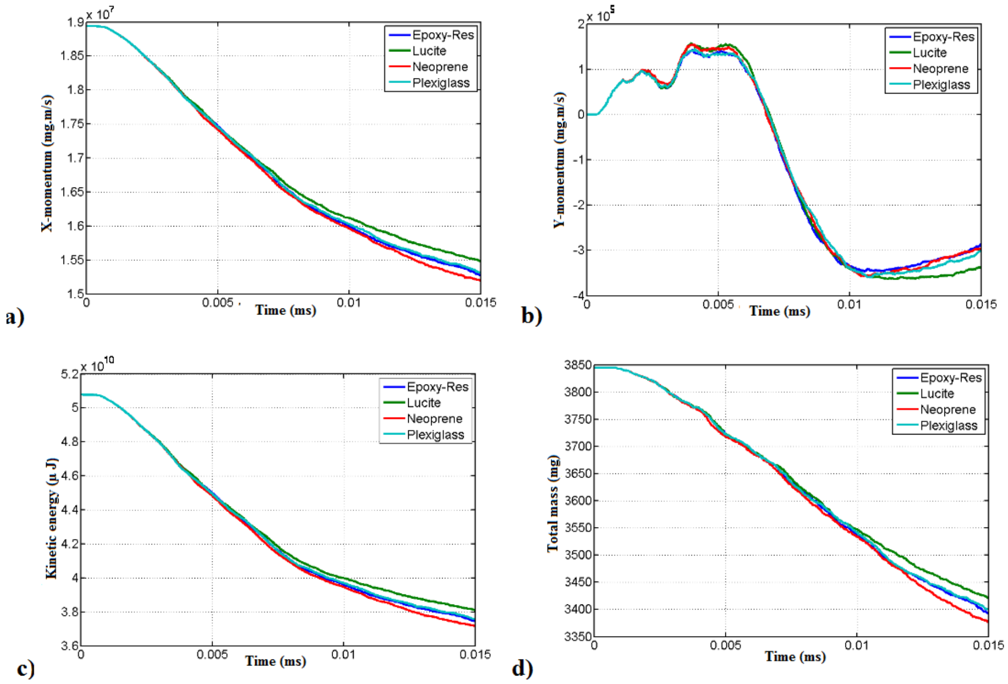

Figure 3.11: Momentum, kinetic energy and mass plots are given for the jet. Intermediate layers are epoxy-res, lucite, neoprene and plexiglass. a) x-momentum - time, b) y-momentum - time, c) kinetic energy - time and d) total mass - time

- In Figure 3.10b, for poly rubber, the y-momentum of the jet reaches nearly $1.45 \cdot 10^5$ mg·m/s approximately at 0.0045 ms. Poly rubber is the lowest effective material. The other materials' results are higher than this. Results of polyurethane, epoxy-res2 and polyethylene are similar.

- In Figure 3.11b, for neoprene and lucite, the y-momentum of the jet reaches nearly $1.55 \cdot 10^5$ mg·m/s approximately at 0.006 ms. This is the highest momentum value. The momentum values of epoxy-res and plexiglass are similar.

The results of phenoxy, polyurethane, epoxy-res2, polyethylene and neoprene are similar in terms of interlayer effectiveness against the jet. The results of the y-momentum of the jet are presented in Figure 3.12. The results are presented until 0.007 ms. To this end considering only the y-momentum gain of the jet, polyethylene is considered as the most effective intermediate layer material for jet deflection against the shape charge jet.

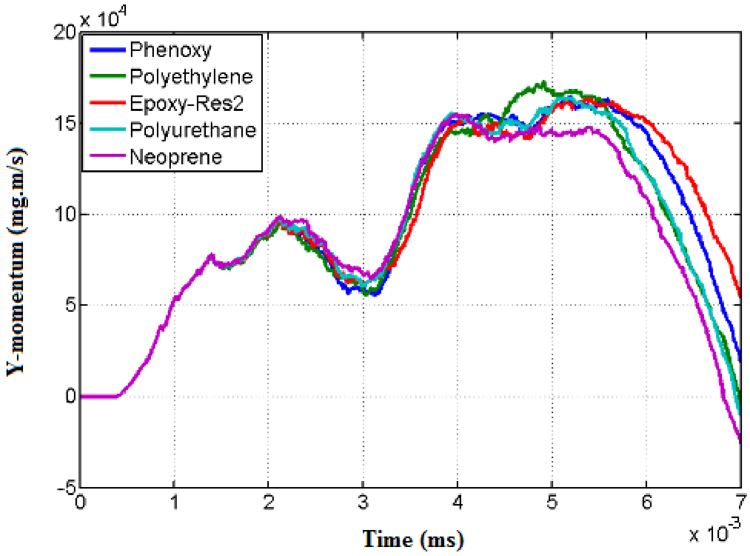

Figure 3.12: Y-momentum - time plot is given for the jet. Intermediate layers are phenoxy, polyurethane, epoxy-res2, polyethylene and neoprene.

3.2.2 Momentum, Kinetic Energy and Mass Results of the BMP

The results of the x-momentum, y-momentum and mass of the BMP, accelerated in the opposite direction to the jet, are shown in Figure 3.13, Figure 3.14 and Figure 3.15.

In Figure 3.13a, changes in the x-momentum of the BMP is given for adiprene, nylon, phenoxy and polycarbonate. Firstly, the BMP gains positive x-momentum. Then, as a result of the bulging of the intermediate layer, the x-momentum of the BMP decreases. The x-momentum of the BMP becomes zero around 0.006 ms. After that, the x-momentum becomes negative. This behavior is similar for all materials.

Figure 3.13b shows the results of the y-momentum of the BMP. Due to the inclined orientation of the BMP, the metal plate gains y-momentum. The bulging of the intermediate layer directly affects the direction of movement of the BMP

In Figure 3.13c, the change of the kinetic energy of the BMP is given. It can be seen that the kinetic energy curves are similar to the x-momentum curves. However, the kinetic energy curves do not decline to zero.

In Figure 3.13d, the mass changes of the BMP are shown. Erosion of highly distorted

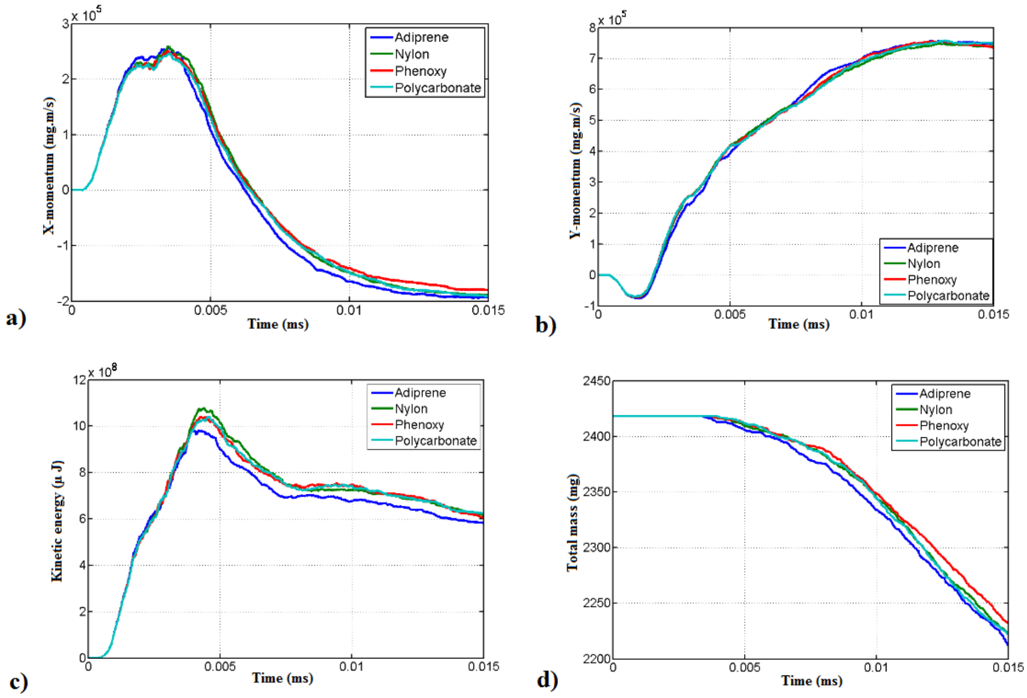

Figure 3.13: Momentum, kinetic energy and mass plots are given for the BMP. Intermediate layers are adiprene, nylon, phenoxy and polycarbonate. a) x-momentum - time, b) y-momentum - time, c) kinetic energy - time and d) total mass - time

elements results in mass loss. It is not a physical loss. Note that the percentage mass loss is higher for the jet when compared with the BMP. This is expected since the elongation of the jet causes stretching of the elements leading to the erosion in addition to the distortion of elements caused by the interaction.

In order to show the effect of the intermediate layer, only two metal plates without the intermediate layer is analyzed. The distance between two metal plates is taken 3 mm. The simulation results of this model are compared with the results of epoxy-res2 and given in Figure 3.16. In Figure 3.16, it can be seen that the BMP first gains positive x-momentum for both two models. Then, in the result of the non-interlayered model, the x-momentum decreases from nearly $3.25 \cdot 10^5$ mg·m/s to about $0.8 \cdot 10^5$ mg·m/s. On the other hand, the x-momentum decreases from nearly $2.4 \cdot 10^5$ mg·m/s to about $-2 \cdot 10^5$ mg·m/s in the result of the model consisting epoxy-res2. The results of y-momentum with respect to time are shown in Figure 3.16b. The y-momentum value reaches up to $2.25 \cdot 10^5$ mg·m/s for the non-interlayered model. However, the y-momentum of the armor (the sandwich armor), modelled with epoxy-res2, reaches up to about $8 \cdot 10^5$ mg·m/s.

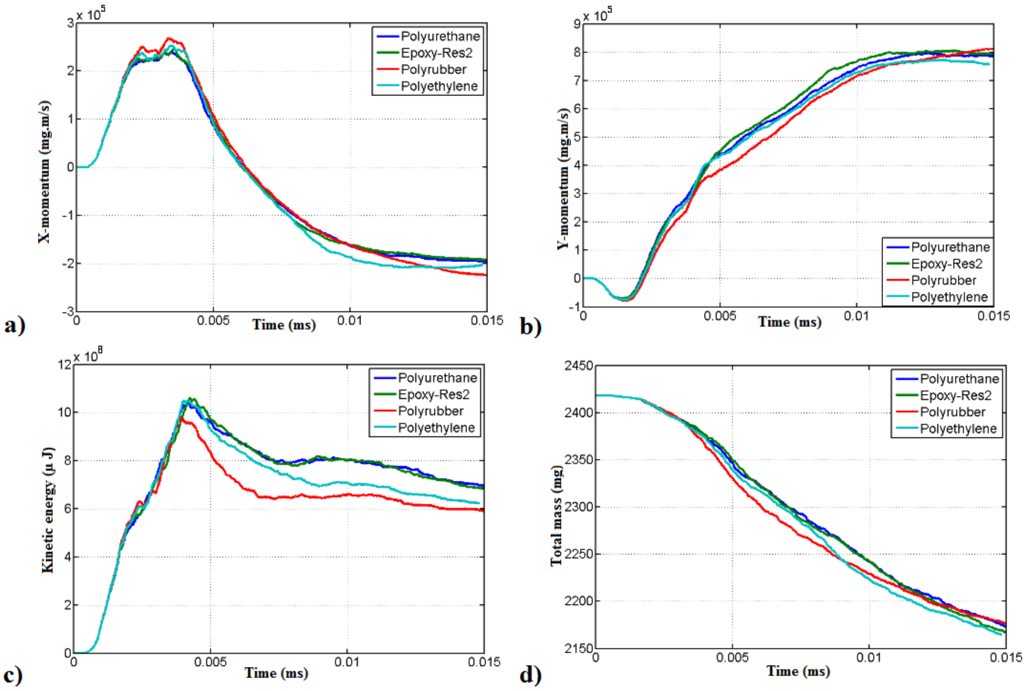

Figure 3.14: Momentum, kinetic energy and mass plots are given for the BMP. Intermediate layers are polyurethane, epoxy-res2, poly-rubber and polyethylene. a) x-momentum - time, b) y-momentum - time, c) kinetic energy - time and d) total mass - time

The x-momentum of the BMP is higher than the y-momentum value for the case when there is no material in the intermediate layer. On the other hand, when an intermediate layer is used, the y-momentum value is higher than the x-momentum. Also, a significant difference is observed in the kinetic energy results. While the kinetic energy of the armor with no intermediate layer reduces to $2.5 \cdot 10^8$ mg· m^2/s^2 at 0.015 ms, the kinetic energy of the armor with epoxy-res2 reduces only to $7 \cdot 10^8$ mg· m^2/s^2. These results clearly show that the existence of an intermediate layer significantly changes the momentum and the kinetic energy of the BMP.

From the results of Figure 3.13b, Figure 3.14b and Figure 3.15b, it can be concluded that:

- In Figure 3.13b, the effects of the interlayer materials (adiprene, nylon, phenoxy,

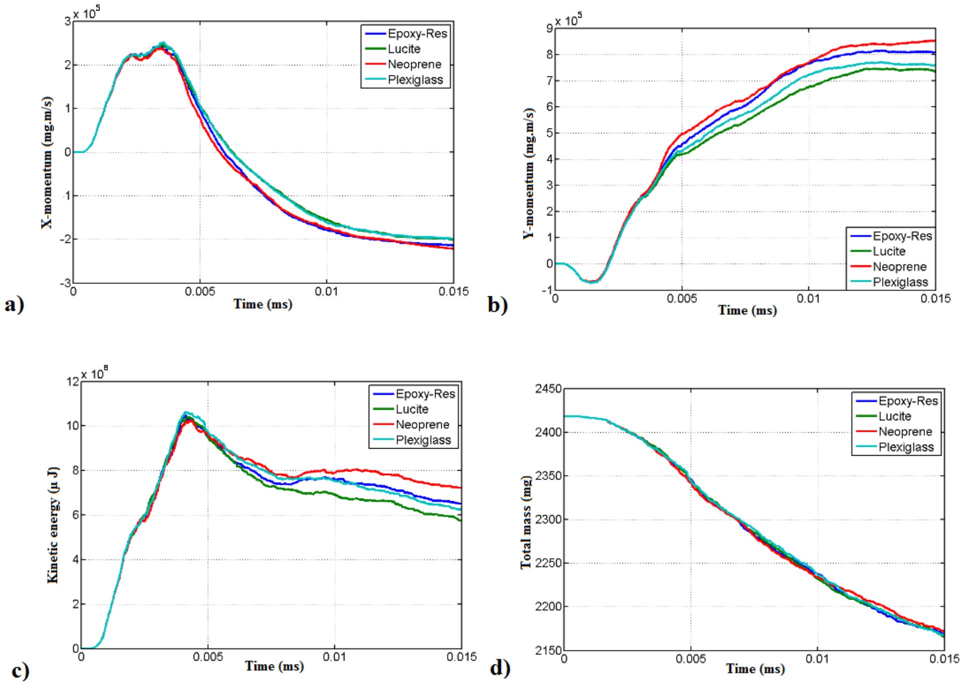

Figure 3.15: Momentum, kinetic energy and mass plots are given for the BMP. Intermediate layers are epoxy-res, lucite, neoprene and plexiglass. a) x-momentum - time, b) y-momentum - time, c) kinetic energy - time and d) total mass - time

polycarbonate) along the y-direction on the BMP are almost similar. There is no apparent difference between the y-momentum results of them.

- The y-momentum of the BMP is highest for epoxy-res2 and lowest for poly rubber. There is little difference in the performance of polyurethane and polyethylene.

- According to the result of Figure 3.15b, the y-momentum value of the BMP is the highest for neoprene and lowest for lucite.

3.2.3 Momentum, Kinetic Energy and Mass Results of the FMP

In Figure 3.17, Figure 3.18 and Figure 3.19, the results of the x-momentum, y-momentum and kinetic energy of the FMP which accelerates in the same direction as the jet are given. Like the results of the BMP, the effect of mass loss on the analyses should be taken into consideration. Even though the impact of the jet on the armor occurs along the x-direction, the FMP gains y-momentum due to the inclined placement of the armor. Additionally, the bulging of the intermediate layer also contributes

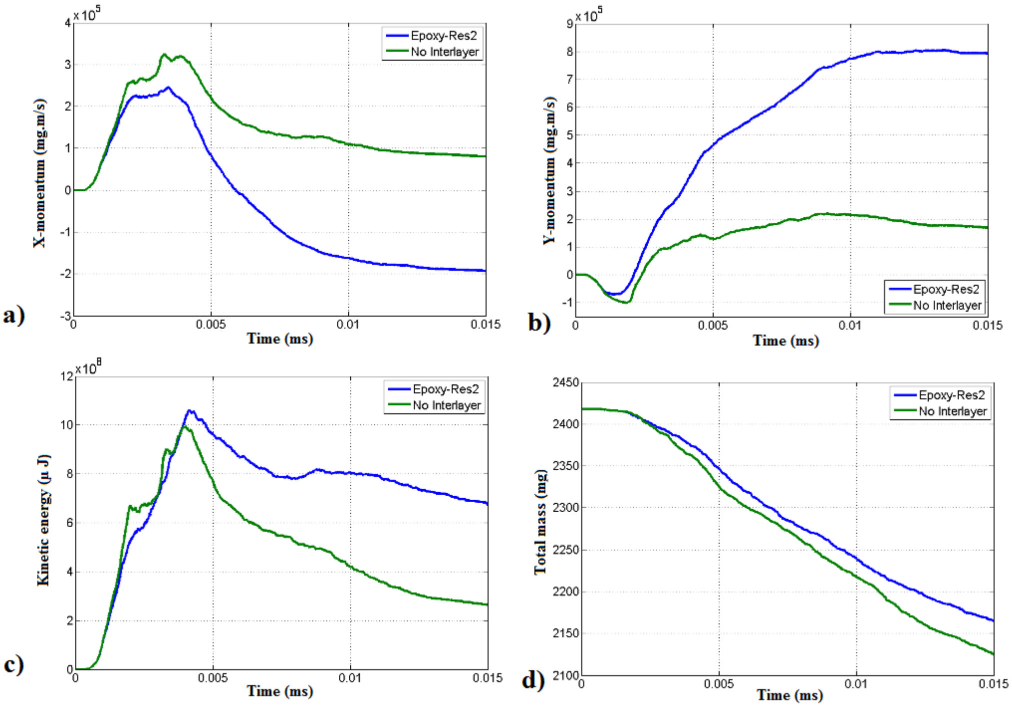

Figure 3.16: Momentum, kinetic energy and mass plots are given for the BMP. The results of the model with/without interlayer are compared with each other. These armors consist of two steel plates and void/epoxy-res2 between them. a) x-momentum - time, b) y-momentum - time, c) kinetic energy - time and d) total mass - time

to the y-momentum of the FMP.

To understand the effect of the intermediate layer, the model, mentioned before, is created with two metal plates (3 mm gap between them). The results of this model are compared with the results of epoxy-res2 and given in Figure 3.20. As seen from the x-momentum result of epoxy-res2 in Figure 3.20a, the FMP gains maximum x-momentum about $1.6 \cdot 10^6$ mg·m/s. On the other hand, the maximum x-momentum of the FMP is around $8 \cdot 10^5$ mg·m/s when there is no intermediate layer. When y-momentum results are examined on the basis of the non-interlayered model, it can be seen that the maximum y-momentums with and without an intermediate layer are about $9.5 \cdot 10^5$ mg·m/s and $4.5 \cdot 10^5$ mg·m/s, respectively. Similarly the maximum kinetic energies with an intermediate layer and without an intermediate layer are about $3.7 \cdot 10^9$ mg·m^2/s^2 and $2.2 \cdot 10^9$ mg·m^2/s^2, respectively.

In compliance with these results, it can be seen that the x-momentum, y-momentum and kinetic energy of the FMP in the sandwich model are higher when there is an in-

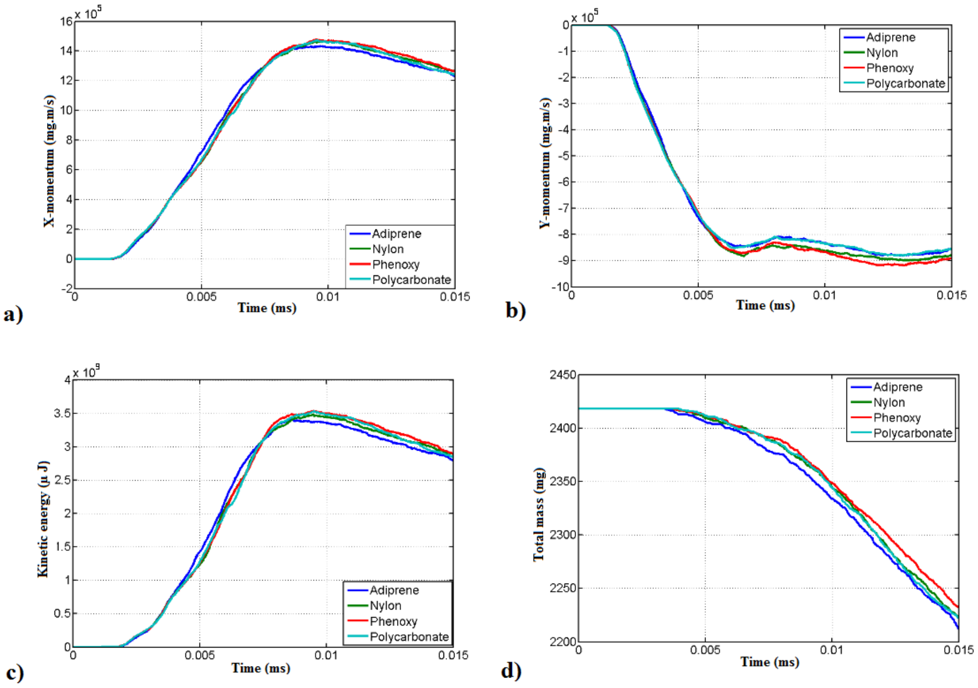

Figure 3.17: Momentum, kinetic energy and mass plots are given for the FMP. Intermediate layers are adiprene, nylon, phenoxy and polycarbonate. a) x-momentum - time, b) y-momentum - time, c) kinetic energy-time and d) total mass-time

termediate layer material. The bulging of the intermediate layer causes the differences in the results.

From the results of Figure 3.17b, Figure 3.18b and Figure 3.19b, it can be concluded that:

- In Figure 3.17b, it can be seen that higher momentums in the y-direction are achieved by using nylon and phenoxy as an intermediate layer. Adiprene and polycarbonate have the lowest effect on the y-momentum of the FMP.

- According to Figure 3.18b, epoxy-res2 causes a higher y-momentum of the FMP. On the other hand the lowest y-momentum is obtained by poly rubber. Polyurethane and polyethylene lead to performances between polyrubber and epoxy-res2.

- In Figure 3.19b, it can be seen that neoprene causes a higher y-momentum of the FMP. The lowest y-momentum is obtained by lucite.

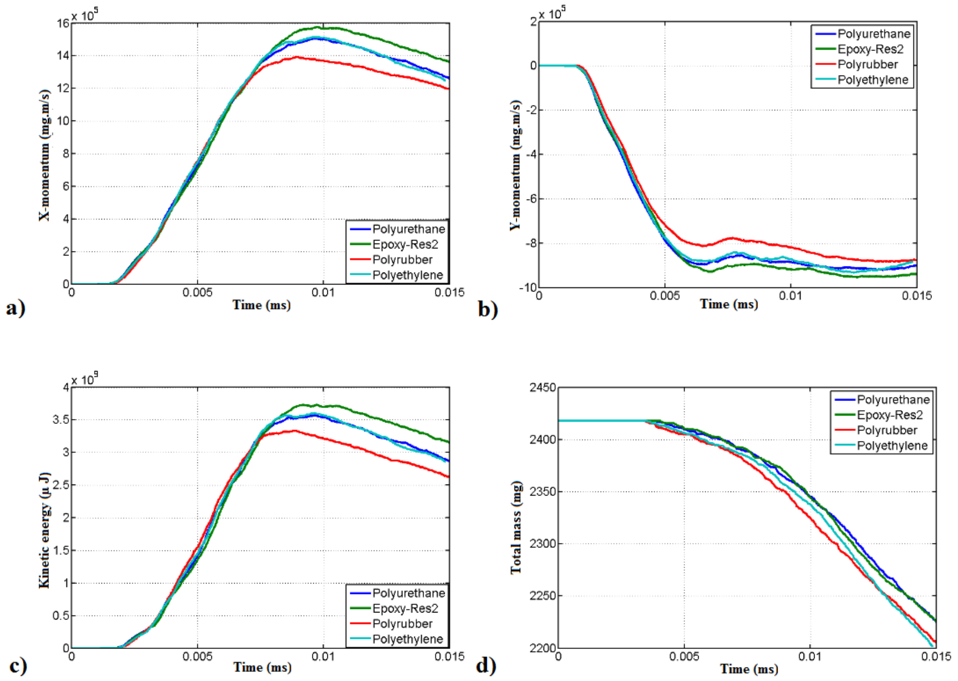

Figure 3.18: Momentum, kinetic energy and mass plots are given for the FMP. Intermediate layers are polyurethane, epoxy-res2, poly-rubber and polyethylene. a) x-momentum - time, b) y-momentum-time, c) kinetic energy-time and d) total mass-time

3.2.4 Velocity Results of Gauge Points on the Jet

To investigate the interactions between the jet and the armor in detail, gauge points are created on the jet and metal plates. Total number of gauge points are 46. They are shown in Figure 3.21.

Velocity-time plots of the gauge points are presented in Figure 3.22 - 3.27. These figures show the changes of the x- and y-velocity of the gauge points. Deceleration of the jet in the x-direction is related to the interaction between the jet and the sandwich armor. On the other hand, the obliquity of the armor and the bulging effect cause acceleration of the jet in the y-direction. The changes in the x- and y-velocity can be related to the armor performance against the jet. In other words, more reduction in x-velocity and higher change in y-velocity (in absolute sense) indicate a better armor performance.

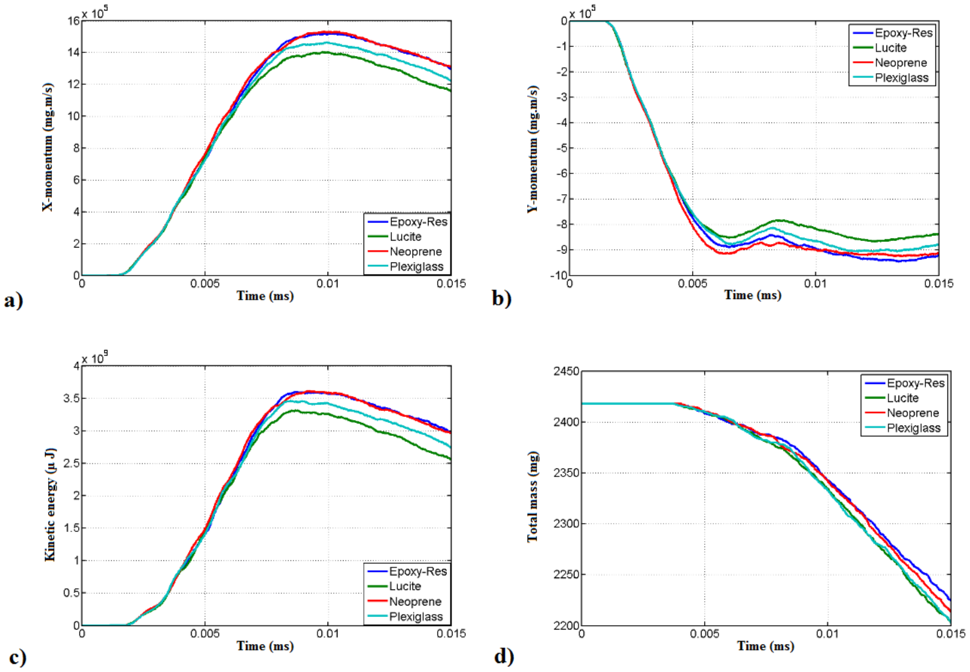

Figure 3.19: Momentum, kinetic energy and mass plots are given for the FMP. Intermediate layers are epoxy-res, lucite, neoprene and plexiglass. a) x-momentum - time, b) y-momentum - time, c) kinetic energy - time and d) total mass - time

In Figure 3.22, the results for the x- and y-velocity of the gauge points 10 and 11 are presented. According to Figure 3.22a, after 9 microseconds, the x-velocity of the gauge point 10 becomes the lowest for polycarbonate. The x-velocity values of the gauge point 10 are the highest for adiprene after 12 microseconds. According to Figure 3.22b, after 11 microseconds, the highest and lowest y-velocity values are obtained with phenoxy and adiprene, respectively. In Figure 3.22c, after 9 microseconds, the x-velocity of the gauge point 11 reaches the lowest values for phenoxy. Moreover, the x-velocity values are the highest for polycarbonate and nylon. On the other hand, it can be seen in Figure 3.22d that the highest y-velocity results for the gauge point 11 are obtained with polycarbonate after 7.5 microseconds. The y-velocity values of the gauge point 11 are the lowest for adiprene and nylon after 7.5 microseconds.

In Figure 3.23a and Figure 3.23b, the results for the x- and y-velocity of the gauge point 12 are presented for the interlayer materials adiprene, nylon, phenoxy and polycarbonate. Differences among four curves start around at about 1.9 microseconds.

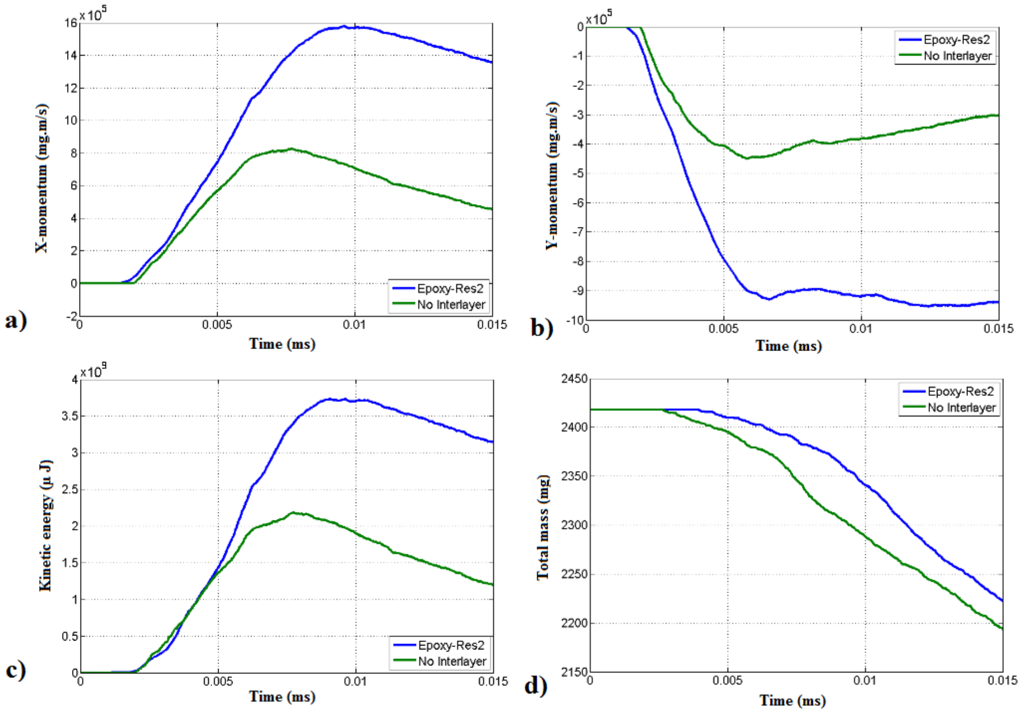

Figure 3.20: Momentum, kinetic energy and mass plots are given for FMP. The results of the model with/without interlayer are compared with each other. These armors consist of two steel plates and void/epoxy-res2 between them. a) x-momentum - time, b) y-momentum - time, c) kinetic energy - time and d) total mass - time

In compliance with Figure 3.23a, the initial x-velocity of the gauge point 12 is approximately equal to 7500 m/s. Then, the x-velocity drops dramatically to about 5000 m/s. After 2 microseconds, the velocity curves of the gauge point 12 fluctuate due to the interaction of the jet with the bulging armor. Around 3 microseconds, the gauge point 12, fixed on an element, is eroded instantaneously because of distortion of the element. As can be seen in Figure 3.23b, the y-velocity of the gauge point 12 first increases and then drops to zero. Then, the gauge point 12 starts to accelerate in the negative y-direction at about 2.25 microseconds. The wild oscillations in the y-velocity curve make performance comparisons of the interlayer materials difficult. The results of the x- and y-velocity of the gauge point 13, placed very close to the tip of the jet, are shown in Figure 3.23c and Figure 3.23d. The intermediate layer materials are adiprene, nylon, phenoxy and polycarbonate. In compliance with these figures, the same velocity-time curve is obtained with all interlayer materials. The initial x-velocity of the jet is approximately 7500 m/s. Between 0.8 and 1.2 microseconds, the x-velocity of the gauge point 13 decreases to about 3000 m/s. Then, the

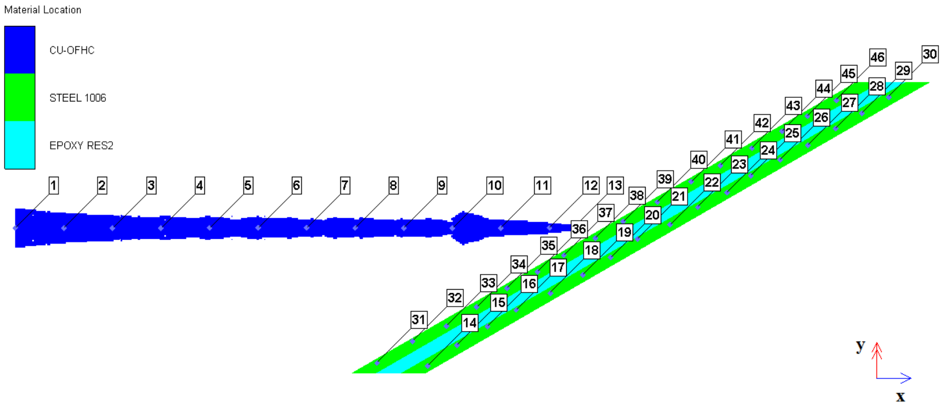

Figure 3.21: Gauge points on the jet and steel plates

x-velocity value suddenly goes to zero due to erosion of a highly distorted element. It can be seen in Figure 3.23d that the y-velocity of the gauge point 13 starts to increase at about 0.6 microseconds. This velocity value approximately equals to 1200 m/s at about 1.05 microseconds. Then, the y-velocity value decreases and goes to zero. The gauge point 13 is eroded at around 1.2 microseconds. It can be concluded that the bulging effect of the intermediate layer cannot be determined from the results of the gauge point 13 due to the erosion.

In Figure 3.24a and Figure 3.24b, the velocity results of the gauge point 10 are presented. Interlayer materials are polyurethane, epoxy-res2, poly-rubber and polyethylene. According to these figures, the maximum reduction in x-velocity and the maximum increase in y-velocity of the gauge point 10 are achieved with epoxy-res2. An opposite performance is obtained for polyrubber. In other words, the most and least effective materials are respectively epoxy-res2 and polyrubber. In Figure 3.24c and Figure 3.24d, the results of the x- and y-velocity of the gauge point 11 are shown. In compliance with Figure 3.24c, the x-velocity of the gauge point 11 decreases, reaching its lowest values in the curve of epoxy-res2. In other words, epoxy-res2 provides a better protection than the other interlayer materials. On the other hand, polyurethane provides the least protection. The highest y-velocity of the gauge point 11 is obtained with polyethylene and epoxy-res2. Similar to the results of x-velocity, the least effective material is found as polyurethane.

The results of the x- and y-velocity of the gauge point 12 are given for the interlayer

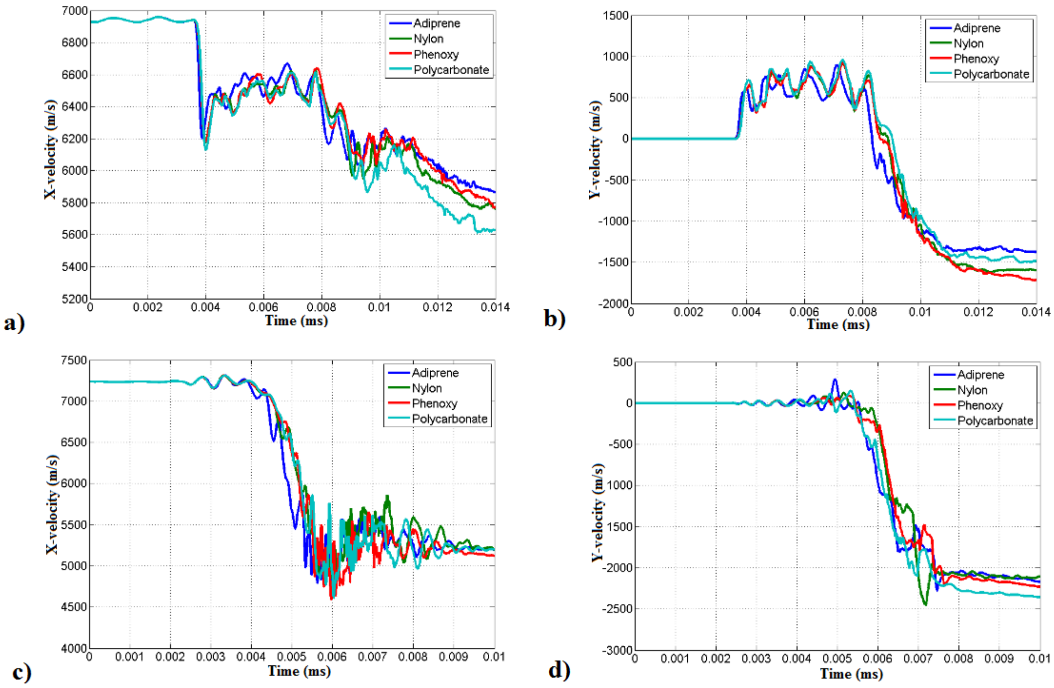

Figure 3.22: Velocity - time plots are given for gauge points on the jet. Intermediate layers are adiprene, nylon, phenoxy and polycarbonate. a) x-velocity of point 10, b) y-velocity of point 10, c) x-velocity of point 11 and d) y-velocity of point 11.

materials polyurethane, epoxy-res2, poly rubber and polyethylene in Figure 3.25a and Figure 3.25b. The curves in general look like the curves of adiprene, nylon, phenoxy and polycarbonate. Due to the strong fluctuations in the x- and y-velocity curves performance comparisons of the interlayer materials are difficult. The results of the x- and y-velocity of the gauge point 13 are given in Figure 3.24c and Figure 3.24d. As in the case of Figure 3.23c and Figure 3.23d, the velocity-time curve is same for all interlayer materials.

In Figure 3.26a and Figure 3.26b, the results of the x- and y-velocity of the gauge point 10 are presented. Interlayer materials are epoxy-res, lucite, neoprene and plexiglass. It can be seen in Figure 3.26a that the x-velocity of the jet falls down to the lowest velocities at about 11 microseconds for neoprene. Lucite is the least effective material due to higher x-velocity values of the jet. In Figure 3.26b, it can be seen that all interlayers materials show similar behavior for the y-velocity of gauge point 10. Therefore, a comparison of the performances of the interlayers is not possible.

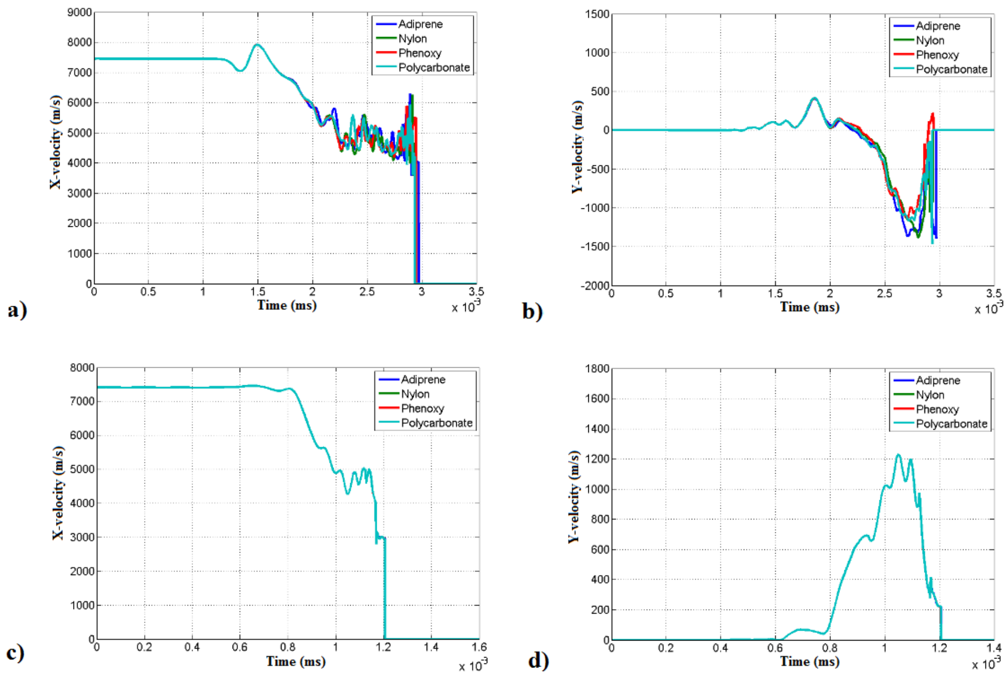

Figure 3.23: Velocity - time plots are given for gauge points on the jet. Intermediate layers are adiprene, nylon, phenoxy and polycarbonate. a) x-velocity of point 12, b) y-velocity of point 12, c) x-velocity of point 13 and d) y-velocity of point 13.

The changes of the x- and y-velocity of the gauge point 11 are shown in Figure 3.26c and Figure 3.26d. After 7 microseconds, differences among the velocity curves can be clearly seen. In other words, a comparison of the performances of interlayer materials can be made easily. The largest velocity reduction in the x-direction is obtained with epoxy-res. On the other hand, the smallest velocity reduction is achieved with lucite. Epoxy-res is also the most effective interlayer material for the jet deflection in the y-direction. Lucite is the least effective interlayer among four materials considered.

In Figure 3.27a and Figure 3.27b, the changes of the x- and y-velocity of the gauge point 12 are shown. Interlayer materials are epoxy-res, lucite, neoprene and plexiglass. Strongly fluctuating curves are obtained from simulations so comparison of the interlayer materials are not made clearly. The results for the x- and y-velocity of the gauge point 13 are presented in Figure 3.27c and Figure 3.27d. Similar to the previous results of the gauge point 13, there is no difference in the velocity results of the interlayer materials.

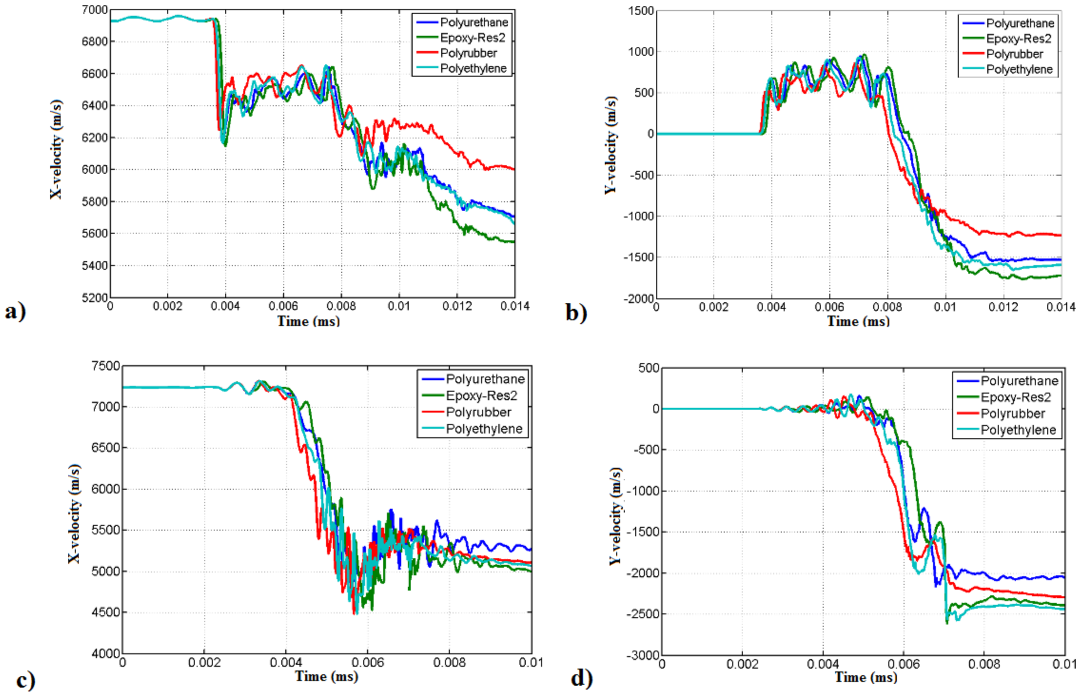

Figure 3.24: Velocity-time plots are given for gauge points on the jet. Intermediate layers are polyurethane, epoxy-res2, poly-rubber and polyethylene. a) x-velocity of point 10, b) y-velocity of point 10, c) x-velocity of point 11 and d) y-velocity of point 11.

From the results of Figure 3.22 - 3.26, it can be concluded that:

- The velocity results of the gauge point 12 and the gauge point 13 do not provide useful information about the effectiveness of the armor against the jet.

- According to the results of the y-velocity of the gauge point 11, the velocity values are higher for polycarbonate, epoxy-res2, polyethylene and epoxy-res. These results can be seen in Figure 3.22d, Figure 3.24d and Figure 3.26d. On the other hand, intermediate layer materials, epoxy-res2, phenoxy, polyethylene and epoxy-res, decrease the x-velocity of the jet more than the other interlayer materials. The results of the x-velocity of the gauge point 11 are given in Figure 3.22c, Figure 3.24c and Figure 3.26c.

- In accordance with the results of the y-velocity of the gauge point 10, epoxy-res2 and phenoxy are the most effective interlayer materials for the armor. The performances

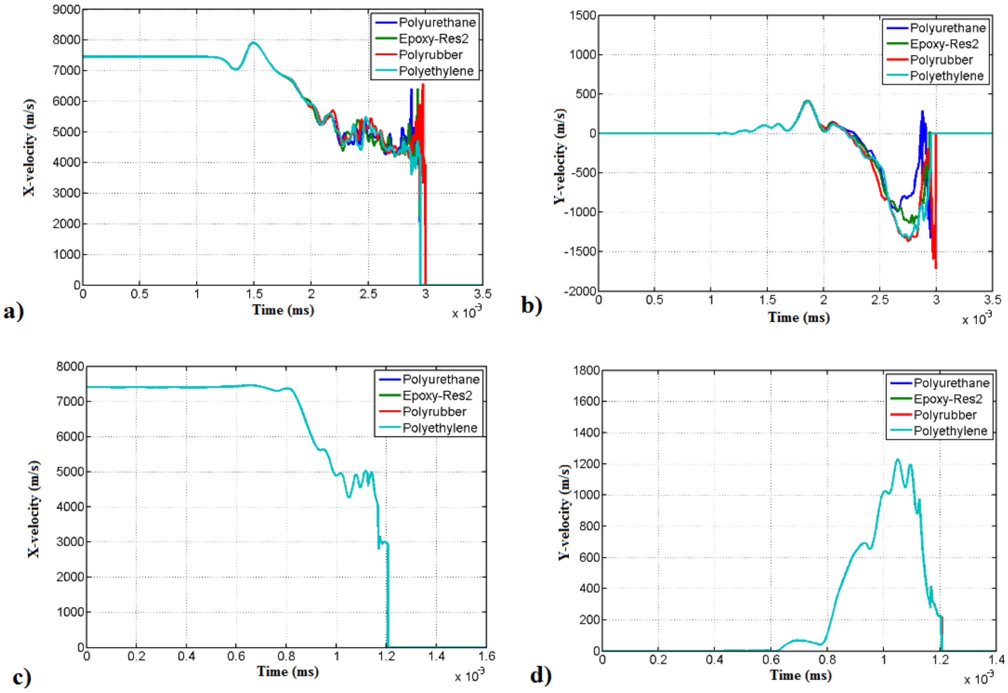

Figure 3.25: Velocity-time plots are given for gauge points on the jet. Intermediate layers are polyurethane, epoxy-res2, poly-rubber and polyethylene. a) x-velocity of point 12, b) y-velocity of point 12, c) x-velocity of point 13 and d) y-velocity of point 13.

of the interlayer materials can be seen in Figure 3.22b, Figure 3.24b and Figure 3.26b. On the other hand, performances of neoprene, epoxy-res2 and polcarbonate are the better when the reduction of x-velocity of the jet is considered. The performances of the interlayer materials are shown in Figure 3.22a, Figure 3.24a and Figure 3.26a.

3.2.5 Velocity Results of Gauge Points on the BMP

To investigate the behavior of the BMP during the interaction of the jet with the bulging armor, gauge points are placed on the BMP. As can be seen in Figure 3.21, these are the gauge points 37, 38, 39 and 40. In Figure 3.28 - 3.33, velocity results of the gauge points are given for different interlayer materials. In Figure 3.28 and Figure 3.29, the interlayer materials are adiprene, nylon, phenoxy and polycarbonate. In Figure 3.30 and Figure 3.31, the interlayer materials are polyurethane, epoxy-res2, poly-rubber and polyethylene. In Figure 3.32 and Figure 3.33, the interlayer materials are epoxy-res, lucite, neoprene and plexiglass. For a better performance of NERA, the

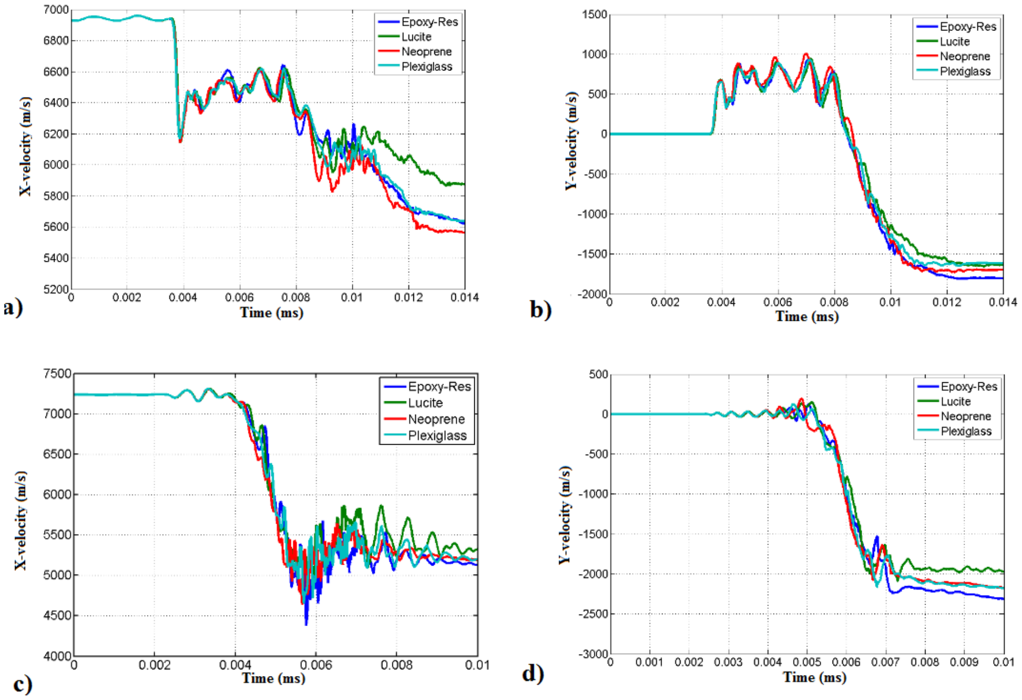

Figure 3.26: Velocity-time plots are given for gauge points on the jet. Intermediate layers are epoxy-res, lucite, neoprene and plexiglass. a) x-velocity of point 10, b) y-velocity of point 10, c) x-velocity of point 11 and d) y-velocity of point 11.

gauge points should reach higher velocities in the negative x-direction. Furthermore, they should gain higher velocity in either the positive or the negative y-direction.

In Figure 3.28a and Figure 3.28b, the plots of the x- and y-velocity of the gauge point 37 are presented. The highest and lowest velocity values for the negative x-direction are achieved with polycarbonate and adiprene, respectively. In addition, the curve of nylon is very similar to the curve of phenoxy. In the y-velocity plots, based on the initial acceleration of the gauge point, the most effective interlayer is polycarbonate. Changes of the x- and y-velocity of the gauge point 38 are presented in Figure 3.28c and Figure 3.28d. While the gauge point 38 is first accelerated in the negative x-direction, it moves in positive x-direction afterwards. Due to the highly distorted meshes, the gauge point 38 are eroded at about 6.8 microseconds. For this reason, the plot of the x-velocity of the gauge point 38 is not useful to identify the performance of the armor. In Figure 3.28d, it can be seen that the gauge point 38 is accelerated first in the negative and then in the positive y-direction. Similar to the results of the gauge point 37, the highest and lowest velocity values in the y-direction are obtained

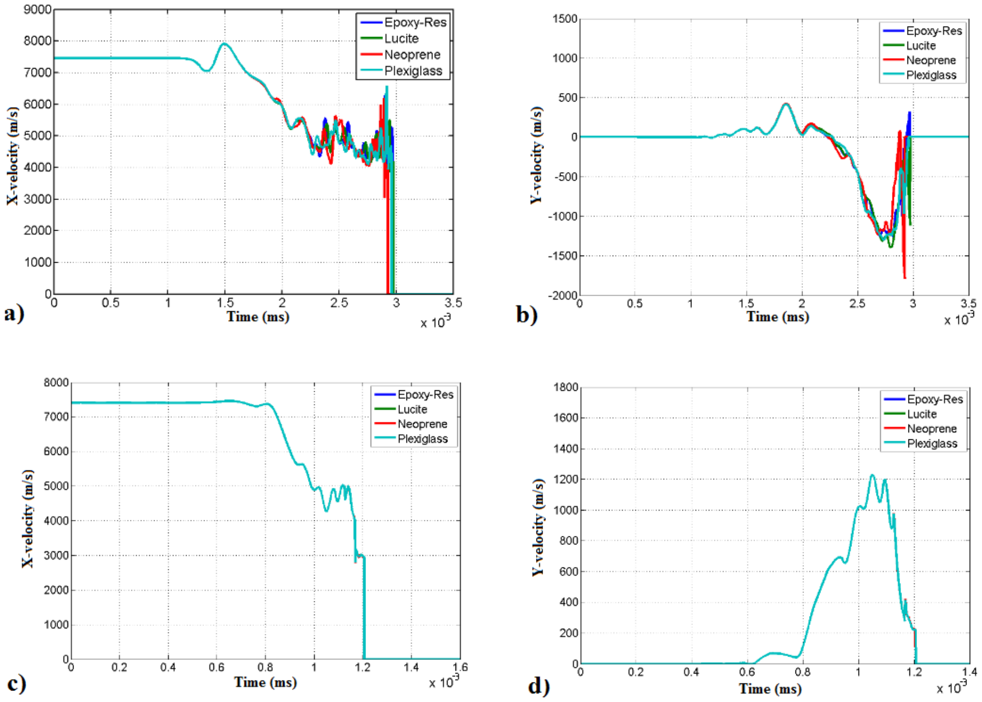

Figure 3.27: Velocity-time plots are given for gauge points on the jet. Intermediate layers are epoxy-res, lucite, neoprene and plexiglass. a) x-velocity of point 12, b) y-velocity of point 12, c) x-velocity of point 13 and d) y-velocity of point 13.

with polycarbonate and adiprene, respectively.

In Figure 3.29a and Figure 3.29b, the plots of the x- and y-velocity of the gauge point 39 are shown. The effects of the interlayer materials on the performance of the armor cannot be determined from the results of the x-velocity of the gauge point 39. On the other hand, it can be seen in Figure 3.29b that the bulging performance of adiprene against the jet is the lowest when compared with others. The performance differences of the interlayer materials start to occur after 2.5 microseconds. The x and y components of the velocity of the gauge point 40 are shown in Figure 3.29c and Figure 3.29d. As can be seen in Figure 3.29c, this gauge point is accelerated in the positive x-direction and decelerated. Then, it moves in the negative x-direction due to the bulging of the armor. According to the x-velocity result, especially after 6.8 microseconds, the velocity of the gauge point 40 is the lowest for phenoxy. The velocity values obtained for nylon, adiprene and polycarbonate are similar. In Figure 3.29d, it can be seen that while the y-velocity of the gauge point 40 is the lowest for adiprene, velocity results of nylon, phenoxy and polycarbonate are very similar.

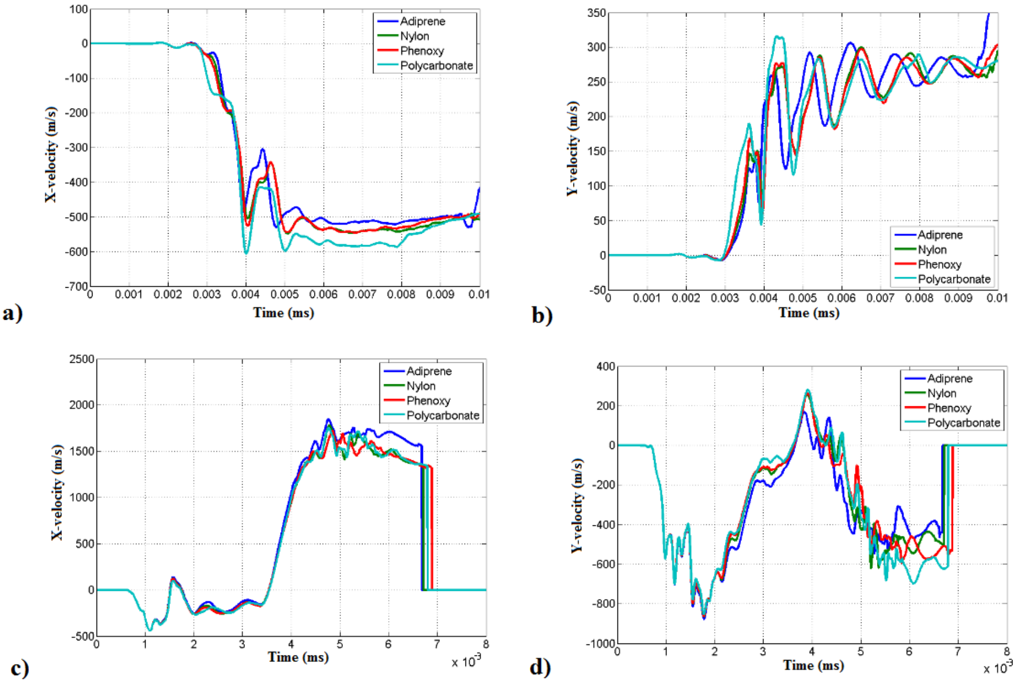

Figure 3.28: Velocity - time plots are given for gauge points on the BMP. Intermediate layers are adiprene, nylon, phenoxy and polycarbonate. a) x-velocity of point 37, b) y-velocity of point 37, c) x-velocity of point 38 and d) y-velocity of point 38.

In Figure 3.30a and Figure 3.30b, results of the velocity components of the gauge point 37 are shown for polyurethane, epoxy-res2, poly-rubber and polyethylene interlayers. The x-velocity of the gauge point 37 is higher for epoxy-res2. According to the x- and y-velocity results of the gauge point 37, the performance is the worst for poly-rubber. The changes of the y-velocity of the gauge point are similar for the other three materials.

In Figure 3.30c and Figure 3.30d, the velocity results of the gauge point 38 are given. According to Figure 3.30c the performance of polyethylene seems superior than the others. In Figure 3.30d, it can be seen that the effect of different interlayer materials on the gauge point 38 particularly occurs after 1.8 microseconds. The effect of bulging on the BMP is maximum at about 4 microseconds. The highest y-velocity values of the gauge point 38 are obtained with polyurethane and epoxy-res2. Furthermore, the lowest y-velocity is obtained with poly-rubber.

The velocity results of the gauge point 39 are presented in Figure 3.31a and Figure

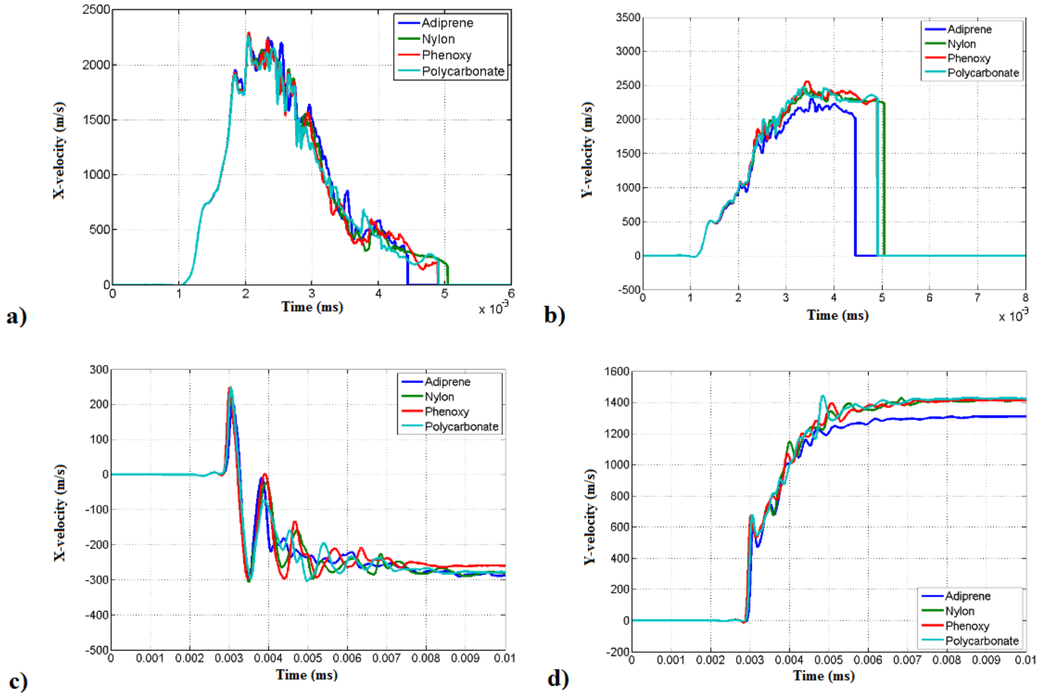

Figure 3.29: Velocity - time plots are given for gauge points on the BMP. Intermediate layers are adiprene, nylon, phenoxy and polycarbonate. a) x-velocity of point 39, b) y-velocity of point 39, c) x-velocity of point 40 and d) y-velocity of point 40.

3.31b. Like the x-velocity results of the gauge point 38, the bulging performances of the interlayers are not clear in Figure 3.31a. In the y-velocity plot of the gauge point 39, it can be seen that velocity values are the highest for epoxy-res2 and polyurethane. On the other hand, the bulging performance of the armor is the lowest for poly-rubber.

In Figure 3.31c and Figure 3.31d, the results of the velocity components of the gauge point 40 are shown. It can be seen in the x-velocity plot that the BMP gains the highest velocity in the negative x-direction when polyurethane or epoxy-res2 is used in the armor. As can be seen from Figure 3.31d the gauge point 40 reaches to highest y-velocities for polyurethane and epoxy-res2.

In Figure 3.32a and Figure 3.32b, the velocity results of the gauge point 37 are given for epoxy-res, lucite, neoprene and plexiglass. In the x-velocity plot, the highest and lowest negative x-velocity values are obtained with neoprene and plexiglass, respectively. According to the y-velocity plot, especially after 3.9 microseconds, lucite is the lowest effective interlayer.

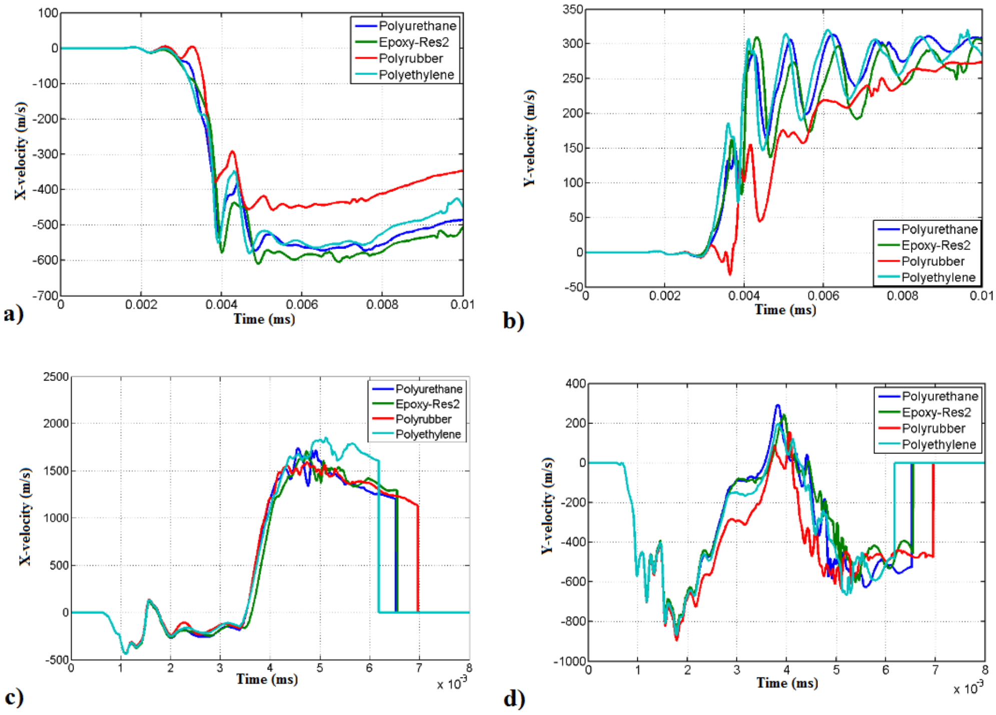

Figure 3.30: Velocity-time plots are given for gauge points on the BMP. Intermediate layers are polyurethane, epoxy-res2, poly-rubber and polyethylene. a) x-velocity of point 37, b) y-velocity of point 37, c) x-velocity of point 38 and d) y-velocity of point 38.

The results of the velocity components of the gauge point 38 are shown in Figure 3.32c and Figure 3.32d. Similar to the results of the interlayers mentioned before, the gauge point is accelerated in positive x-direction. This acceleration starts after 3.6 microseconds. The plot is not clear for comparison of the performance of the interlayers. In accordance with the y-velocity plot, it can be concluded that there is not a strong difference in the bulging performances of the interlayers.

The velocity results of the gauge point 39 are shown in Figure 3.33a and Figure 3.33b. Similar to previous cases, it is not possible to make a comparison of the bulging performance of the interlayers based on solely the x-velocity of the gauge point 39. The y-velocity results of the gauge point 39 are also not sufficient to compare the bulging performances of the interlayers. The y-velocities of the gauge point 39 are very similar.

In Figure 3.33c and Figure 3.33d, the velocity results of the gauge point 40 are pre-

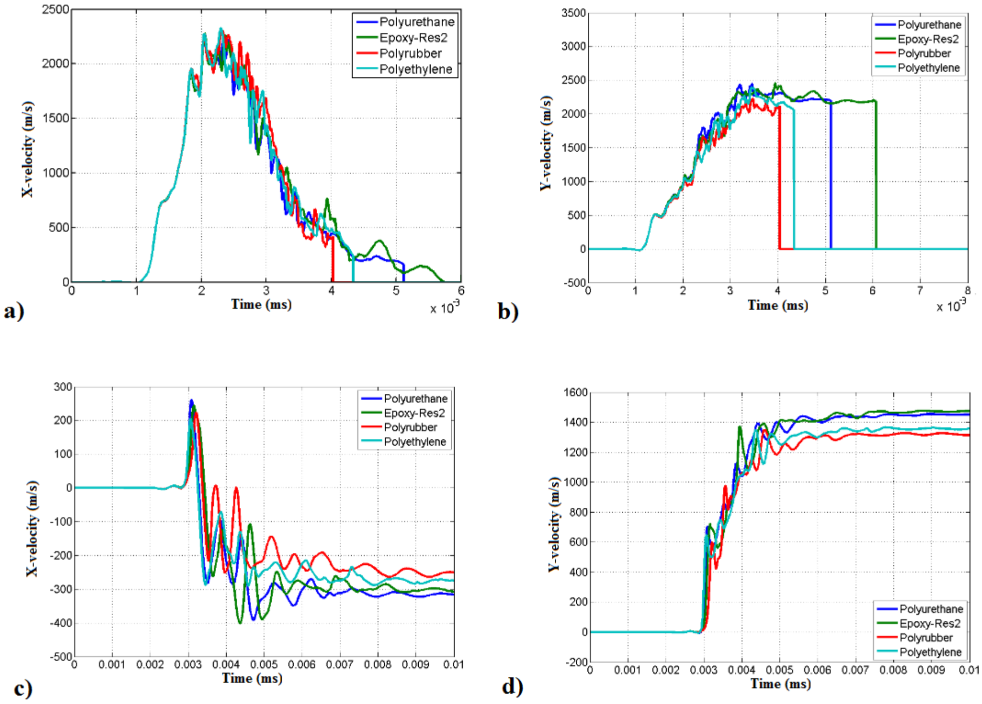

Figure 3.31: Velocity-time plots are given for gauge points on the BMP. Intermediate layers are polyurethane, epoxy-res2, poly-rubber and polyethylene. a) x-velocity of point 39, b) y-velocity of point 39, c) x-velocity of point 40 and d) y-velocity of point 40.

sented. In accordance with the interaction after 4.5 microseconds, the most and the least effective interlayers for the x-velocity of the BMP are neoprene and lucite, respectively. Similarly, in the y-direction, velocity values of the gauge point 40 are the highest for neoprene and the lowest for lucite.

From the results of Figure 3.28 - 3.33, it can be concluded that:

- According to the x-velocity values of the gauge point 37, the bulging performances of polycarbonate, epoxy-res2 and neoprene are the highest. The gauge point 37 gains high negative x-velocities due to bulging. On the other hand, in the y-direction, the performances of polycarbonate, polyethylene and epoxy-res2 are better than the others. The least effective materials in the x- and y-direction are adiprene, poly-rubber, plexiglass and epoxy-res.

- The x-velocity results of the gauge point 38 do not provide useful information about the effectiveness of the armor against the jet. However, in the y-direction, the bulging

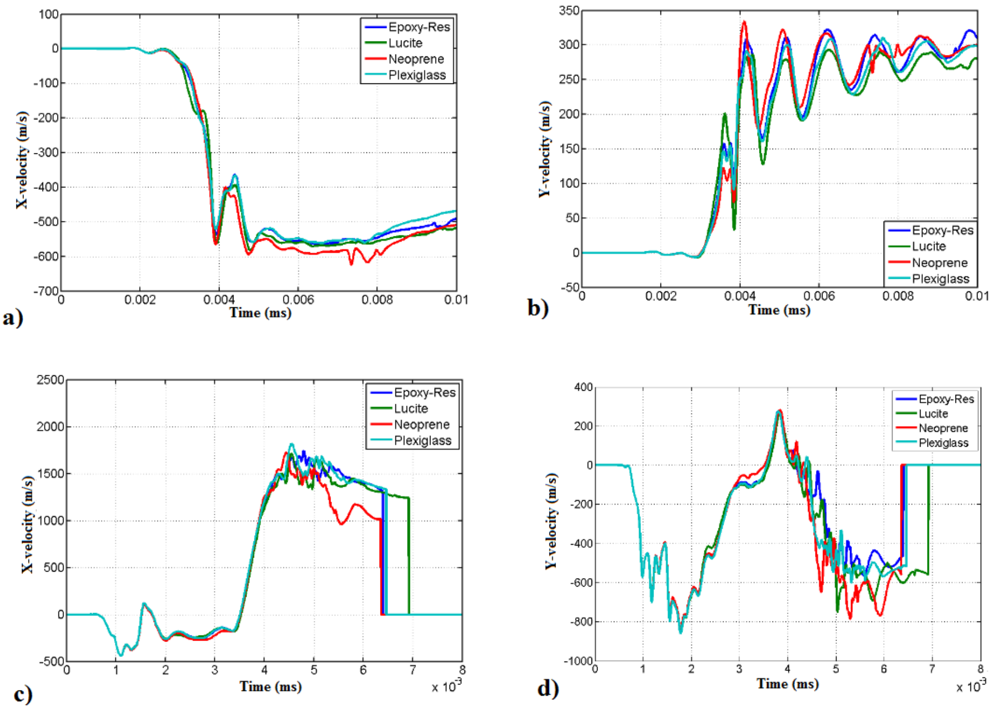

Figure 3.32: Velocity - time plots are given for gauge points on BMP. Intermediate layers are epoxy-res, lucite, neoprene and plexiglass. a) x-velocity of point 37, b) y-velocity of point 37, c) x-velocity of point 38 and d) y-velocity of point 38.

performances of polycarbonate, epoxy-res2, polyurethane and neoprene are better. The least effective interlayers are adiprene and poly-rubber.

- Similar to the x-velocity results of the gauge point 38, a reasonable comparison between the performances of the interlayers cannot be made with the x-velocity results of the gauge point 39. According to the y-velocity results of this gauge point, the highest bulging performance of the armor is achieved with epoxy-res2, polyurethane, phenoxy and polycarbonate.

-According to the x-velocity results of the gauge point 40, the bulging performances of epoxy-res2, polyurethane and neoprene seem to be the best. The y-velocity results of the gauge point 40 are shown in Figure3.29- d, Figure 3.31d and Figure 3.33 d. It can be seen that the performances of polyurethane, epoxy-res2, neoprene and plexiglass are better than the other interlayers.

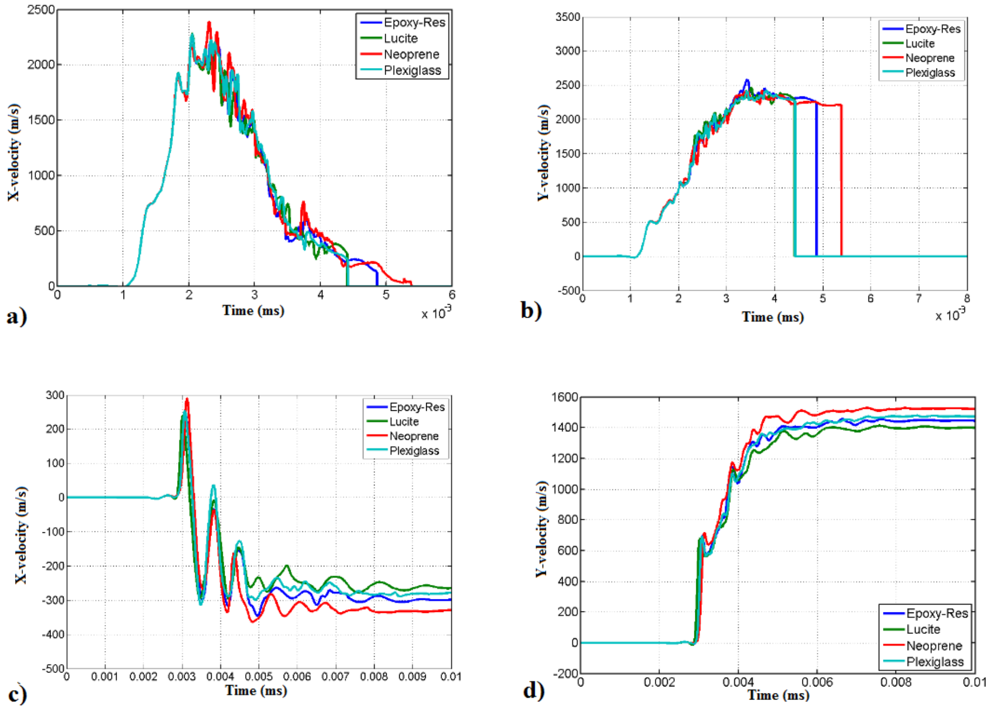

Figure 3.33: Velocity - time plots are given for gauge points on BMP. Intermediate layers are epoxy-res, lucite, neoprene and plexiglass. a) x-velocity of point 39, b) y-velocity of point 39, c) x-velocity of point 40 and d) y-velocity of point 40.

3.2.6 Velocity Results of Gauge Points on the FMP

To investigate the interaction between the jet and the bulging armor locally, gauge points are placed also on the FMP. The gauge points are 19, 20, 21 and 22. These gauge points can be seen in Figure 3.21. Velocity-time plots of the gauge points are given in Figure 3.34-3.39. In the plots, the x- and y-velocity of the gauge points are shown. In Figure 3.34 and Figure 3.35, interlayer materials are adiprene, nylon, phenoxy and polycarbonate. In Figure 3.36 and Figure 3.37, interlayer materials are polyurethane, epoxy-res2, poly-rubber and polyethylene. In Figure 3.38 and Figure 3.39, interlayer materials are epoxy-res, lucite, neoprene and plexiglass. For the FMP, it can be stated that x- and y-velocity of the gauge points are related to the bulging performance of the armor. Higher x-velocity in the positive x-direction and higher y-velocity in the positive or negative y-direction mean that the bulging performance of the armor is better.

Velocity results of the gauge point 19 are shown in Figure 3.34a and Figure 3.34b.

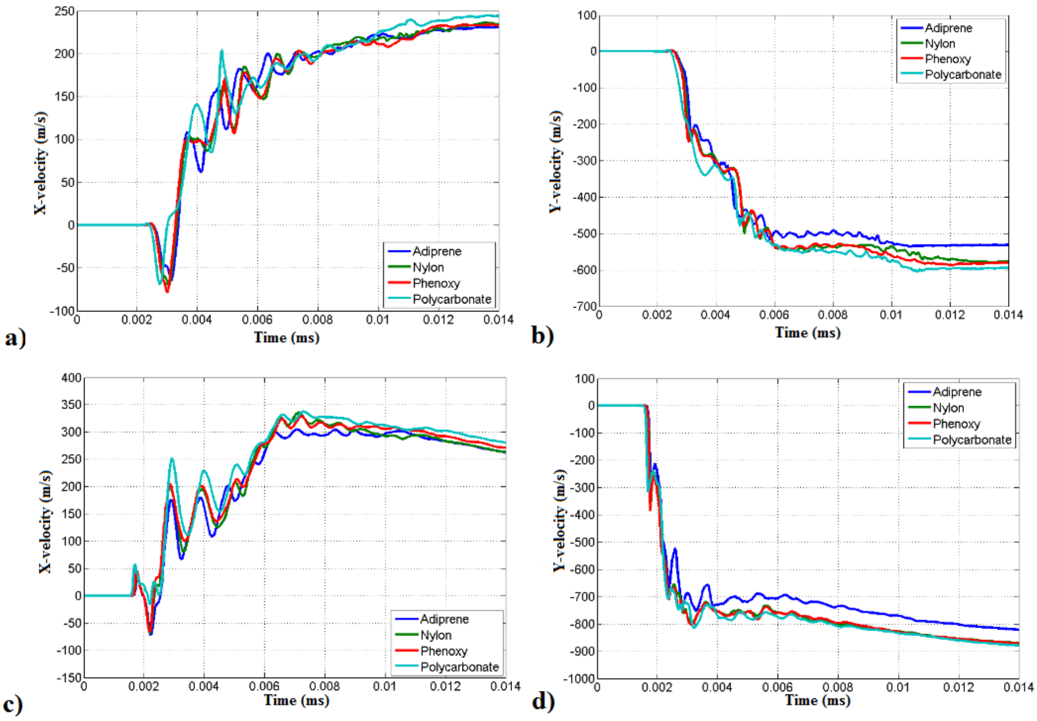

Figure 3.34: Velocity - time plots are given for gauge points on FMP. Intermediate layers are adiprene, nylon, phenoxy and polycarbonate. a) x-velocity of point 19, b) y-velocity of point 19, c) x-velocity of point 20 and d) y-velocity of point 20.

In Figure 3.34a, it can be seen that the highest and lowest x-velocity are values are obtained with polycarbonate and adiprene, respectively. The velocity differences for different interlayer materials especially occur after 10 microseconds. The x-velocity values of the gauge point 19 are moderate for nylon and phenoxy. In Figure 3.34b, similar to the results of the x-velocity of the gauge point 19, the highest and the lowest y-velocity values are obtained with polycarbonate and adiprene, respectively. While the gauge point 19 placed on polycarbonate has a velocity of up to -600 m/s, the gauge point 19 on adiprene are at about -530 m/s. As can be seen in this figure, the velocity differences for various interlayers approximately occurs after 5.8 microseconds.

The results of the x- and y-velocity of the gauge point 20 are shown in Figure 3.34c and Figure 3.34d. Like the results of the gauge point 19, polycarbonate is more effective in accelerating the FMP. The effectiveness of the armor decreases for other interlayer materials. The least effective interlayer against the jet is adiprene.

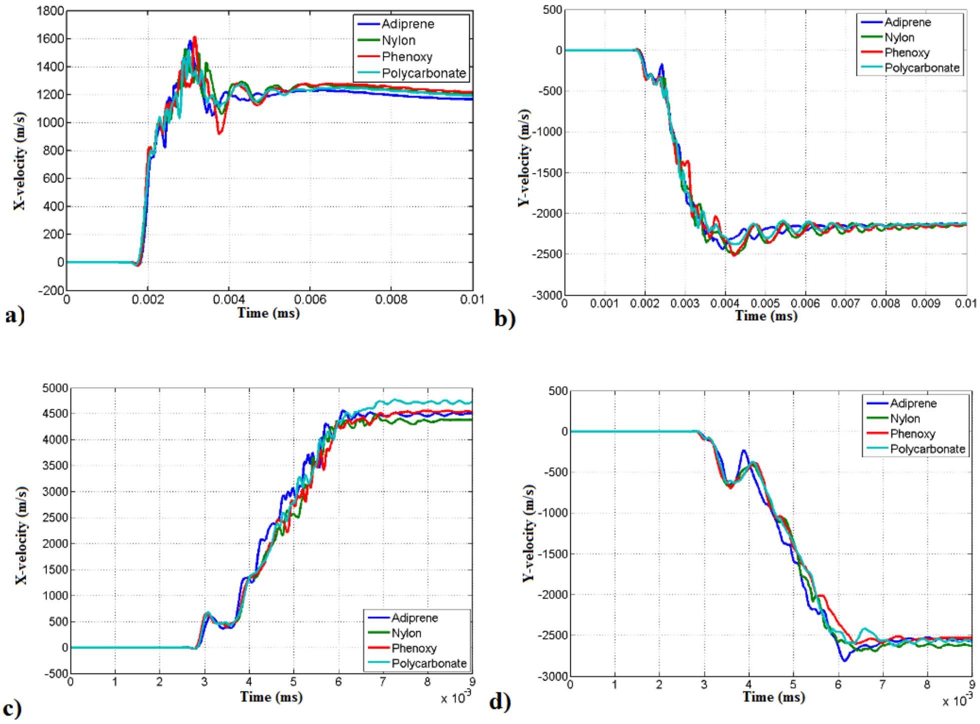

Figure 3.35: Velocity - time plots are given for gauge points on FMP. Intermediate layers are adiprene, nylon, phenoxy and polycarbonate. a) x-velocity of point 21, b) y-velocity of point 21, c) x-velocity of point 22 and d) y-velocity of point 22.

In Figure 3.35a and Figure 3.35b, changes of x- and y-velocity of the gauge point 21 are shown. As can be seen in Figure 3.35a, phenoxy and adiprene yield higher and lower x-velocity results for the gauge point 21, respectively. The difference in the x-velocity results appears after 5.5 microseconds. It can be seen in Figure 3.35b that the velocity differences in the y-direction are negligible.

The results of the velocity components of the gauge point 22 are shown in Figure 3.35c and Figure 3.35d. The x-velocity is the lowest for nylon and the highest for polycarbonate. The gauge x-velocity for nylon is approximately 4300 m/s after 6.2 microseconds. On the other hand, the gauge x-velocity for polycarbonate is approximately 4700 m/s. A comparison of y-velocity time histories for the interlayers does not lead to a conclusion. While the performance of adiprene is the best before 6.5 microseconds, the best performance is achieved with nylon after 6.5 microseconds.

The velocity results for the gauge point 19 are presented in Figure 3.36a and Figure 3.36b. As Figure 3.36a shows that the results for epoxy-res2, polyurethane and

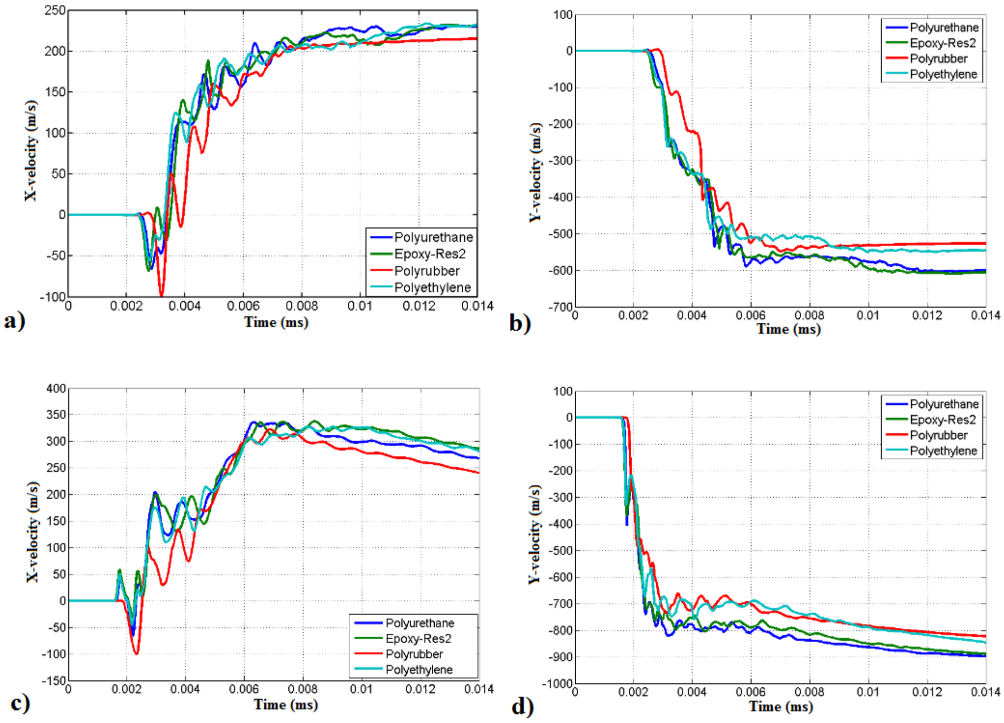

Figure 3.36: Velocity - time plots are given for gauge points on FMP. Intermediate layers are polyurethane, epoxy-res2, poly-rubber and polyethylene. a) x-velocity of point 19, b) y-velocity of point 19, c) x-velocity of point 20 and d) y-velocity of point 20.

polyethylene are similar to each other and the maximum velocities reach to same value at 14 microseconds. On the other hand, the lowest velocity in the x-direction is obtained for poly-rubber. In Figure 3.36b, it can be seen that the bulging performance based on the y-velocity of the gauge point is the highest for polyurethane and epoxy-res2.

The x- and y-velocity time histories for the gauge point 20 are given in Figure 3.36c and Figure 3.36d. According to the x-velocity results, the most effective interlayers are epoxy-res2 and polyethylene. Poly-rubber is the least effective interlayer. Epoxy-res2 and polyurethane lead to better performance of the armor when the y-velocity results are considered.

The results of the velocity components of the gauge point 21 are given in Figure 3.37a and Figure 3.37b. The x-velocity of the gauge point 21 is the smallest for poly-rubber after 3 ms. The x-velocity of the gauge point 21 for poly-rubber is approximately

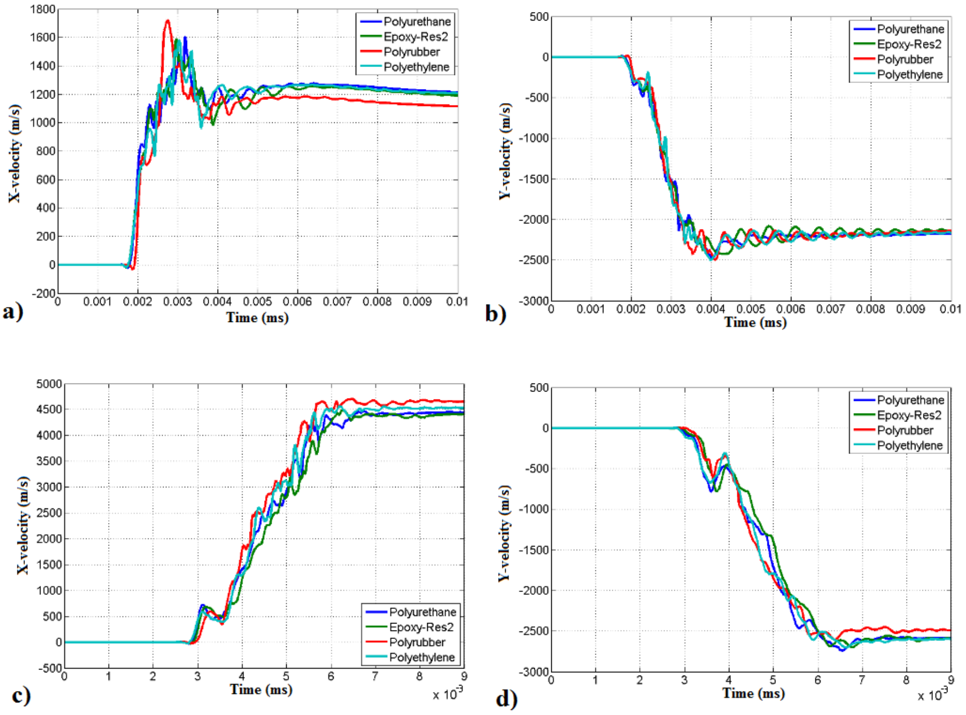

Figure 3.37: Velocity - time plots are given for gauge points on FMP. Intermediate layers are polyurethane, epoxy-res2, poly-rubber and polyethylene. a) x-velocity of point 21, b) y-velocity of point 21, c) x-velocity of point 22 and d) y-velocity of point 22.

1190 m/s at 6 microseconds. In addition, response time of poly-rubber in the aspect of shockwave reaction is at about 1.8 microseconds which is later than the others. The x-velocity of the gauge point 21 is similar for polyurethane, polyethylene and epoxy-res2. This velocity value approximately equals to 1250 m/s at 6 microseconds. On the other hand, Figure 3.37b indicates that there are no obvious differences in the y-velocity results of the gauge point 21.

In Figure 3.37c and Figure 3.37d, the changes of the x- and y-velocity of the gauge point 22 during the interaction of the jet with the armor are shown. As can be seen in Figure 3.37c, the highest velocity for the gauge point is accomplished by using poly-rubber as an interlayer. On the other hand, the lowest velocity of the gauge point 22 is accomplished via use of epoxy-res2 and polyurethane. According to the y-velocity results of the gauge point 22, poly-rubber is the least effective material. In addition, for the case of poly-rubber the gauge point starts to accelerate slightly later than the others.

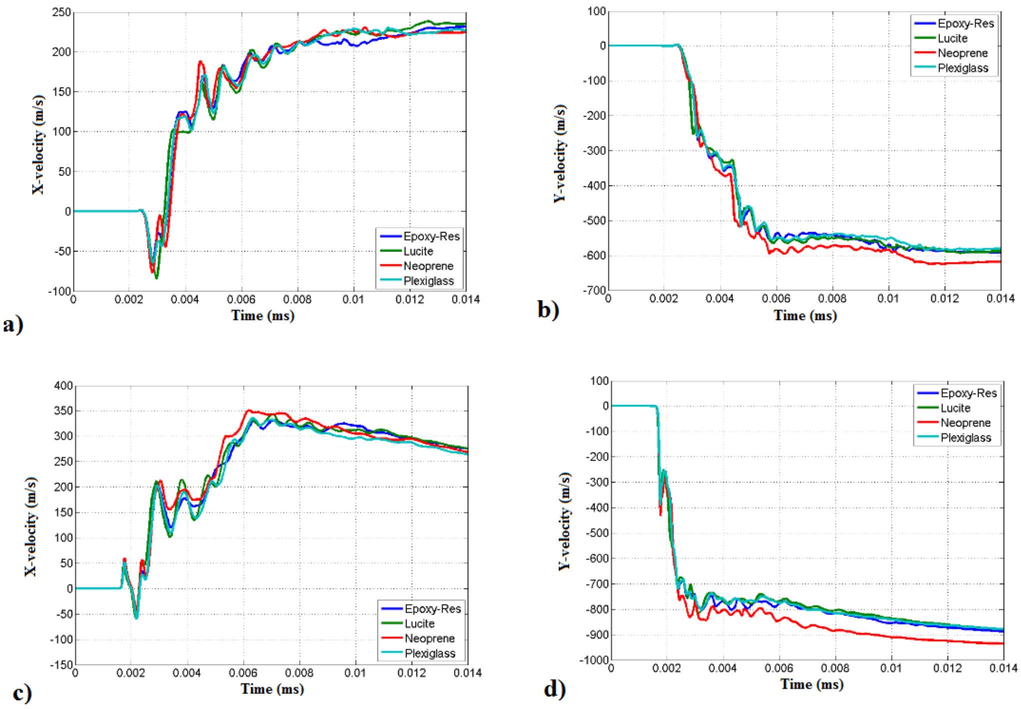

Figure 3.38: Velocity - time plots are given for gauge points on FMP. Intermediate layers are epoxy-res, lucite, neoprene and plexiglass. a) x-velocity of point 19, b) y-velocity of point 19, c) x-velocity of point 20 and d) y-velocity of point 20.

The x- and y-velocity of the gauge point 19 are plotted as shown in Figure 3.38a and Figure 3.38b. The greatest x-velocity of the gauge point is obtained with lucite while the responses are very similar for the other three materials. On the other hand, the maximum y-velocity is achieved for neoprene while the other materials lead to very close results. Velocity results for the gauge point 20 are presented in Figure 3.38c and Figure 3.38d. The x-velocity-time plot demonstrates that there are no significant differences among four interlayer materials. The y-velocity - time plot shows that the bulging performance of neoprene is significantly better than the others.

The x- and y-velocity of the gauge point 21 are plotted in Figure 3.39a and Figure 3.39b. It can be seen in Figure 3.39a that the performance of the armor against the jet is the lowest for neoprene. Velocity values of the other interlayers are similar. In the y-velocity - time plots, velocity values of all interlayers are nearly the same.

In Figure 3.39c and Figure 3.39d, results for the x- and y-velocity of the gauge point 22 are given. As Figure 3.39c shows the best performances are achieved with epoxy-

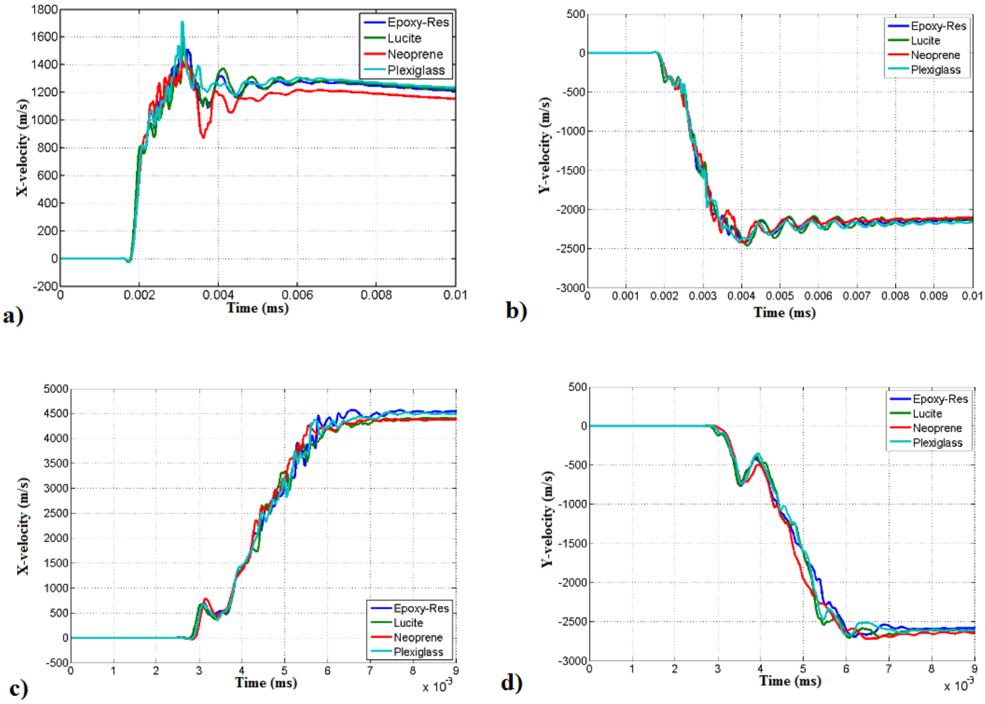

Figure 3.39: Velocity - time plots are given for gauge points on FMP. Intermediate layers are epoxy-res, lucite, neoprene and plexiglass. a) x-velocity of point 21, b) y-velocity of point 21, c) x-velocity of point 22 and d) y-velocity of point 22.

res and plexiglass. On the other hand, the performances of the interlayer in the y-direction cannot be evaluated by using the results in Figure 3.39d.

From the results of Figure 3.34-3.39, it can be concluded that:

- In the x-velocity - time plots of the gauge point 19, the most effective interlayer against the jet is polycarbonate. The x-velocity value for polycarbonate equals to about 240 m/s at 14 microseconds. According to the y-velocity results, epoxy-res2 is the most effective interlayer against the jet. The y-velocity value for epoxy-res2 equals to about -600 m/s at 10 microseconds. For both the x- and y-direction, the bulging performances of adiprene and polyrubber are the lowest when compared with the others.

- In the x-velocity - time plots of the gauge point 20, the most effective interlayer against the jet is epoxy-res2. Although the x-velocity value for polyethylene and epoxy-res2 equals to about 325 m/s at 10 microseconds, the x-velocity profile for the gauge point 20 is higher for epoxy-res2. On the other hand, the y-velocity of the gauge point 20 reaches peak values in the results of neoprene. The y-velocity value for neoprene equals to about -900 m/s at 10 microseconds. Similar to the results of gauge point 19, the least effective interlayers are adiprene, poly-rubber and polyethylene.

- Comparison of the performances of the interlayers in the aspect of y-velocity of the gauge point 21 is not possible. Similar velocity curves are obtained from the interlayers. On the other hand, the lowest velocity results are achieved with poly-rubber.

- As can be seen in Figure 3.35c, Figure 3.37c and Figure 3.39c, the performance of polycarbonate is prominent for the x-velocity of the gauge point 22. The x-velocity value for polycarbonate equals to about 4750 m/s at 9 microseconds. The y-velocity values for most of the interlayers except adiprene, phenoxy, polycarbonate and poly-rubber equal to about -2625 m/s at 9 microseconds. The performances of adiprene, phenoxy, polycarbonate and poly-rubber are the lowest.

In Figure 3.40, the process of the interaction between the jet and the NERA is shown for epoxy-res2. Interaction images are taken at 0.002 ms, 0.004 ms, 0.006 ms, 0.008 ms, 0.01 ms and 0.012 ms. Interaction processes for the other interlayers are similar and the performance of the interlayer materials cannot be determined from the images of the interaction. Therefore, the snapshots for other materials are not given.

Note that the mass within a highly distorted element can be retained with retained inertia option in the AUTODYN software. In this case, the mass of the eroded element is distributed to the nodes of this element. Conversation of inertia can be maintained, yet the two-dimensional solver in AUTODYN-2D does not allow retaining mass for planar symmetric models. However, the kinetic energy and momentum results within 0.015 ms are evaluated and the effect of mass loss is low in this time range.

In sum, many variables are investigated to determine the most effective interlayer material. These variables are the kinetic energy, x-momentum and y-momentum of the jet, the BMP and the FMP and velocity results of the gauge points on the jet, the BMP and the FMP. According to the many results in AUTODYN-2D, epoxy-res2 is found to be most effective interlayer due to its bulging performance. Therefore, epoxy-res2 is selected as an interlayer material. In the next chapter, it is used to model the NERA for the three-dimensional simulations.

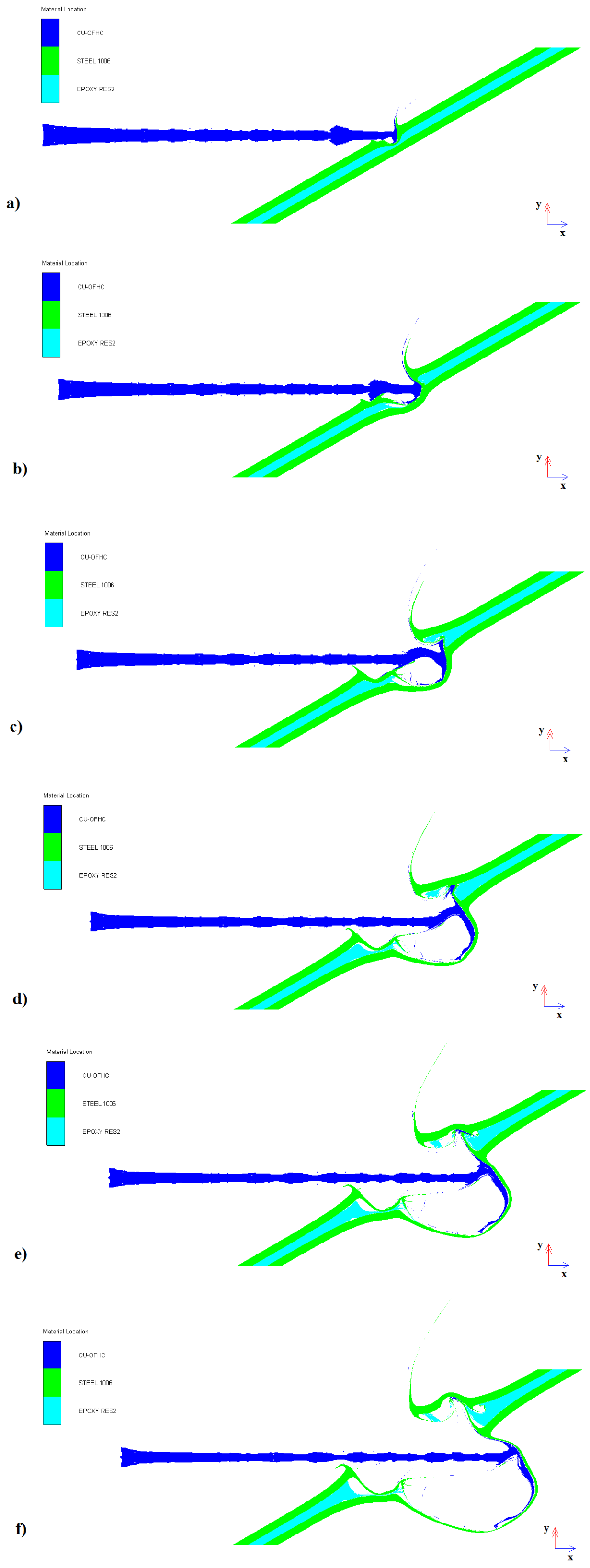

Figure 3.40: The interaction of the jet with the NERA is shown. Interlayer material is epoxy-res2. a) t= 0.002 ms, b) t= 0.004 ms, c) t= 0.006 ms, d) t= 0.008 ms, e) t= 0.01 ms and f) t= 0.012 ms

CHAPTER 4

THREE-DIMENSIONAL NUMERICAL ANALYSES AND MATERIAL OPTIMIZATION OF NERA

This chapter focuses on the investigation of significant parameters for the performance of NERA. The effects of density, C_1 and S_1 parameters defined in Chapter 2 equation 2.1 on the performance of NERA are investigated. To this end, density values are taken 1.086 g/cm^3, 1.186 g/cm^3 and 1.286 g/cm^3. As mentioned in Chapter 2, C_1 and S_1 are the shock parameters of a material. Three different values of C_1= $3.234 \cdot 10^3$ m/s, $4.234 \cdot 10^3$ m/s, $5.234 \cdot 10^3$ m/s are considered. In addition, analyses for S_1= 1.055, 1.255, 1.455 are conducted. To observe the performance of NERA comprehensively, gauge points are placed on the metal plates and the intermediate layers, see Figure 4.1. Pointwise velocity and pressure results are measured by the gauge points. In this chapter, the change of the pressure of the interlayers is measured by the gauge points 3, 4, 5, 7, 8 and 9. Furthermore, the changes of the x- and y-velocity of the FMP are measured by the gauge points 11 and 13. The gauge points placed on NERA can be seen in Figure 4.1.

In this chapter, all of the analyses are performed with the three-dimensional solver AUTODYN-3D so that the solution times of the analyses are longer than two-dimensional analyses.

The shaped charge model and the NERA are modelled symmetrically with respect to xy-plane. The actual dimension of each layer of the NERA is 100x100x3 mm. For the simulations, the dimension of each layer is taken 100x50x3 mm due to symmetry. The dimension of the NERA is given in Figure 4.2.

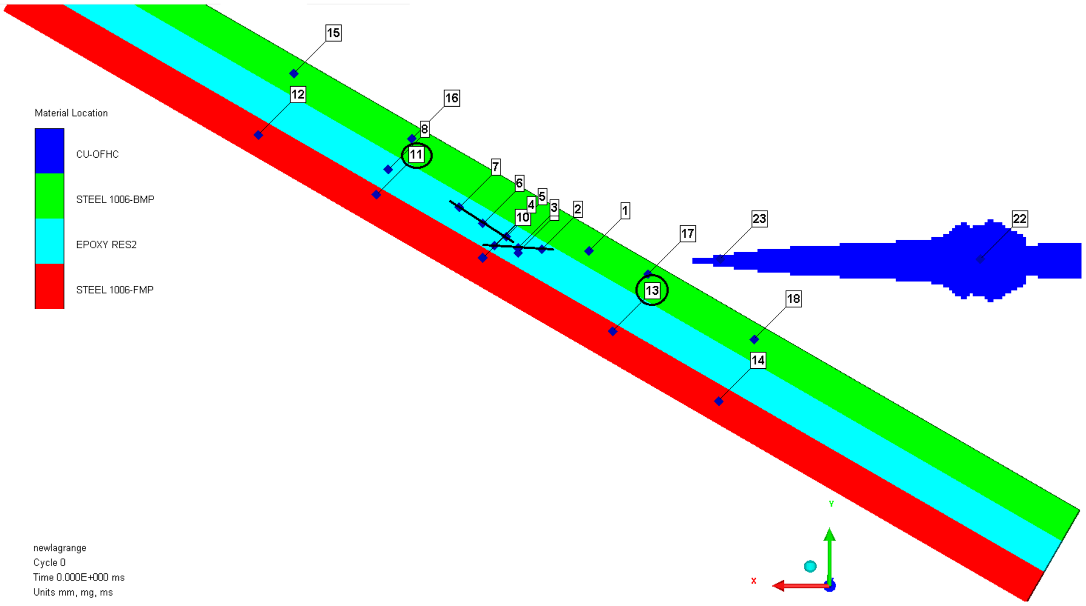

Figure 4.1: The gauge points on the intermediate layer, the BMP and the FMP

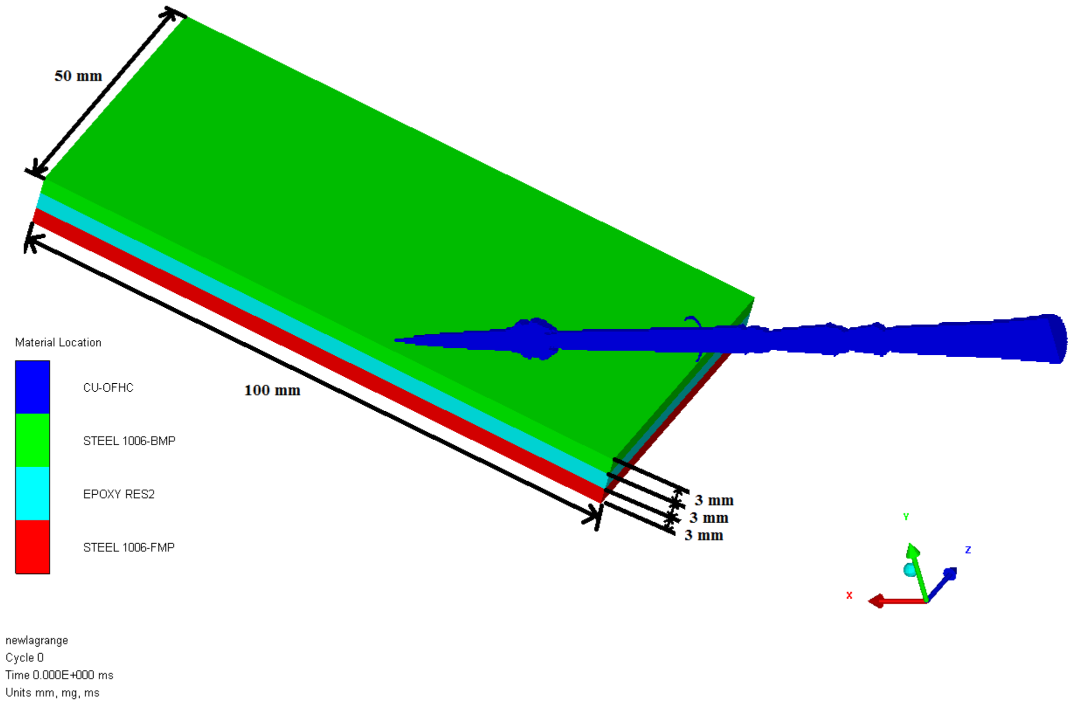

Figure 4.2: The dimensions of the intermediate layer, the BMP and the FMP

As mentioned in the previous chapter, jet formation analyses are conducted in the two-dimensional solver. Then, the formed jet is remapped from two-dimensional to three dimensional solver. This transferred jet is axisymmetric and the x-direction is selected as the jet flow direction.

In Chapter 3, epoxy-res2 was determined as the most effective interlayer material against the jet. Therefore, for the base model in three-dimensional analyses, epoxy-res2 is used as an interlayer material of the NERA. Similar to the previous chapter steel 1006 is selected as the material of the outer plates of the NERA. In Figure 4.3, the interactions between the jet and NERA are shown a different time instants.

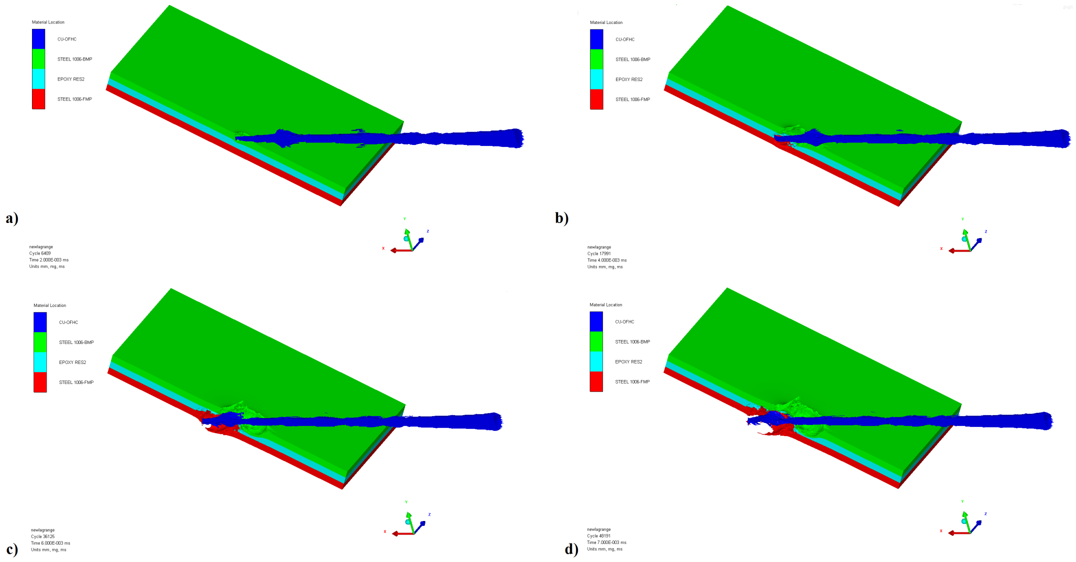

Figure 4.3: The interactions of the jet and the NERA at a) $t = 2\ \mu s$, b) $t = 4\ \mu s$, c) $t = 6\ \mu s$ and d) $t = 7\ \mu s$

The Lagrangian method is used to calculate the interaction of the jet with the armor. In impact and penetration analyses, Lagrangian methods mostly result in severe mesh distortions. This causes loss of accuracy and significant reduction in time increments used in solution. In this case, an erosion criterion of AUTODYN is used to erode highly distorted elements of the mesh.

4.1 Results of Density Variation

In this section, the density of the interlayer (epoxy-res2) is taken as a variable, while keeping the shock parameters (C_1 and S_1) constant. In other words, to observe the effect of the density on the performance of the NERA, the density is changed while keeping the the shock parameters of the interlayer as the original values of epoxy-res2. The original density value of epoxy-res2, in AUTODYN library, is 1.186 g/cm^3.

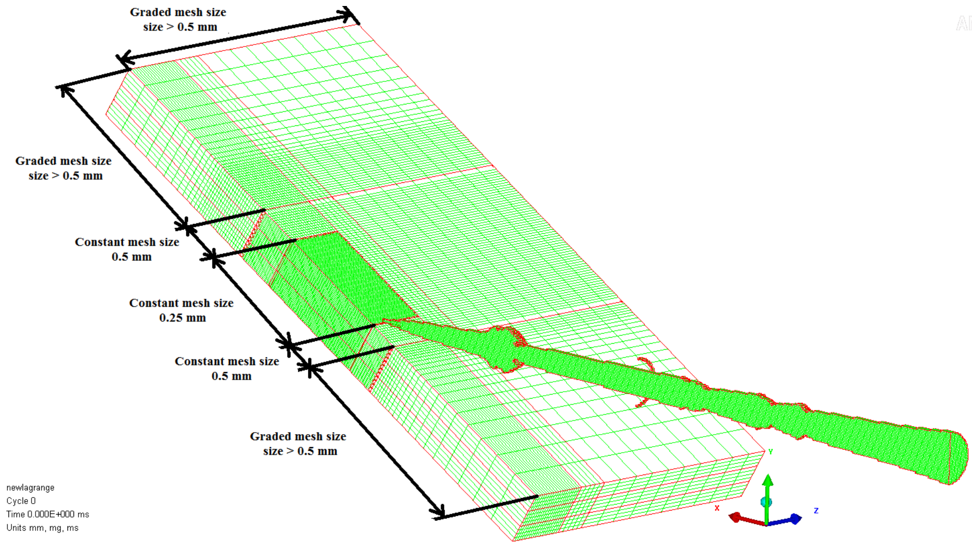

Figure 4.4: Mesh dimensions of the NERA

Besides its original density, 1.086 g/cm^3 and 1.286 g/cm^3 are used for simulations. Original C_1 and S_1 values of epoxy-res2, given in Table 3.1, are used for the interlayer.

4.1.1 Effects of Density on Momentum and Kinetic Energy Variation of the BMP

To evaluate the bulging performance of the NERA, momentum and kinetic energy results of the jet, the BMP and the FMP are examined. In Figure 4.5, changes of the x-momentum, y-momentum and kinetic energy of BMP are shown with respect to time. Three values of the density, 1.086 g/cm^3, 1.186 g/cm^3 and 1.286 g/cm^3, are considered in simulations. After the jet hits to the BMP, the x-momentum of BMP increases. Then, the x-momentum of the BMP decreases due to the bulging of the intermediate layer. This incident especially occurs after 5 ms. The x-momentum of the BMP does not decrease to negative values in three-dimensional analyses as in the case of two-dimensional analyses. This state can be seen in Figure 4.5a. This difference is due to two reasons. One of the reasons is that the three-dimensional solver in AUTODYN-3D allows retaining mass of an eroded element. As mentioned in Chapter 3, the mass of the eroded element cannot be distributed to the nodes of this element in AUTODYN-2D (for planar symmetric models). The other reason is that the masses of the plates in the three-dimensional model are higher than the masses in the two-dimensional model.The decrease of x-momentum of the BMP is more significant for higher densities of the interlayer material. It is concluded that density change of the interlayer affects the speed of the bulging process and the bulging rate of the intermediate layer. In Figure 4.5b, results for the y-momentum of the BMP is given. For the three density values of the intermediate layer, the BMP first gains very little negative y-momentum due to the jet impact. Then, BMP starts to gain positive y-momentum due to the bulging of the interlayer. The highest y-momentum results for the BMP are obtained with the interlayer having a density of 1.286 g/cm^3. In addition, the lowest y-momentum values of the BMP are obtained in the results of a density of 1.086 g/cm^3. From the y-momentum results, it can be concluded that the density of the interlayer is directly proportional to the y-momentum of the BMP. In Figure 4.5c, the results of kinetic energy change are given for the BMP. The kinetic energy values of the BMP are the highest for a density of 1.186 g/cm^3. The changing of the original density reduces the amount of kinetic energy. In other words, the kinetic energy of the BMP does not increase with increasing of the density. As can be seen in the results, the x-momentum values of the BMP is always positive and the change to negative values does not take place during the investigated time interval. Kinetic energy is proportional to the square of speed, so it depends on the absolute values of the velocity components. In the momentum equation, on the other hand the mass is multiplied with the velocity. Therefore, the changing of the density of the interlayer has different effects on the kinetic energy and the momentum of the BMP. It can be concluded from the BMP plots in Figure 4.5 that the increase of the density of interlayer increases the performance of the armor.

4.1.2 Effects of Density on Momentum and Kinetic Energy Variation of The FMP

Figure 4.6 shows the x-momentum - time, the y-momentum - time and the kinetic energy-time histories of the FMP. The jet first hits the BMP so the momentums of the BMP begin to increase at about 0.8 ms. On the other hand, the x- and y-momentum of FMP increase after 2 microseconds. As Figure 4.6a and Figure 4.6b show, the momentums of the FMP are directly affected by the density of the interlayer. Figure 4.6c shows a time plot of the kinetic energy of the FMP. Similar to the the momentum

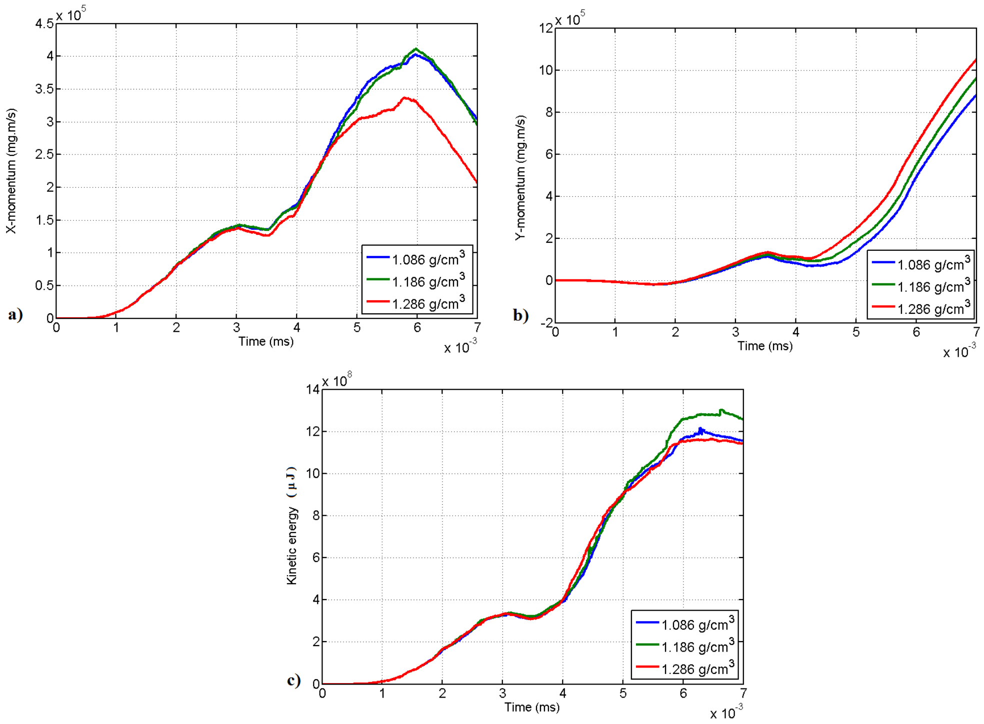

Figure 4.5: Results of BMP are given with respect to density variation of the interlayer material. a) x-momentum - time, b) y-momentum - time and c) kinetic energy - time

results for the FMP, the kinetic energy also increases with an increase in the original density value. As can be seen in the results, the effect of density change on the BMP is more significant than the effect on the FMP. According to the momentum and kinetic energy results of the FMP, it is concluded that increasing the density of the intermediate layer improves the bulging performance of the armor.

4.1.3 Effects of Density on Momentum and Kinetic Energy Variation of The Jet

In Figure 4.7, the x-momentum - time, the y-momentum - time and the kinetic energy-time histories of the jet are presented. In compliance with the momentum results, greater lost in x-momentum and greater gain in y-momentum are obtained in the results of the density of 1.286 g/cm^3. In addition, the highest values of kinetic energy loss for the jet occur in the results of the density of 1.286 g/cm^3. As a result, the interlayer having higher density can contribute to the performance of the NERA.

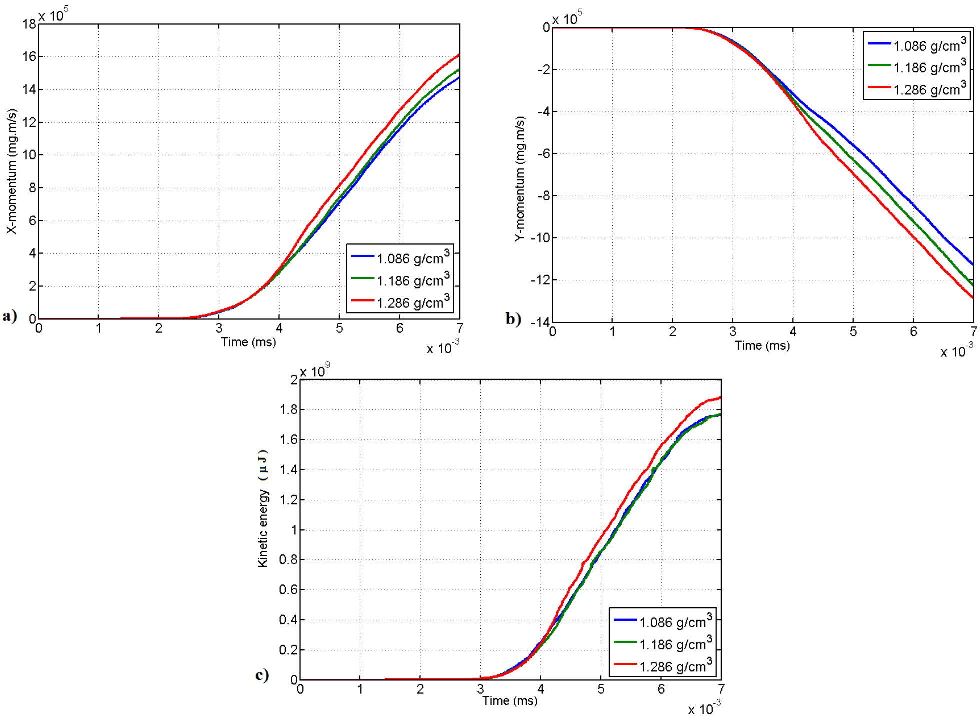

Figure 4.6: Results of FMP are given with respect to density variation of the interlayer material. a) x-momentum - time, b) y-momentum - time and c) kinetic energy - time

4.1.4 Effects of Density on Pressure and Velocity Variation of Gauge Points

In Figure 4.8 and Figure 4.9, changes of pressure at gauge point 2, 3, 4, 5, 6 and 7 with respect to time are shown. Gauge point 2, 3 and 4 are located in the jet flow direction. As shown in Figure 4.1, these gauge points are located on the interlayer. They are moving gauges so that they move together with the mesh. The gauges recording pressure are affected by highly distorted elements of the intermediate layer. During the analysis, the gauge points and degenerated elements can be eroded at the same time. It could be seen in Figure 4.8a, Figure 4.8b and Figure 4.8c that the gauge point 2, 3 and 4 are eroded at about 3.3 microseconds, 3.7 microseconds and 4.1 microseconds, respectively. The gauge point 2 is closer to the jet impact region than the gauge point 4, so the gauge point 2 is eroded before. Similarly, the gauge point 5, 6 and 7, placed on the intermediate layer, are eroded with respect to distance from the jet impact region. In Figure 4.9a, Figure 4.9b and Figure 4.9c, it can be seen that the gauge point 5 is eroded earlier than the gauge points 6 and 7. It can be concluded from Figure 4.8 and Figure 4.9 that increasing the original density causes higher pressure on the most of the gauge points, especially in the early times of the interaction. This conclusion does not hold for the gauge points 2 and 3. Pressures at the gauge points 2 and 3 reach their highest values when the density of the interlayer is 1.186 g/cm^3. However, it can be seen in the figures that these gauge points are eroded suddenly after the pressure reaches its maximum value. For this reason, the comparison of the pressure results of the two gauge points may be misleading. On the other hand, pressures at the other four gauge points first reach to their maximum value, and after some time drop to zero due to erosion.

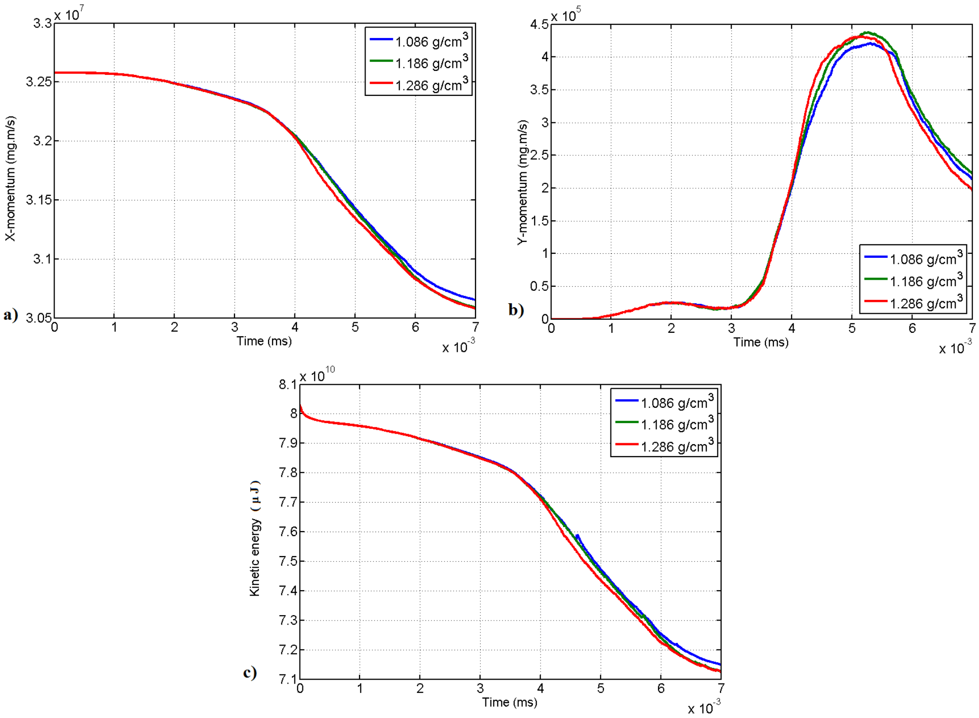

Figure 4.7: Results of the jet are given with respect to density variation of the interlayer material. a) x-momentum - time, b) y-momentum - time and c) kinetic energy - time

Velocity changes of the gauge points 11 and 13 on FMP are shown in Figure 4.10 and Figure 4.11. Note that the gauge point 11 is located above the direction of the jet flow while the gauge point 13 is located below the direction of the jet flow. For a better performance of the NERA, these gauge points should gain higher positive x-velocity. Furthermore, the gauge point 13 should be accelerated in the negative y-direction, while the gauge point 11 should be accelerated in positive y-direction. From the velocity-time plots of the gauge points on FMP, it is concluded that increasing density of the intermediate layer enhances the bulging performance of the NERA.

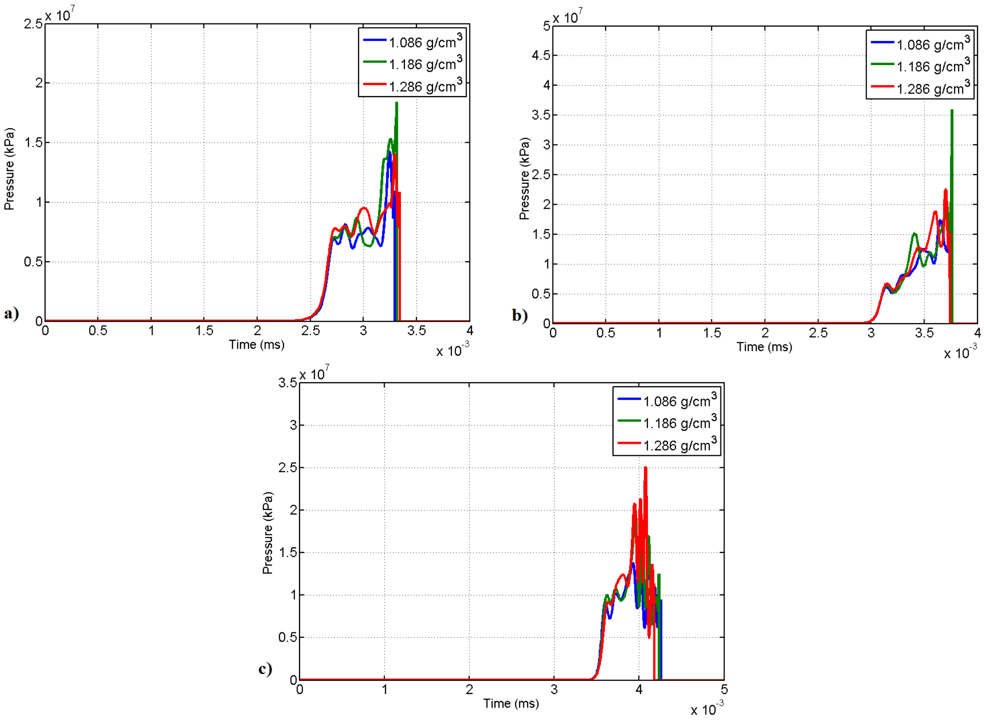

Figure 4.8: Pressure results of gauge points are given with respect to density variation of the interlayer material. a) pressure at gauge point 2 - time, b) pressure at gauge point 3 - time and c) pressure at gauge point 4 - time

4.2 Results of C_1 Variation

In this section, the shock parameter C_1 of the interlayer (epoxy-res2) is taken as a variable. The density and S_1 are taken as constant. In other words, to observe the effect of C_1 on the performance of the NERA, C_1 is changed while keeping the the density and S_1 of the interlayer constant. The original C_1 parameter of epoxy-res2 equals to $3.234 \cdot 10^3$ m/s in AUTODYN library. In addition to its original C_1 value, $4.234 \cdot 10^3$ m/s and $5.234 \cdot 10^3$ m/s are used for the analyses. The original density and S_1 values of epoxy-res2, given in Table 4.1, are used for the interlayer. In accordance with Table 3.1, C_1 value of epoxy-res2 is the highest when compared with the others. Therefore, the original C_1 value is only increased to investigate the effect of C_1.

Table 4.1: Mechanical properties of the interlayer material

Interlayer Material	ρ [g/cm^3]	C_1 [m/s]	S_1 [-]
Epoxy Res2	1.186	$3.234 \cdot 10^3$	1.255

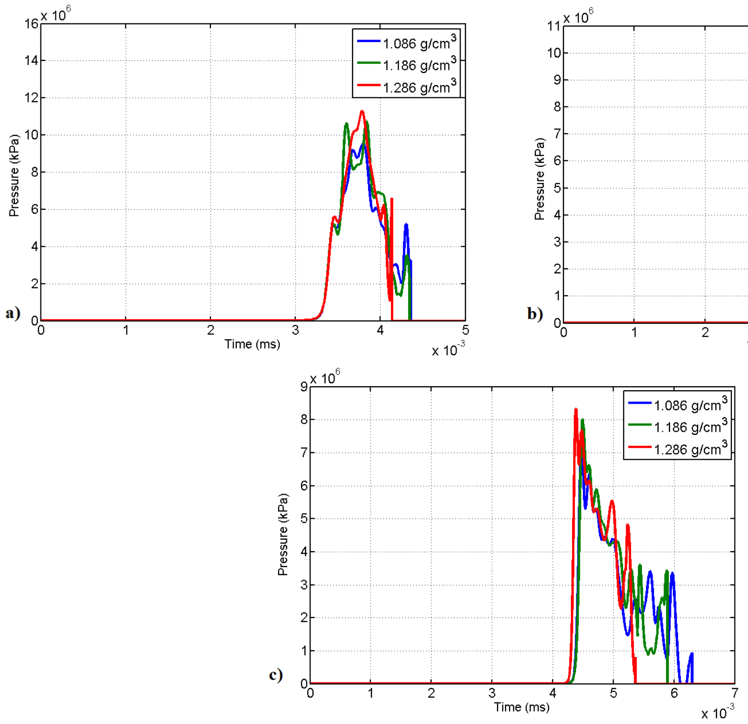

Figure 4.9: Pressure results of gauge points are given with respect to density variation of the interlayer material. a) pressure at gauge point 5 - time, b) pressure at gauge point 6 - time and c) pressure at gauge point 7 - time

4.2.1 Effects of C_1 on Momentum and Kinetic Energy Variation of the BMP

In Figure 4.12, the x-momentum - time, the y-momentum - time and the kinetic energy-time histories of the jet are presented. As mentioned before, while the density and S_1 parameter are taken constant, C_1 parameter of the interlayer is varied. After the jet hits the BMP, the x-momentum of the BMP increases till the bulging of the interlayer. Bulging process causes the x-momentum of the BMP to decrease. The response time of the interlayer to bulge and cause the BMP to loose x-momentum depends directly on C_1 parameter. According to the results given in Figure 4.12, the x-momentum of the BMP decreases with increasing C_1 value. Therefore, higher C_1 values increase the amount of bulging and the performance of the armor. In Figure 4.12b, the y-momentum - time history of the BMP is given. Thus, similar to the x-momentum results, the performance of the armor is better for C_1 value of $5.234 \cdot 10^3$ m/s. In Figure 4.12c, the change of the kinetic energy of the BMP with time is shown. The kinetic energy changes are very similar for three C_1 values. In conclusion, it can be inferred that the increase of C_1 value of the interlayer material

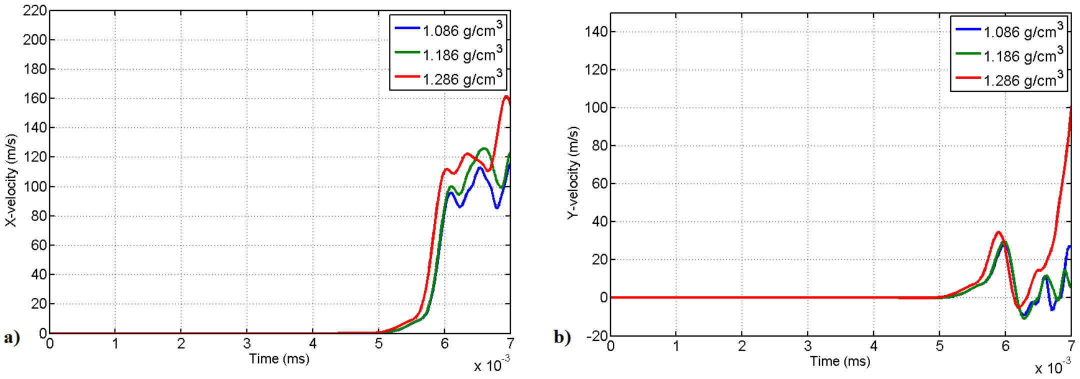

Figure 4.10: Velocity results of gauge point 11 are given with respect to density variation of the interlayer material. a) x-velocity - time and b) y-velocity - time

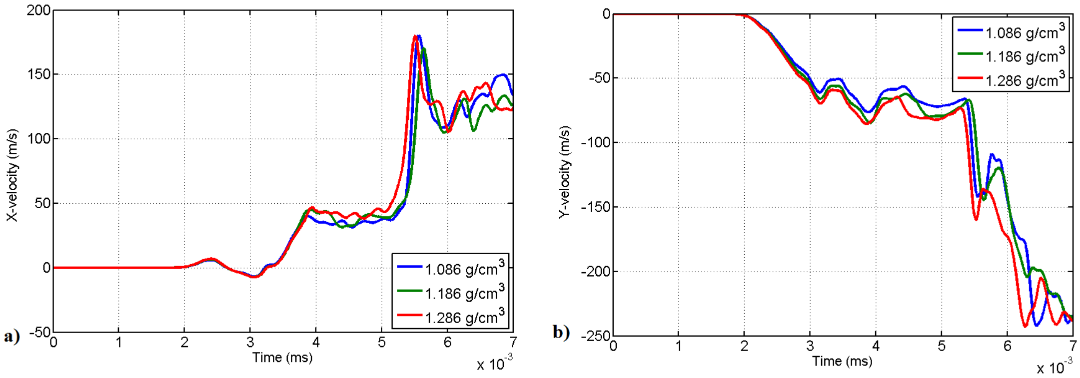

Figure 4.11: Velocity results of gauge point 13 are given with respect to density variation of the interlayer material. a) x-velocity - time and b) y-velocity - time

improves the bulging performance of the armor.

4.2.2 Effects of C_1 on Momentum and Kinetic Energy Variation of the FMP

In Figure 4.13, the changes of the x-momentum, the y-momentum and the kinetic energy of the FMP with respect to time are shown. After the jet hits the BMP, this plate starts to gain x-momentum at 0.8 ms as already shown in Figure 4.12a. On the other hand, the FMP gains x-momentum after 2 ms. As can be seen in Figure 4.13a and Figure 4.13b, increase of C_1 causes a higher positive x- and the negative y-momentum of the FMP. Therefore, higher C_1 values give rise to improved performance of the armor. The kinetic energy-time history of the FMP is presented in Figure 4.13c showing no

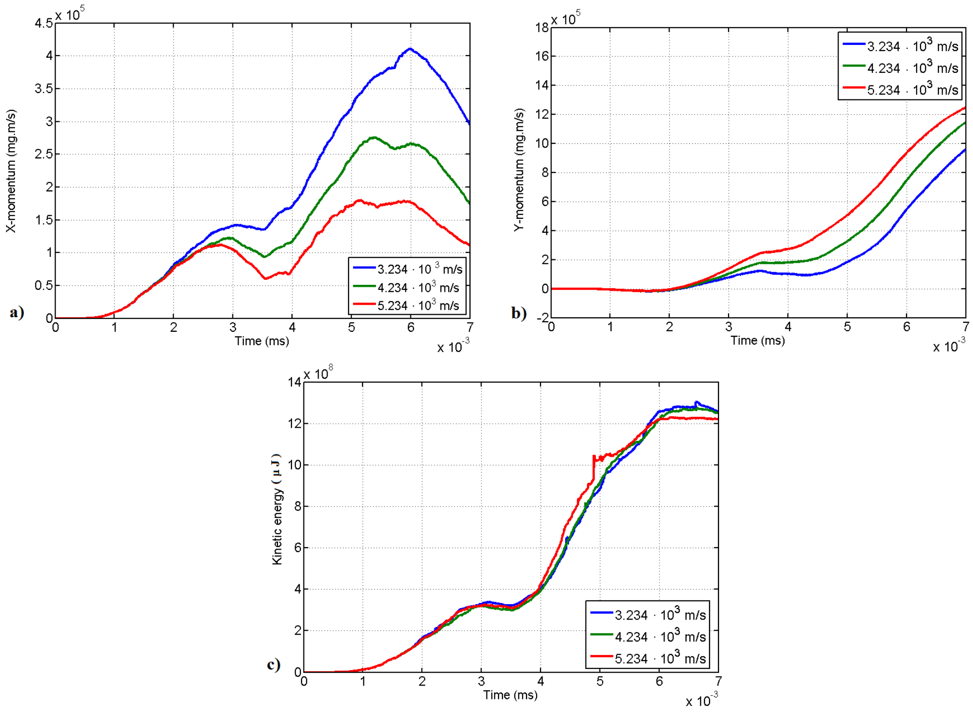

Figure 4.12: Results of BMP are given with respect to C_1 variation of the interlayer material. a) x-momentum - time, b) y-momentum - time and c) kinetic energy - time

significant change with the parameter C_1. The effect of change of C_1 parameter is more on BMP than FMP. In conclusion, increase of C_1 parameter contributes to the performance of the NERA.

4.2.3 Effects of C_1 on Momentum and Kinetic Energy Variation of the Jet

The effects of change of C_1 parameter on the x-momentum, the y-momentum and the kinetic energy of the jet are given in Figure 4.14. According to this figure, the change of C_1 parameter does not make significant differences in the momentum and kinetic energy results of the jet.

4.2.4 Effects of C_1 on Pressure and Velocity Variation of Gauge Points

In Figure 4.15 and Figure 4.16, pressure changes at the gauge point 2, 3, 4, 5, 6 and 7 on the intermediate layer are given. The gauge points 2, 3 and 4 are located in the flow direction of the jet. The elements, in the interaction region between the jet and

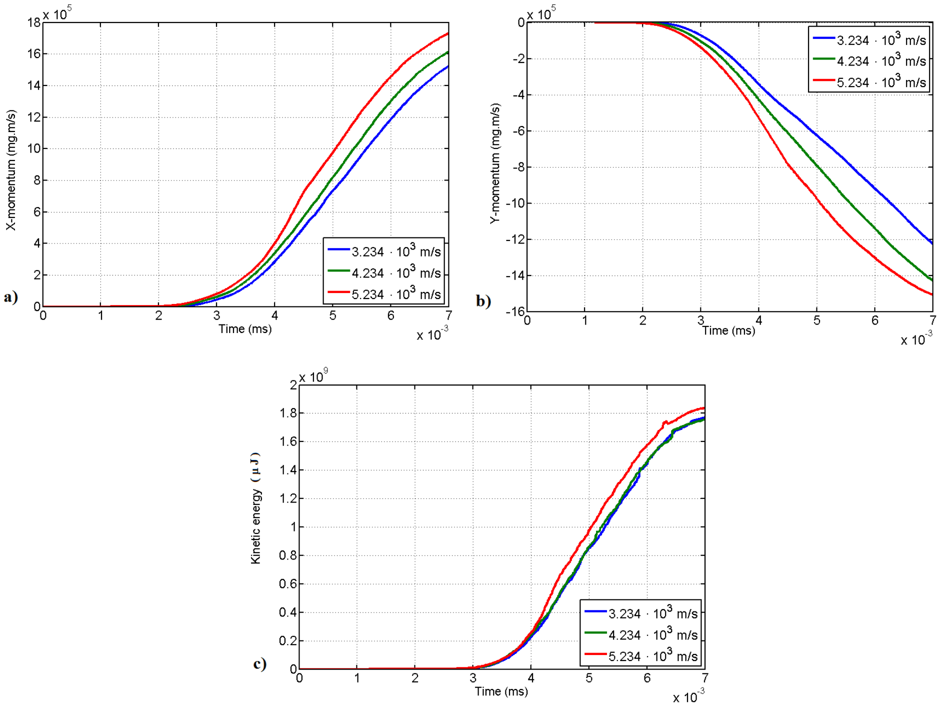

Figure 4.13: Results of FMP are given with respect to C_1 variation of the interlayer material. a) x-momentum - time, b) y-momentum - time and c) kinetic energy - time

the NERA, can be highly distorted during the simulations. To this end, the gauge points and distorted elements can be eroded. In the pressure plots, pressure values drop to zero suddenly due to the element erosion. It can be seen in Figure 4.15a, Figure 4.15b and Figure 4.15c that the gauge points 2, 3 and 4 are eroded at about 3.3 microseconds, 3.8 microseconds and 4.1 microseconds (3.8 microseconds for C_1= 4.234 m/s), respectively. The gauge points 5, 6 and 7, placed parallel to the long side of the interlayer. Corresponding pressure-time plots for these gauge points can be seen in Figure 4.16d, Figure 4.16e and Figure 4.16c. It is seen from Figure 4.15 and Figure 4.16 that the maximum pressure generally decreases with increase in C_1. This inference is not valid for Figure 4.15c and Figure 4.16f. Furthermore, as expected, the increase in C_1 parameter results in an earlier generation of pressure at the gauge points. This means that pressure wave moves faster through the interlayer. Therefore, bulging of an armor occurs quicker due to the earlier generation of pressure. This condition improves the performance of the armor.

Velocity-time histories of the gauge points 11 and 13, on the FMP, are given in Figure 4.17 and Figure 4.18. Higher gauge velocities are related with the performance

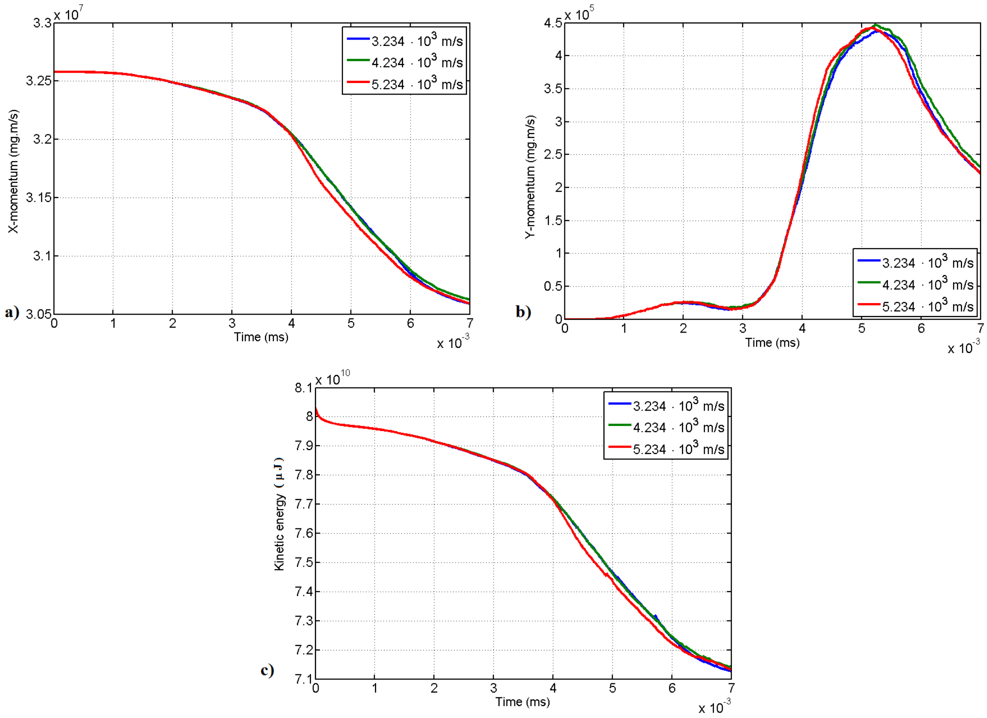

Figure 4.14: Results of the jet are given with respect to C_1 variation of the interlayer material. a) x-momentum - time, b) y-momentum - time and c) kinetic energy - time

of bulging.There is no clear correlation between C_1 value and the gauge velocities. However, it is clearly seen that the gauge points start to accelerate earlier if the C_1 value is larger. It is therefore concluded from Figure 4.15-4.18 that the increase in C_1 parameter improves the bulging performance of the armor.

4.3 Results of S_1 Variation

In this section, S_1 parameter of the interlayer (epoxy-res2) is taken as a variable. The density and C_1 parameter are taken as constant. In other words, to observe the effect of S_1 parameter on the performance of the NERA, S_1 parameter is changed while keeping the density and C_1 parameter of the interlayer constant. The original S_1 parameter of epoxy-res2 is 1.255. The original material properties of epoxy-res2, in AUTODYN library, are given in Table 4.1. Besides its original S_1 value, 1.055 and 1.455 are used for the simulations. Moreover, the effects of S_1 parameter on bulging of the BMP, the FMP and the jet are also investigated through pressure-time and velocity-time histories of the gauge points.

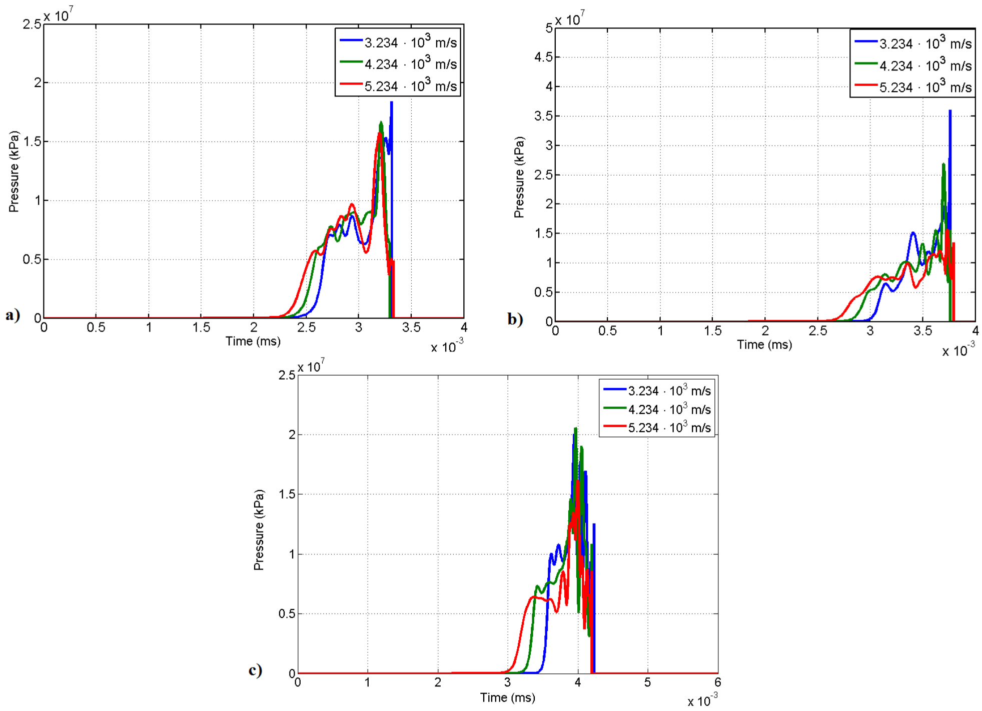

Figure 4.15: Pressure results of gauge points are given with respect to C_1 variation of the interlayer material. a) pressure at gauge point 2, b) pressure at gauge point 3 and c) pressure at gauge point 4

4.3.1 Effects of S_1 on Momentum and Kinetic Energy Variation of the BMP

In Figure 4.19, the results of the x-momentum, the y-momentum and the kinetic energy of the BMP are shown for S_1 values. As can be seen in Figure 4.19-a, the x-momentum of the BMP increases due to the hit of the jet till 3 ms. After about 6 microseconds, the x-momentum of the BMP starts to decrease due to bulging. When S_1 equals to 1.455, the decrease in the x-momentum of the BMP is the largest. The y-momentum - time history of the BMP is presented in Figure 4.19b. In compliance with the results of three S_1 values, the BMP first gains little y-momentum in the negative y-direction and then moves in the positive y-direction due to the bulging of the armor. The highest y-momentum is observed for S_1 value of 1.455. In addition, there is no significant difference in the results of the other two S_1 values. The kinetic energy results of S_1= 1.055 and S_1= 1.455 are approximately the same. On the other hand, the highest kinetic energy for the BMP is achieved with the interlayer having S_1= 1.255. This can be seen in the figure after 6 microseconds. According to these results, it can be stated that an interlayer having higher S_1 value improves the bulging

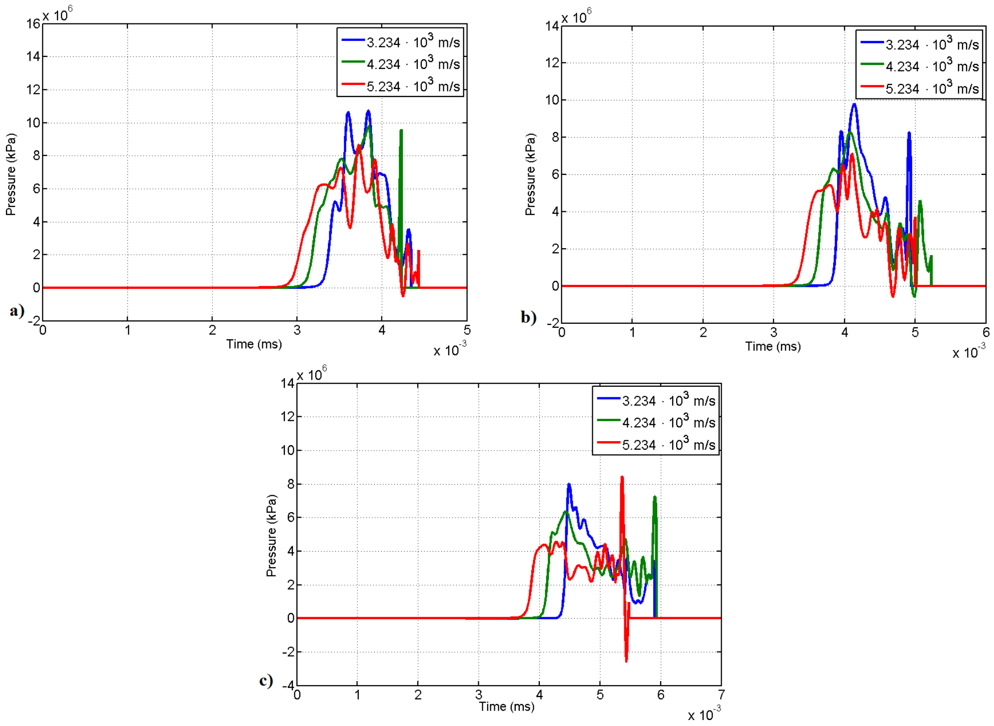

Figure 4.16: Pressure results of gauge points are given with respect to C_1 variation of the interlayer material. a) pressure at gauge point 5, b) pressure at gauge point 6 and c) pressure at gauge point 7

performance of the NERA.

4.3.2 Effects of S_1 on Momentum and Kinetic Energy Variation of the FMP

In Figure 4.20, the x-momentum - time, the y-momentum - time and the kinetic energy-time plots of the FMP are presented. As mentioned before, S_1 parameter of the interlayer is taken to be variable. The jet first hits the BMP causing the BMP to gain momentum after 0.8 microseconds. On the other hand, the FMP starts to gain momentum after t= 2.5 ms. As can be seen in Figure 4.20a and Figure 4.20b, the change of S_1 parameter does not significantly change the momentum results of the FMP. However, the momentum results for S_1 = 1.455 are a little higher than the others. In addition, there is a small difference in the kinetic energy results of the FMP. As Figure 4.20c shows, the kinetic energy results for S_1= 1.455 are a little higher than the others. According to these results, higher values of S_1 parameter of the interlayer seem to improve the bulging performance, but the changes in the results for different values of S_1 are marginal. The different values of S_1 have no obvious effect on the

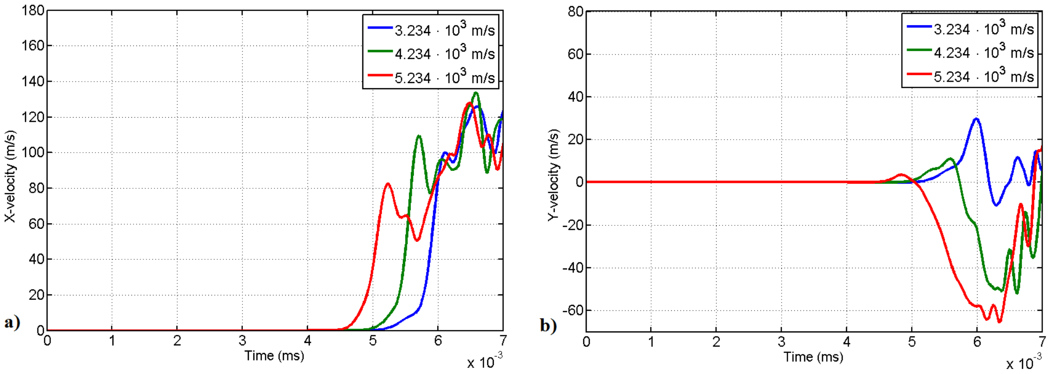

Figure 4.17: Velocity results of gauge point 11 are given with respect to C_1 variation of the interlayer material. a) x-velocity - time and b) y-velocity - time

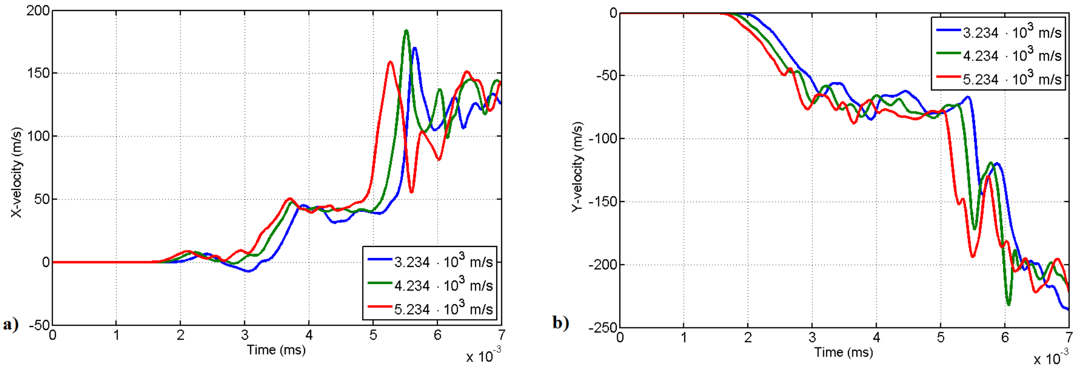

Figure 4.18: Velocity results of gauge point 13 are given with respect to C_1 variation of the interlayer material. a) x-velocity - time and b) y-velocity - time

momentums and kinetic energy of the FMP.

4.3.3 Effects of S_1 on Momentum and Kinetic Energy Variation of the Jet

Effects of change of S_1 parameter on the momentums and kinetic energy of the jet are shown in Figure 4.21. The x-momentum and the kinetic energy of the jet are not affected by the change of S_1 parameter. These results can be seen in Figure 4.21a and Figure 4.21c. In Figure 4.21b, it is shown that the lowest values for the y-momentum of the jet are obtained from the result of the interlayer having a S_1 of 1.455. Therefore, a lower S_1 value leads to higher y-momentum of the jet. In conclusion, it can be stated that the lower S_1 value contributes the bulging performance of the NERA.

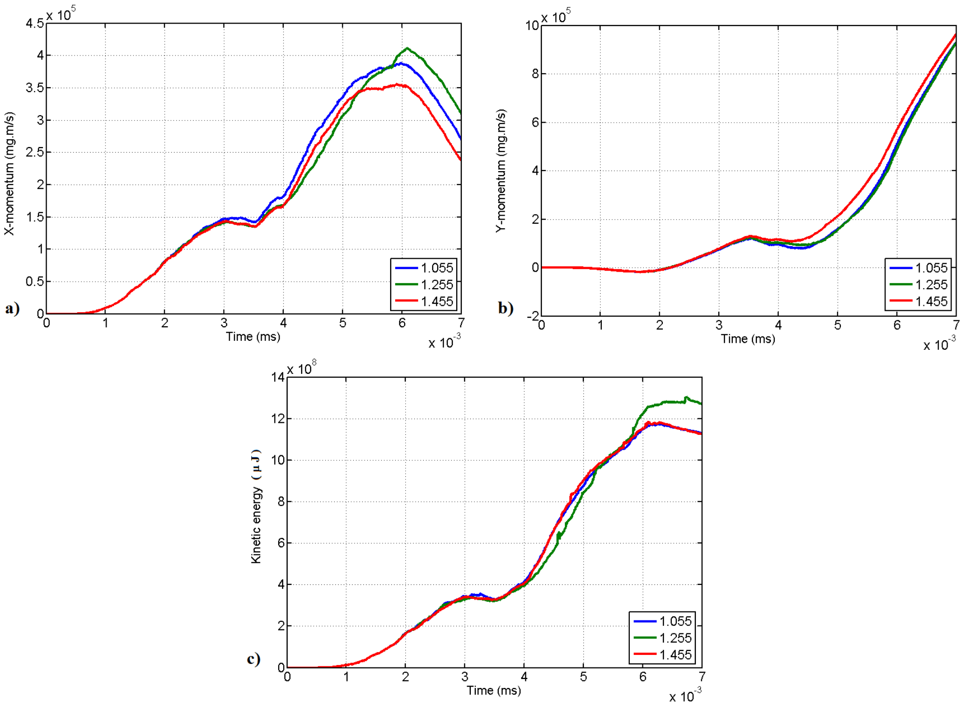

Figure 4.19: Results of BMP are given with respect to S_1 variation of the interlayer material. a) x-momentum - time, b) y-momentum - time and c) kinetic energy - time

4.3.4 Effects of S_1 on Pressure and Velocity Variation of Gauge Points

In Figure 4.22 and Figure 4.23, pressure changes at the gauge point 2, 3, 4, 5, 6 and 7 are given for three S_1 values. As Figure 4.1 shows, the gauge point 2, 3 and 4 are positioned parallel to the flow direction of the jet. When the jet penetrates into the armor, elements in the interaction region are deformed significantly. In this case, the elements in which the strain values exceed a given value are eroded. Both the elements and the gauge points 2, 3 and 4 are eroded at the same time. It can be seen in the pressure plots that pressure values drop to zero instantaneously due to this erosion. In Figure 4.22, removal of the gauge points 2, 3 and 4 can be seen. According to the results in Figure 4.22, the peak pressure value of the interlayer having S_1= 1.055 is a little lower than the pressures of the other S_1 values. On the other hand, the pressure waves propagate slightly faster in the interlayer when S_1 parameter is larger. In other words, bulging occurs faster for larger values of S_1. To this end, larger S_1 values seem to be better for the performance of the armor.

The gauge points 5, 6 and 7, on the interlayer, are eroded due to element distortion

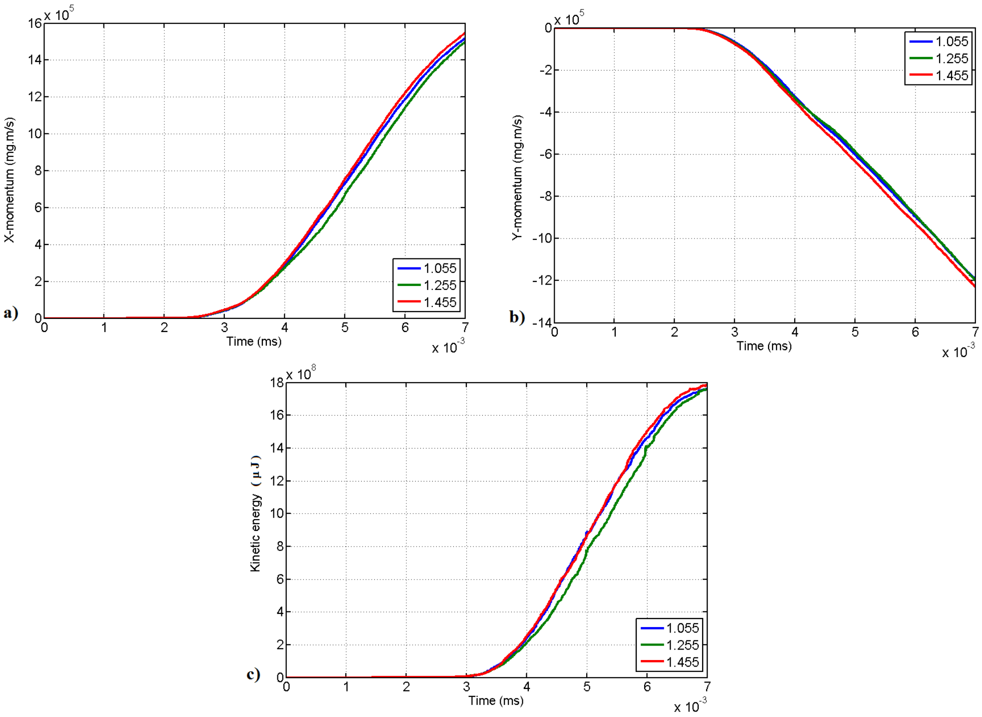

Figure 4.20: Results of FMP are given with respect to S_1 variation of the interlayer material. a) x-momentum - time, b) y-momentum - time and c) kinetic energy - time

as well. In Figure 4.23a, Figure 4.23b and Figure 4.23c, sudden decline in the curves indicates erosion of the gauge points. According to the results in Figure 4.23, pressure values of the interlayer with S_1= 1.455 are a little lower than the others. Unlike the results in Figure 4.22, peak pressure values at the gauge points 5, 6 and 7 can be measured. While maximum pressure value at the gauge point 5 is measured approximately $12 \cdot 10^6$ kPa, lower pressures ($8 \cdot 10^6$ kPa) are found at the gauge point 7 due to further distance from the interaction region. Furthermore, the process by which pressure wave is generated is related to the S_1 parameter. As can be seen in Figure 4.23, higher S_1 values are essential for fast propagation of pressure waves. Consequently, the higher the S_1 parameter, the faster the response time of the interlayer to bulge.

The velocity changes at the gauge points 11 and 13, on the FMP, are presented in Figure 4.24 and Figure 4.25. As mentioned earlier, highly accelerated gauge points indicate that the bulging performance of the NERA is better. In the velocity-time histories of the gauge points 11 and 13, it can be seen that the FMP begins to accelerate more quickly when the S_1 parameter of the interlayer is higher. Moreover, the gauge point 13 moves at higher x- and y-velocities compared to the gauge point 11.

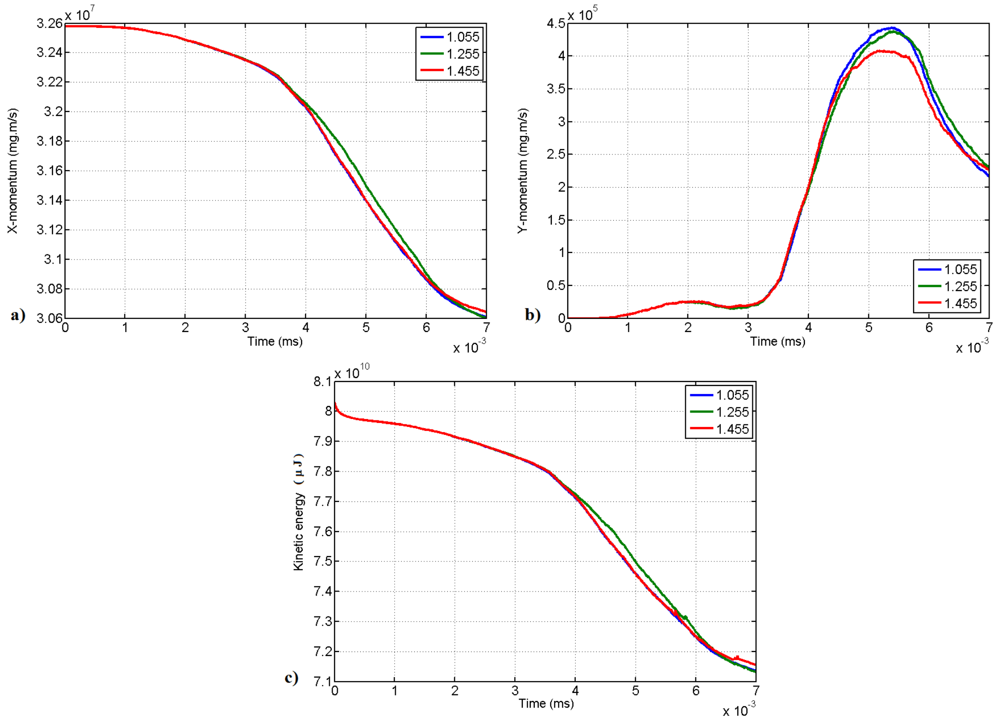

Figure 4.21: Results of the jet are given with respect to S_1 variation of the interlayer material. a) x-momentum - time, b) y-momentum - time and c) kinetic energy - time

Its x-velocity reaches the maximum value of about 180 m/s after 5.5 microseconds. For the gauge point 13, the acceleration time getting to about 225 m/s in the negative y direction is quite short and approximately 7 microseconds. On the other hand, the x- and y-velocities of the gauge point 11 can reach approximately the values of 130 m/s (+ x direction) and 25 m/s (-y direction), respectively. In conclusion, it is considered that the increasing of S_1 can result in high bulging performance due to faster acceleration of the metal plates.

4.4 Results of Effects of Impedance

According to the results of the previous sections, it was found that the density (ρ) and C_1 parameter of the interlayer could significantly change the bulging performance of the NERA. The parameter S_1 of the interlayer has far less effect on the performance of the armor than the others. It was concluded that higher density and higher C_1 (bulk sound speed) of the interlayer lead to better performance of the NERA. Similar results were found by Rosenberg and Dekel [25]. Based on these results, it is decided

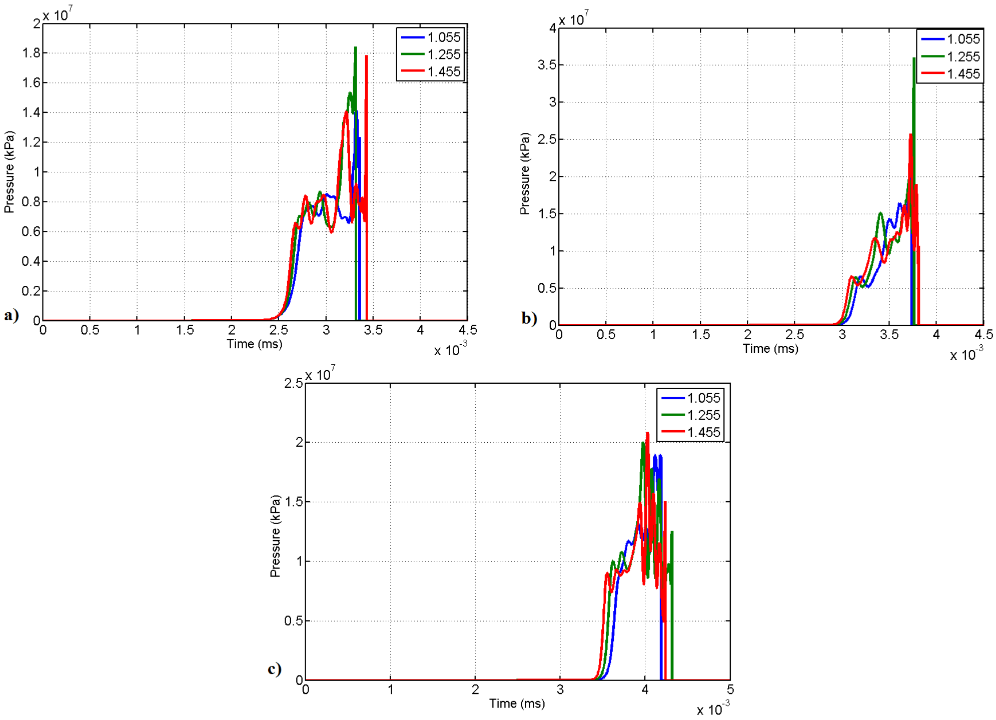

Figure 4.22: Pressure results of gauge points are given with respect to S_1 variation of the interlayer material. a) pressure at gauge point 2, b) pressure at gauge point 3 and c) pressure at gauge point 4

to investigate the effects of impedance (Z) on the bulging performance of the NERA. Impedance is equivalent to the product of the density and C_1. To understand the importance of impedance on the performance of the armor, the impedance value of the interlayer material is taken as constant. In other words, both the density and C_1 values are changed simultaneously such that their product does not change. Simulations are conducted for three combinations of ρ and C_1 values. These are presented below.

- Impedance-1: $\rho = 1.186$ g/cm^3, $C_1 = 3.2340 \cdot 10^3$ m/s ($\rho \cdot C_1 = 3.8355 \cdot 10^5$ g·cm^{-2}·s^{-1})

- Impedance-2: $\rho = 1.286$ g/cm^3, $C_1 = 2.9825 \cdot 10^3$ m/s ($\rho \cdot C_1 = 3.8355 \cdot 10^5$ g·cm^{-2}·s^{-1})

- Impedance-3: $\rho = 1.086$ g/cm^3, $C_1 = 3.5318 \cdot 10^3$ m/s ($\rho \cdot C_1 = 3.8355 \cdot 10^5$ g·cm^{-2}·s^{-1})

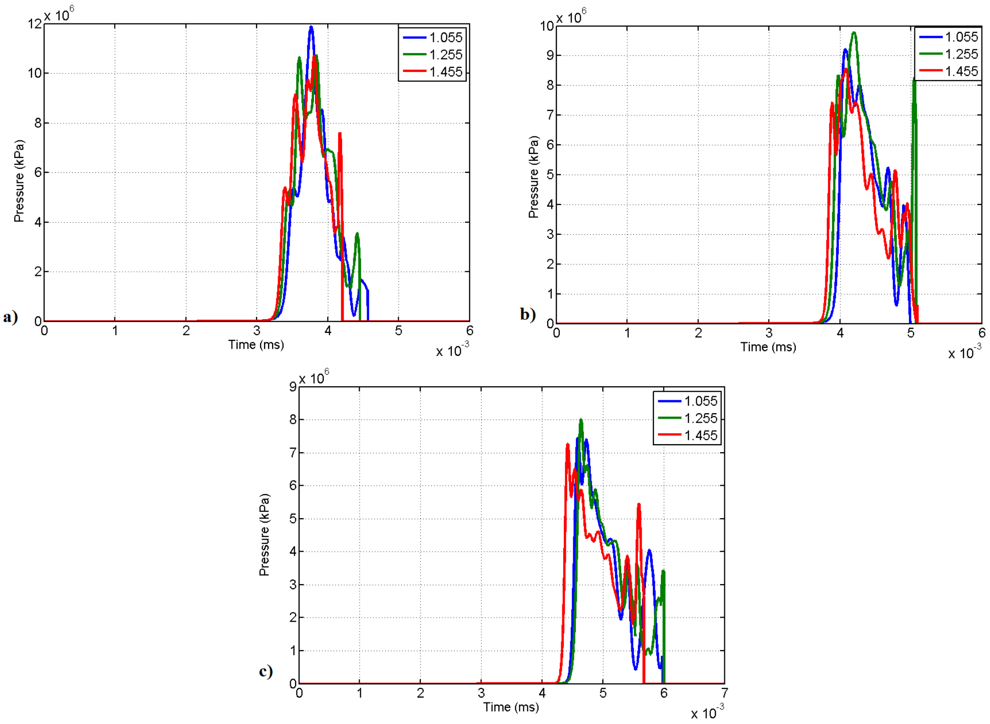

Figure 4.23: Pressure results of gauge points are given with respect to S_1 variation of the interlayer material. a) pressure at gauge point 5, b) pressure at gauge point 6 and c) pressure at gauge point 7

4.4.1 Effects of Impedance on Momentum and Kinetic Energy of the BMP

In Figure 4.26, results of the x-momentum, the y-momentum and the kinetic energy of the interlayer material are shown for three combinations of an impedance value of $3.8355 \cdot 10^5$ g·cm^{-2}·s^{-1}. In the plots, Impedance-1 is the combination of the original density and C_1 values of epoxy-res2. On the other hand, in Impedance-2, the original density value is increased to 1.286 g/cm^3 and the original C_1 value is decreased to $2.9825 \cdot 10^3$ m/s. In Impedance-3, the original density value is decreased to 1.086 g/cm^3 and the original C_1 value is increased to $3.5318 \cdot 10^3$ m/s. As can be seen in Figure 4.26, there are some changes in the x-momentum and the kinetic energy of the BMP. This difference can be seen especially in the peak region and the post-peak region of the curves. The peak on these curves corresponds to the point of maximum momentum and kinetic energy values. The difference between the maximum x-momentum values is about $0.5 \cdot 10^5$ mg·m/s. Additionally, the difference between the maximum kinetic energy values is about $1 \cdot 10^8$ microjoule. On the other hand, the y-momentum of the BMP, are found almost the same for these three cases.

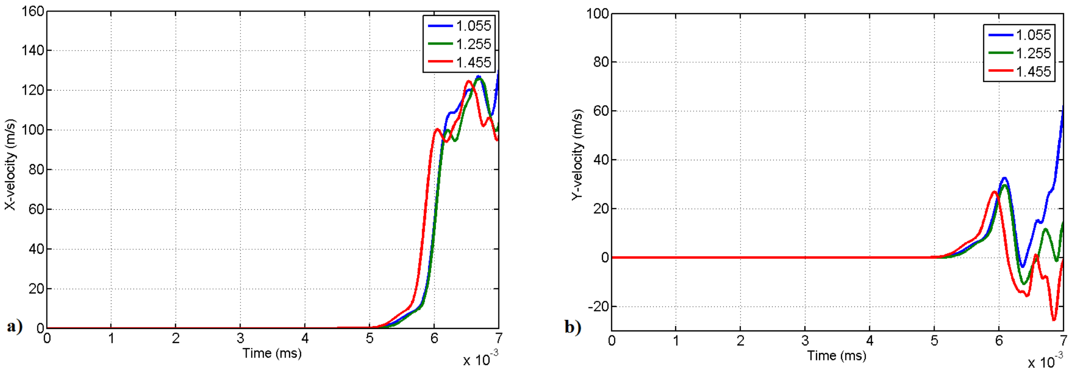

Figure 4.24: Velocity results of gauge point 11 are given with respect to S_1 variation of the interlayer material. a) x-velocity - time and b) y-velocity - time

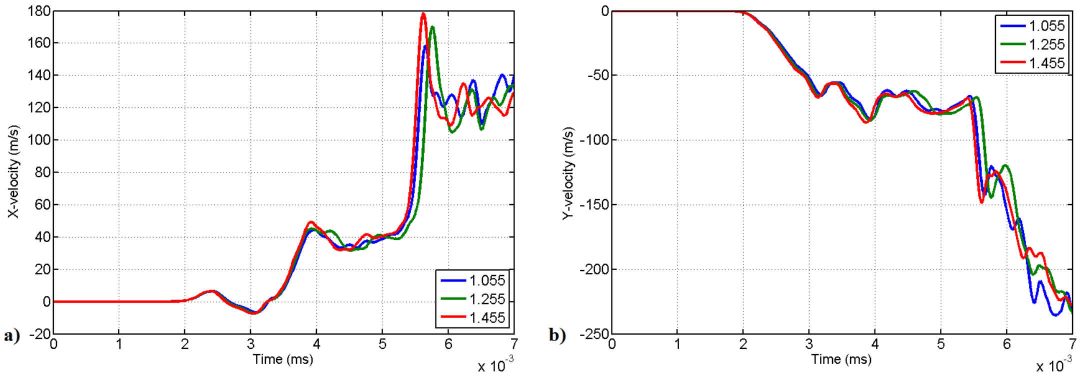

Figure 4.25: Velocity results of gauge point 13 are given with respect to S_1 variation of the interlayer material. a) x-velocity - time and b) y-velocity - time

Figure 4.5, shown and discussed earlier, gives the results of the x-momentum, the y-momentum and the kinetic energy of the BMP. The interlayers are composed of the inert plates with various densities (1.086, 1.186 and 1.286 g/cm^3) and constant C_1 ($3.234 \cdot 10^3$ m/s). In this case, different impedance values are obtained for the interlayer. When a comparison is made between the results in Figure 4.5 and Figure 4.26, it can be stated that the momentum and kinetic energy curves in Figure 4.26 are much closer together than the curves in Figure 4.5. For example, while the y-momentum difference within 7 microseconds can reach up to $2 \cdot 10^5$ mg$\cdot$ m/s in Figure 4.5, the momentum difference is nearly zero in Figure 4.26. It is considered that the main reason of the difference is probably the effect of impedance on the NERA.

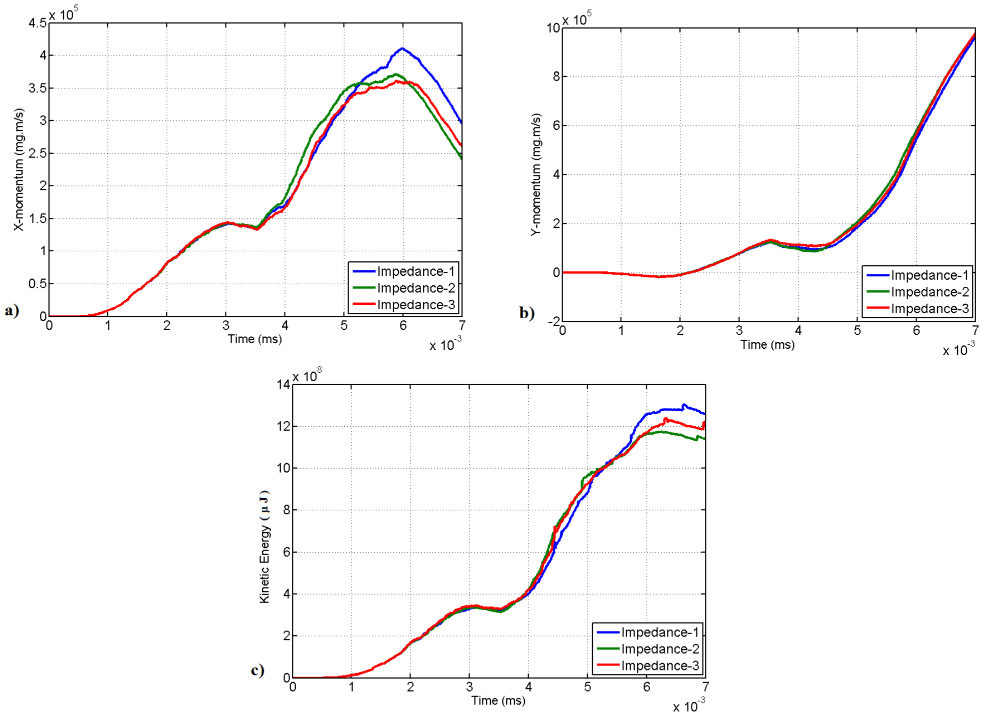

Figure 4.26: Constant impedance value is defined for the intermediate layer. a) change of the x-momentum of the BMP, b) change of the y-momentum of the BMP and c) change of the kinetic energy of the BMP

4.4.2 Effects of Impedance on Momentum and Kinetic Energy of the FMP

In Figure 4.27, the x-momentum - time, the y-momentum - time and the kinetic energy-time histories of the FMP are presented. Similar to the analysis of the BMP, three impedance combinations are investigated. According to this figure, the changes in the x- and y-momentum of the FMP are almost the same for the three impedance combinations considered. Additionally, the kinetic energy curves of the FMP are very close to each other. The FMP plays a critical role in disturbing the jet because of longer interaction time with the jet. In addition, the downward or upward deflection of the jet results mainly from the bulging of the FMP. Accordingly, it is considered that the y-momentum of the FMP is an important criterion to determine the performance of the armor. To find the effect of impedance on the y-momentum of the FMP, a comparison is made between the results in Figure 4.6 and Figure 4.27. In compliance with the comparison, the y-momentum curves in Figure 4.27 are much closer together than the curves in Figure 4.6. As mentioned before, the results, given in Figure 4.6, show cases for variable impedance.

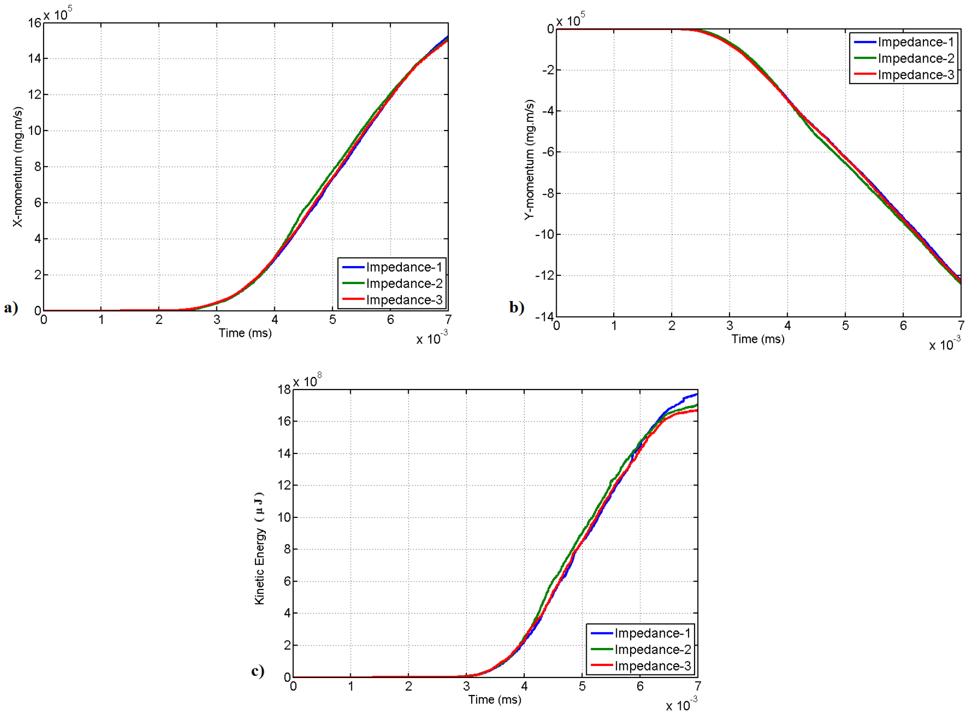

Figure 4.27: The interlayers are composed of the inert plates with a constant impedance value. a) change of the x-momentum of the FMP, b) change of the y-momentum of the FMP and c) change of the kinetic energy of the FMP

4.4.3 Effects of Impedance on Momentum and Kinetic Energy of the Jet

The results of the x-momentum, the y-momentum and the kinetic energy of the jet are shown in Figure 4.28. In accordance with the results, the momentum and the kinetic energy of the jet do not change noticeably for the impedance combinations. Therefore, it seems that the behavior of the jet is not significantly affected by a simultaneous change of the density and the bulk sound speed as long as the impedance is kept constant.

4.4.4 Effects of Impedance on Pressure and Velocity Variation of Gauge Points

In Figure 4.29 and Figure 4.30, pressure changes at the gauge points 2, 3, 4, 5, 6 and 7 are shown for the three impedance combinations. As can be seen in these pressure plots, pressure instantaneously drops to zero due to the erosion phenomenon. In addition, pressure-time response is slightly faster when C_1, the impedance multiplier, is increased.

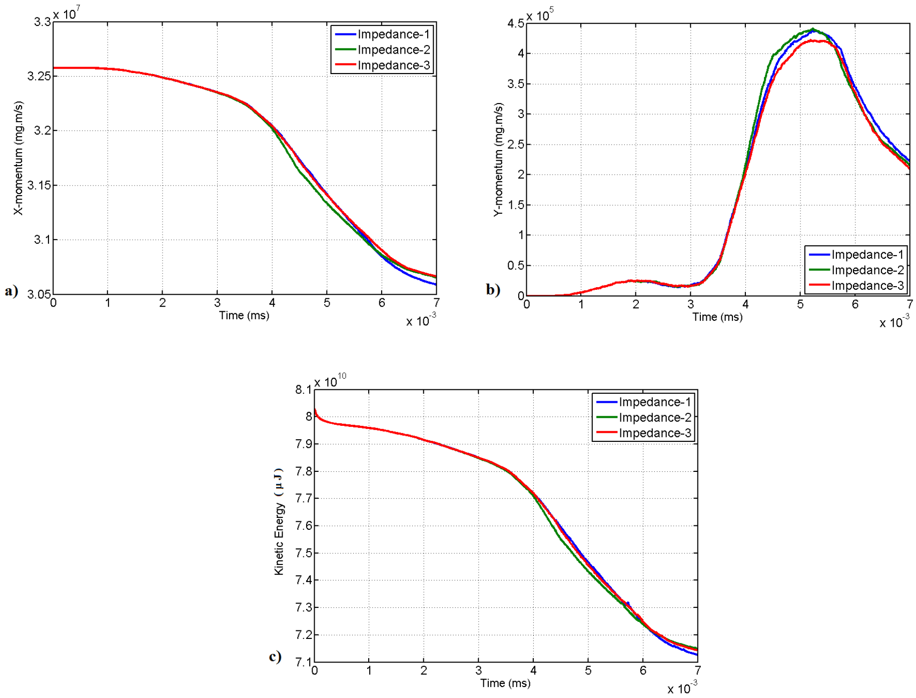

Figure 4.28: The interlayers are composed of the inert plates with a constant impedance value. a) change of the x-momentum of the jet, b) change of the y-momentum of the jet and c) change of the kinetic energy of the jet

The velocity changes at the gauge points 11 and 13, on the FMP, are presented in Figure 4.31 and Figure 4.32. In the velocity-time histories of the gauge points 11 and 13, it can be seen that the FMP begins to accelerate a little quicker when C_1, the impedance multiplier, is higher. Additionally, the velocity curves of the gauge point 13 are very similar for the impedance combinations.

In a nutshell, some criteria for determination of the most effective interlayer are investigated. These criteria are the kinetic energy, the x-momentum and the y-momentum of the jet, the BMP and the FMP, pressure results of the gauge points on the interlayer and the FMP and velocity results of the gauge points on the FMP. In the density range investigated in this thesis, increasing the density of the intermediate layer improves the bulging performance of the armor. In particular, the momentums of the BMP and the FMP increase in parallel with the increase in the density of the interlayer. In the C_1 range investigated in this work, the increase of C_1 value of the interlayer material contributes the bulging performance of the armor. According to increasing C_1 value, the momentums of the BMP and the FMP consistently increases. Additionally,

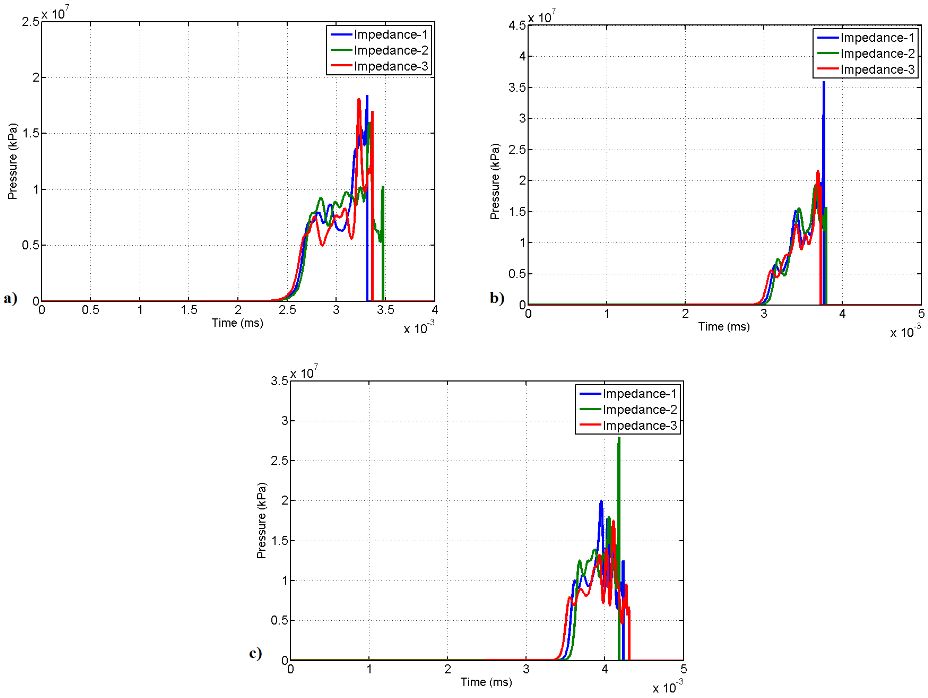

Figure 4.29: The interlayers are composed of the inert plates with a constant impedance value. Gauge points are located on the intermediate layer of NERA. a) change of pressure in gauge point 2, b) change of pressure in gauge point 3 and c) change of pressure in gauge point 4

pressure wave is transmitted to the FMP earlier due to increasing C_1 value. In the S_1 range investigated in this work, the effects of S_1 parameter on bulging of the BMP, the FMP and the jet do not deliver distinct results as ρ and C_1. However, this parameter contributes the performance of the armor. Up to now, it has been mentioned that higher density and higher C_1 of the intermediate layer yield better performance of the armor. Rosenberg and Dekel discussed similar results in their paper [25].

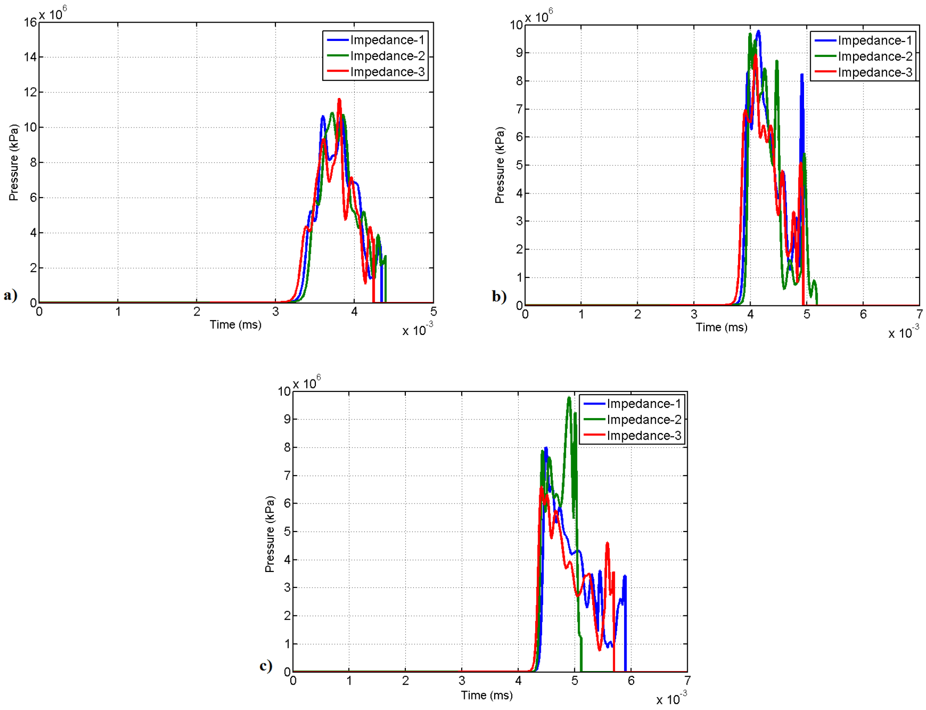

Figure 4.30: The interlayers are composed of the inert plates with a constant impedance value. Gauge points are located in the intermediate layer of NERA. a) change of pressure in gauge point 5, b) change of pressure in gauge point 6 and c) change of pressure in gauge point 7

Effects of the product of ρ and C_1 called impedance on momentum and kinetic energy of the BMP, the FMP and the jet are investigated. Pressure variation of gauge points on the interlayer and velocity variation of gauge points on the FMP are also investigated. A constant impedance value of the interlayer material causes almost the same results for most of the performance criteria. Therefore, the impedance value of the intermediate layer is a critical parameter in evaluating the performance of the armor.

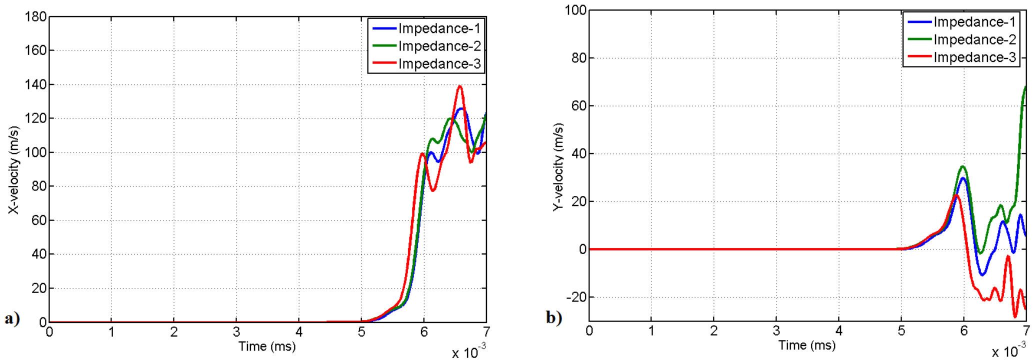

Figure 4.31: Velocity results of gauge point 11 are given for the three impedance combinations. a) x-velocity - time and b) y-velocity - time

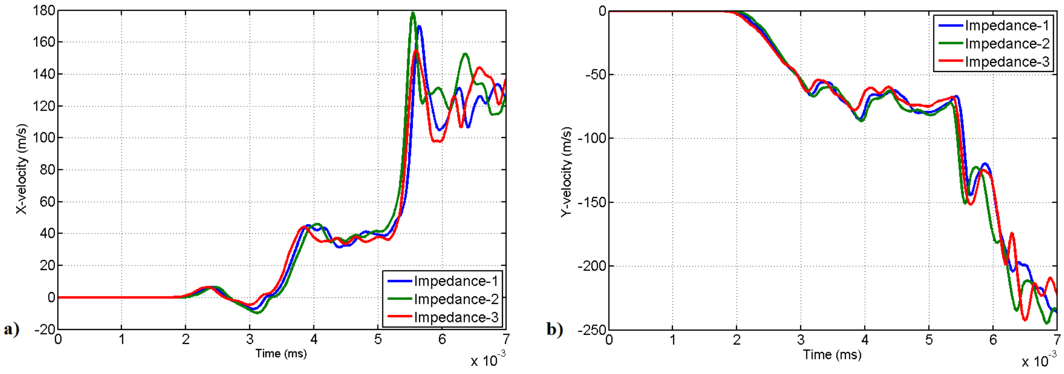

Figure 4.32: Velocity results of gauge point 13 are given for the three impedance combinations. a) x-velocity - time and b) y-velocity - time

CHAPTER 5

CONCLUSION

Reactive armors also called add-on armors are arranged on both the side and front wall of heavily armoured vehicles. The purpose of these armors is to provide extra protection to the heavily armoured vehicles. The reactive armors are particularly effective against attack by anti-tank weapons. The anti-tank weapons utilize shaped charge warheads. Shaped charge jets, formed by the collapse of a metal liner, have a tendency to penetrate into the main armor. To increase the survivability and multiple-hit capability of the add-on armors, non-energetic reactive armors (NERAs) have been developed. NERAs also called bulging armors are one type of reactive armors. A non-energetic reactive armor (NERA) has a sandwich-like structure and consists of two parallel metal plates with an interlayer. This interlayer is made of a non-energetic material such as rubber or polymer. This material can absorb the impact energy produced by the shaped charge jet and cause the bulging of metal plates. In addition, these metal plates are accelerated in opposite directions by shock waves.

In the literature, studies on non-energetic reactive armors (NERAs) are limited. For this reason, NERA has a less known defeat mechanism. On the other hand, there are some experimental, analytical and numerical studies in the literature. In the experiments, various interlayer materials, mainly polymers, are used to evaluate the performance of the bulging armor. The analytical and numerical studies are performed in the two-dimensional and the three-dimensional models. According to the literature, the high density of a bulging armor makes it a highly effective armor against threat. In other words, the performance of the bulging armor is directly proportional to the density of the interlayer. In addition, the strength of the interlayer does not considerably affect the performance of the interlayer. On the other hand, it is stated in the literature that increase in the strength of the metal plates brings about performance increase for the bulging armor.

In the light of the literature, high performance NERAs are examined in this thesis. Numerical simulations are conducted for penetration of shaped charge jets into the bulging armors by using AUTODYN software. Penetration simulations are carried out for two consecutive steps. They are respectively formation of the jet and penetration of the jet into the bulging armor. The AUTODYN-Euler solver is used for the jet formation analysis. This formed jet is then transferred to the AUTODYN-Lagrange solver. In the AUTODYN material library, there are 12 inert materials that can be found to model the interlayer. These interlayer materials are investigated through simulations. The two-dimensional solver in AUTODYN (AUTODYN-2D) is used for fast calculation of the penetration analysis. After determination of an interlayer effective against the jet, the three-dimensional solver in AUTODYN (AUTODYN-3D) is used to obtain more exact solutions for the penetration analysis. The density and shock parameters of the interlayer are changed to inquire as to whether or not the performance of the bulging armor is based on these material properties. The effects of them on the interlayer are investigated.

In this thesis, the high velocity impact response of the bulging armor is investigated using AUTODYN. The Shock EOS is used as a material property for the simulation of the impacts of shaped charge jets on the bulging armor. This material property is defined for both the shaped charge and the bulging armor. Due to limited data available in the literature, the linear form of the Shock EOS is employed instead of the bilinear form of the Shock EOS. In the linear form, the user-defined shock parameters are C_1 (the bulk sound speed of a material) and S_1 (the slope of the curve of the shock velocity vs. the particle velocity). The formulation of the linear shock EOS based on these parameters can be seen in Chapter 2 equation 2.1. The effects of changing the C_1 and S_1 parameter on the performance of the bulging armor are investigated. In addition, the study on the performance of the bulging armor is continued to find the effects of density evaluated in the literature.

AUTODYN is based on continuum mechanics which relate to the dynamics of a continuous medium. The governing equations in AUTODYN are the conversation of mass, momentum and energy. They are also called the Rankine-Hugoniot jump conditions [35]. In this work, the shaped charge jet transfers its momentum and kinetic energy to the bulging armor during the interaction. The amount of momentum and energy transfers is indicative of the bulging performance of NERA. Therefore, changes in momentum and kinetic energy are investigated for both the jet and NERA.

In the two-dimensional and three-dimensional penetration simulations of the shaped charge jet, the initial values such as the distance between a shaped charge and a bulging armor (stand-off distance), the angle between the jet‘s flow direction and the normal of the armor and the thicknesses of each layer of the armor are not changed. These values are given in Chapter 3. The aim of this add-on armor system is to prevent the penetration of the shaped charge jet into the main armor by deflecting it out of its flow direction. In this regard, it should be obtained lower results for the x-momentum and kinetic energy of the jet. Moreover, the y-momentum of the jet should be as high as possible to protect the main armor. On the other hand, it can be stated that highly accelerated flying plates exhibit better bulging performance.

Conclusions from the results of the two-dimensional simulations are mentioned below.

- In the two-dimensional simulations of bulging armors, some criteria are investigated to determine the most effective interlayer material. These criteria are the kinetic energy, x-momentum and y-momentum of the jet, the BMP and the FMP and velocity results of the gauge points on the jet, the BMP and the FMP. In accordance with most of the criteria, epoxy-res2 is found to be the most effective for protection against shaped charges. As can be seen in Table 3.1, the original C_1 parameter of epoxy-res2 is the highest. On the other hand, adiprene and polyrubber are the lowest effective materials according to their bulging performance. The original density values of adiprene (0.927 g/cm^3) and polyrubber (1.01 g/cm^3) are the lowest except polyethylene, see Table 3.1. It is concluded that low density interlayer degrades the bulging performance of the armor.

In three-dimensional simulations of bulging armors, some criteria investigated in this work are the kinetic energy, the x-momentum and the y-momentum of the jet, the BMP and the FMP, pressure results of the gauge points on the interlayer and the FMP and velocity results of the gauge points on the FMP. It can be concluded from the results of the simulations that:

- According to the density range investigated in this study, the bulging performance of the armor is improved by increasing the density of the intermediate layer. The momentums of the BMP and the FMP particularly increase with the increase in the density of the interlayer.
- In accordance with the C_1 range investigated in this study, the increase of C_1 value of the interlayer material improves the bulging performance of the armor. The momentums of the BMP and the FMP consistently increase with increasing C_1 value. Furthermore, increasing C_1 value causes pressure waves to reach the FMP earlier.
- According to the S_1 range investigated in this study, S_1 parameter does not have a strong influence on bulging of the armor in comparison to ρ and C_1 parameter.
- Effects of impedance (the product of ρ and C_1) on momentum and kinetic energy of the BMP, the FMP and the jet are investigated. Pressure variation of gauge points on the interlayer and velocity variation of gauge points on the FMP are also investigated. Both the density and C_1 values are changed simultaneously to obtain a constant impedance value. The constant impedance value of the interlayer material causes almost the same results for most of the performance criteria. Herewith, it is thought that impedance value of the intermediate layer is a critical parameter in evaluating the performance of the armor.

5.1 Further work

In the current work, the many initial values (i.e. stand-off distance, thicknesses of each layer, etc.) mentioned before are taken as constant. The intermediate layer material and its material properties are the only variables among those significant parameters for the performance of NERAs. Other parameters mentioned above can also be investigated. Furthermore, an additional performance criterion, which is used in experiments, penetration to witness plate can be used in simulations.

Furthermore, a linear form of the shock EOS, a particular equation of state in AUTODYN, is used for the materials of both shaped charge and NERA in this work. These materials can be expressed in the bilinear form of the shock EOS, based on experiments, if necessary test data is available. Both two-dimensional and three-dimensional simulations can be conducted according to this material definition. In this way, simulation accuracy can be ensured by the experiments.

REFERENCES

[1] *Autodyn Theory Manual*. Century Dynamics Inc., 2001.

[2] G. Baudin and R. Serradeill. Review of jones-wilkins-lee equation of state. In *EPJ Web of Conferences 10,00021*, 2010.

[3] T. Belytschko and Mullen. Stability of explicit-implicit mesh partitions in time integration. In *International Journal for Numerical Methods in Engineering, Vol.12*, pages 1575–1586, 1978.

[4] J. Carleone. *Tactical Missile Warheads*. American Institute of Aeronautics and Astronautics Inc., 1993.

[5] Y. Cohen-Arazi, E. Sokol, S. Frilling, and I. Shaked. Extremely insensitive detonating substance and method for its manufacture. Patent, United States, No 8277584 B2, 2012.

[6] N. Gov, Y. Kivity, and D. Yaziv. On the interaction of a shaped charge jet with a rubber filled metallic cassette. In *13th International Symposium on Ballistics*, pages 95–102, 1992.

[7] E. Grüneisen. Theorie des festen zustandes einatomiger elemente. In *Annalen der Physik,* 344(12), pages 257–306, 1912.

[8] E. Gürel. Modeling and simulation of shaped charges. In *M.s thesis, Middle East Technical University*, 2009.

[9] M. Held. Explosive reactive armor. Patent, Germany, No 2008156, 1970.

[10] M. Held. Schutzeinrichtung gegen Geschosse, insbesondere Hohlladungsgeschosse (protection device against projectiles, especially shaped charges). Patent, Germany, No 2358227, 1973.

[11] M. Held. Disturbance of shaped charge jets by bulging armour. In *Propellants, Explosives, Pyrotechnics*, pages 26:191–195, 2001.

[12] Z. X. Huang, X. D. Zu, Q. Q. Xiao, and X. Jia. The role of the wave impedance of the sandwich material in the composite armor against shaped charge jet. In *26th International Symposium on Ballistics*, pages 1326–1333, 2007.

[13] X. Jia, Z. X. Huang, X. D. Zu, X. H. Gu, C. S. Zhu, and Z. W. Zhang. Experimental study on the performance of woven fabric rubber composite armor

subjected to shaped charge jet impact. In *International Journal of Impact Engineering*, pages 57:134–144, 2013.

[14] G. R. Johnson and W. H. Cook. A constitutive model and data for metals subjected to large strains, high strain rates and high temperatures. In *7th International Symposium on Ballistic*, pages 541–547, 1983.

[15] S. L. Knoeller. Protecting the warfighter-recent armor innovations. In *Countering the Modern Threat, AMMTIAC, Volume 4 No 4*, pages 8–9, 2010.

[16] M. C. Kurt, F. Saeidi, T. Deniz, and E. Gürses. 3d numerical simulation of non-energetic reactive armor. In *8th Ankara International Aerospace Conference*, 2015.

[17] E. L. Lee, H. c. Horning, and J. W. Kury. Adiabatic expansion of high explosives detonation products. In *Lawrence Livermore National Laboratory, University of California, Livermore, TID 4500-UCRL 50422*, 1968.

[18] D. E. Lemons and C. M. Lund. Thermodynamics of high temperature, mie-gruneisen solids. In *Am. J. Phys., Vol. 67, No. 12*, pages 1105–1108, 1999.

[19] E. Lidén, A. Helte, and A. Tjernberg. Multiple cross-wise orientated nera-panels against shaped charge warheads. In *23rd International Symposium on Ballistics*, pages 1373–1380, 2007.

[20] M. Mayseless. Reactive armor - simple modeling. In *25th International Symposium on Ballistics*, pages 1554–1563, 2010.

[21] M. Mayseless, Y. Erlich, Y. Falcovitz, and G. Rosenberg. Interaction of shaped charge jets with reactive armor. In *8th International Symposium on Ballistics*, pages VII–15–20, 1984.

[22] M. S. Mayseless, E. Marmor, N. Gov, Y. Kivity, J. Falcovitz, and D. Tzur. Interaction of a shaped charge jet with reactive or passive cassettes. In *14th International Symposium on Ballistics, volume 2*, pages 439–448, 1993.

[23] G. Mie. Zur kinetischen theorie der einatomigen körper. In *Annalen der Physik,* 316.8, pages 657–697, 1903.

[24] D. Orlikowski, A. A. Correa, E. Schwegler, and J. E. Klepeis. A steinberg-guinan model for high-pressure carbon, diamond phase. In *Lawrence Livermore National Laboratory*, 2007.

[25] Z. Rosenberg and E. Dekel. A parametric study of the bulging process in passive cassettes with 2d numerical simulations. In *International Journal of Impact Engineering*, pages 21(4):297–305, 1998.

[26] Z. Rosenberg and E. Dekel. *Terminal Ballistics*. Springer, 2012.

[27] P. C. Souers. *JWL Calculating*. Lawrence Livermore National Laboratory, 2005.

[28] K. Thoma, D. Vinckier, J. Kiermeir, U. Deisenroth, and W. Fucke. Shaped charge jet interaction with highly effective passive sandwich systems-experiments and analysis. In *Propellants, Explosives, Pyrotechnics*, pages 18:275–281, 1993.

[29] W. Walters. A brief history of shaped charges. In *24th International Symposium on Ballistics*, 2008.

[30] W. P. Walters and J. A. Zukas. *Fundamentals of Shaped Charges*. John Wiley, Sons, 1989.

[31] H. S. Yadav. Study of jet interaction with interlayer material of bulging armor. In *Propellants, Explosives, Pyrotechnics*, pages 29(6):349–353, 2004.

[32] D. Yaziv, S. Frilling, and Y. Kivity. The interaction of inert cassettes with shaped charge jets. In *15th International Symposium on Ballistics*, pages 461–467, 1995.

[33] X. Zu, Z. Huang, and X. Jia. Study on rubber composite armor anti-shaped charge jet penetration. In *Propellants, Explosives, Pyrotechnics*, pages 35:1–8, 2013.

[34] X. D. Zu, Z. X. Huang, and Q. Q. Xiao. Dip angle effect on the impact of polybutylene rubber composite target resistance to jet penetration. In *25th International Symposium on Ballistics*, pages 1239–1246, 2010.

[35] J. A. Zukas. *Introduction to Hydrocodes*. Elsevier, 2004.